

Synthesis, characterization and catalytic testing of metal tungstates as catalysts for activation of lower alkanes

vorgelegt von
Master of Science
Xuan Li
aus Hunan (China)

Von der Fakultät II – Mathematik und Naturwissenschaften
der Technischen Universität Berlin
Zur Erlangung des akademischen Grades

Doktor der Naturwissenschaften

Dr. rer. nat
genehmigte Dissertation

Promotionsausschuss:

Vorsitzender: Prof. Dr. Peter Hildebrandt

Gutachter: Prof. Dr. Robert Schlögl

Gutachter: Prof. Dr. Reinhard Schomäcker

Gutachter: Prof. Dr. Klaus Rademann

Tag der wissenschaftlichen Aussprache: 28.02.2017

Berlin 2017

Acknowledgement

First and foremost, I want to thank Prof. Schlögl for giving me the opportunity to conduct my research at the Fritz-Haber-Institute of the Max-Planck-Society. I felt excited every morning on the way to work. Thanks him for bringing together so many characterization techniques, providing chance to pursue more comprehensive and deeper understanding in heterogeneous catalysis. His delightful and humorous way of conveying his feelings and thoughts makes it a pleasure to present him the scientific result, although there is always a chance to receive his criticism. His broad knowledge and deep understanding in catalysis greatly helps my PhD project.

I would like to deeply acknowledge my supervisor Dr. Annette Trunschke, for her continuous encouragement, suggestions and also criticism. In China, there is a saying “Yan shi chu gao tu”, meaning strict teacher educates good students. And I would also like to thank her for the freedom she gave me to pursue my ideas. Her curiosity into the scientific truth always stimulates me.

I would like to particularly acknowledge my supervisor Dr. Frank Rosowski, for providing me the opportunity to conduct my PhD research as collaboration between BasCat UniCat BASF JointLab and Fritz-Haber-Institute. And I would like to thank him for his patience and freedom to my study, and for his continuous support.

I would also like to acknowledge the members of the doctoral board: Prof. Reinhard Schomacker at the Technical University of Berlin for hosting me as an external student, Prof. Klaus Rademann at the Humboldt University of Berlin for serving as the referee. I also thank Prof. Peter Hildebrandt at the Technical University of Berlin for taking the chair during the defense.

I would like to thank Pierre Kube and Mateusz Jastak for transferring knowledge about the parallel reactor. I would also like to thank Dr. Xing Huang for introduction to basic and practical knowledge about transmission electron microscope. Similarly, I would like to thank Verena Pfeifer for her help in XPS and NEXAFS analysis, and introduction to fundamental knowledge about these techniques.

I would like to thank Dr. Thomas Lunkenbein for his continuous support in high resolution transmission electron microscopic analysis. And in a similar manner, I would like to thank Dr. Detre Teschner for his support in laboratory XPS analysis.

A member of colleagues in the Department of Inorganic Chemistry and BasCat lab contributed in performing experiments, calculation, technical assistance and discussions. I would like to acknowledge the following people (in no particular order): Jutta Kröhnert (IR), Dr. Friedrich Seitz (in situ IR), Dr. Teng Fu (IR and Raman), Dr. Travis Jones (Theory), Prof. Dr. Sophia Klokishner (Theory), Dr. Frank Girgsdies (XRD), Gisela Weiberg (SEM), Wiebke Frandsen (TEM and SEM),

Maike Hashagen (N_2 physisorption), Dr. Johannes Noack (Raman), Christian Schulz (catalytic testing in ODH of butane), Jasmin Allan (TG-MS and XRD), Dr. Olaf Timper (XRF).

I would like to thank my officemates Hamideh Ahi, Marie Mathilde-Millet and Dr. Teng Fu for the warm atmosphere and help in many aspects. I also thank members of “Reactivity group” and “BasCat” for valuable discussions and encouragement.

Berlin International Graduate School of Natural Science and Engineering (BIG-NSE) is gratefully acknowledged for a scholarship.

Last but certainly not least important, I thank my wife Cen Kuang, my parents and parents-in-law for their support, encouragement and love. This thesis is dedicated to them!

Abstract

The electronic and structural properties of vanadium-containing phases govern the formation of isolated active sites at the surface of these catalysts for selective alkane oxidation. This concept is not restricted to vanadium oxide. The deliberate use of hydrothermal techniques can turn the typical combustion catalyst manganese oxide into a selective catalyst for oxidative dehydrogenation of propane (ODP). Nanostructured, crystalline MnWO_4 serves as the support that stabilizes a defect-rich MnO_x surface phase. Oxygen defects can be reversibly replenished and depleted at the reaction temperature. Terminating MnO_x zigzag chains on the (010) crystal planes are supposed to bear structurally site-isolated oxygen defects that account for the unexpectedly good performance of the catalyst in propane activation.

The mechanism of C-H activation in selective oxidation reactions of short-chain alkane molecules over transition metal oxides is critically affected by the balance of acid-base and redox sites at the surface of the catalyst. Using the example of manganese tungstate we discuss how the relative abundance of these sites can be controlled via synthetic techniques. Phase-pure catalysts composed of the thermodynamic stable monoclinic MnWO_4 phase have been prepared by hydrothermal synthesis. Variation of the initial pH value resulted in rod-shaped nano-crystalline MnWO_4 catalysts composed of particles with varying aspect ratio. The synthesis products have been analysed by transmission electron microscopy, X-ray diffraction, infrared and photoelectron spectroscopy. In-situ Raman spectroscopy was used to investigate the dissolution-re-crystallization processes occurring under hydrothermal conditions. Ethanol oxidation was applied to probe the surface functionalities in terms of acid-base and redox properties. Changes in the aspect ratio of the primary catalyst particles are reflected in the product distribution induced by altering the fraction of acid-base and redox sites exposed at the surface of the catalysts in agreement with the proposed mechanism of particle growth by re-crystallization during ageing under hydrothermal conditions.

Phase-pure CoWO_4 catalysts were successfully prepared by hydrothermal synthesis and tested in ODP. Higher initial pH value in the synthesis gel gives rise to a higher Co/W ratio in the near surface region as detected by XPS. Furthermore, there exists a correlation between the specific propane consumption rate and the Co/W ratio. CoWO_4 enriched in tungsten in the near surface region shows low selectivity to propene, and the selectivity to conversion trajectory is similar to that of mesoporous tungsten oxide. However, the catalyst with the highest Co/W ratio shows the best selectivity to propene at around 9 % propane conversion. Moreover, the surface termination by a Co chain structure on the (010) crystal planes is confirmed by HRTEM. FT-IR spectroscopy exhibits a band at 3387 cm^{-1} attributed to surface Co bridging hydroxyl groups. The terminating oxo-hydroxy layer in the catalyst precursor is

proposed to develop a Co-rich defective surface responsible for high activity and selectivity of CoWO_4 in ODP.

Zusammenfassung

Elektronische und strukturelle Eigenschaften vanadiumhaltiger Phasen steuern die Entstehung isolierter aktiver Zentren an der Oberfläche von Katalysatoren für die selektive Oxidation von Alkanen. Wir zeigen, dass dieses Konzept nicht nur auf Vanadiumoxide beschränkt ist. Durch gezielte Anwendung hydrothormaler Synthesemethoden konnte aus dem typischen Verbrennungskatalysator Manganoxid ein selektiver Katalysator für die oxidative Dehydrierung von Propan (ODP) entwickelt werden. Nanostrukturiertes, kristallines MnWO_4 dient als Trägermaterial, das in der Synthese eine defektreiche MnO_x -Oberflächenphase hervorbringt. Sauerstoffdefekte können bei Reaktionstemperatur reversibel verbraucht und regeneriert werden. Es wird vermutet, dass MnO_x -Zickzack-Ketten an der Oberfläche von (010)-Kristallflächen strukturell isolierte Sauerstoffdefekte tragen, die für die unerwartet gute Leistung des Katalysators in der Propanaktivierung verantwortlich sind.

Der Mechanismus der C-H-Aktivierung in selektiven Oxidationsreaktionen von kurzkettigen Alkanmolekülen gegenüber Übergangsmetalloxiden wird durch die Balance der Säure-Base- und Redox-Zentren an der Oberfläche von Katalysatoren kritisch beeinflusst. Am Beispiel des Manganwolframats wird diskutiert, wie die Verteilung dieser Zentren mittels synthetischer Techniken gesteuert werden kann. Phasenreine Katalysatoren aus der thermodynamisch stabilen monoklinen MnWO_4 Phase wurden durch hydrothermale Synthese hergestellt. Eine Variation des pH-Werts in der Synthese führte zu nanokristallinen MnWO_4 Katalysatoren, die aus stabförmigen Partikeln mit unterschiedlichem Aspektverhältnis bestehen. Die Syntheseprodukte wurden mittels Transmissionselektronenmikroskopie, Röntgenbeugung, Infrarot- und Photoelektronenspektroskopie analysiert. In-situ Ramanspektroskopie wurde verwendet, um die unter hydrothermalen Bedingungen auftretenden Lösungs- und Rekristallisationsverfahren zu untersuchen. Die Ethanoloxidation diente als Testreaktion, um die Oberflächenfunktionalitäten hinsichtlich Säure-Base- und Redox-Eigenschaften zu untersuchen. Eine Änderung des Aspektverhältnisses der primären Katalysatorteilchen spiegelt sich in der Produktverteilung wider. In Übereinstimmung mit dem vorgeschlagenen Mechanismus des Teilchenwachstums durch Rekristallisation während des Alterns unter hydrothermalen Bedingungen bestimmt das Aspektverhältnis den Anteil an Säure-Base- und Redox-Zentren, die an der Oberfläche der Katalysatoren exponiert sind, und damit die katalytischen Eigenschaften.

Phasereine CoWO_4 Katalysatoren wurden erfolgreich durch hydrothermale Synthese hergestellt und in der ODP-Reaktion getestet. Ein höherer anfänglicher pH-Wert führt zu einem höheren Co/W Verhältnis in der oberflächennahen Region der Katalysatoren. Es besteht eine Korrelation zwischen der spezifischen Propan-Verbrauchsgeschwindigkeit und dem Co/W Verhältnis der Katalysatoren. Der oberflächlich mit W angereicherte Katalysator zeigt eine viel geringere Selektivität hinsichtlich

Propen. Der Verlauf der Selektivität als Funktion des Umsatzes an diesem Katalysator ähnelt dem von mesoporösen Wolframoxid. Dagegen zeigt der Katalysator mit dem höchsten Co/W Verhältnis die beste Selektivität zu Propen bei einem Propanumsatz von 9%. HRTEM bestätigt, dass dieser Katalysator durch eine Co-Kettenstruktur auf den (010) Kristallflächen terminiert ist. Mittels FT-IR Spektroskopie wird eine Bande bei 3387 cm^{-1} für oberflächenverbrückende Hydroxylgruppen beobachtet. Das Vorhandensein einer solchen Oxo-Hydroxy-Schicht an der Oberfläche des Katalysatorvorläufers könnte für die Entwicklung der hohen Aktivität und Selektivität des Katalysators in der ODP-Reaktion verantwortlich sein, die auf eine defekt- und Co-reiche Oberfläche zurückzuführen ist.

List of figures

Figure 1.1 Near surface concentration of Te and V determined by XPS (escape depth 0.8 nm) at T=298 K, p=30 Pa O ₂ as a function of the concentration in the crystalline M1 framework measured by EDX (redrawn from ref. [1]).	4
Figure 1.2 STEM image of one M1 particle along the <001> direction. Red and blue circles highlight heptagonal and hexagonal open channels, respectively. Green circles highlight the M{M ₅ } structure. The bright dots represent columns of M-O polyhedra (reproduced from ref. [46]).	6
Figure 2.1 (S)TEM analysis of the MnWO ₄ powder catalyst: a) Overview TEM micrograph of the MnWO ₄ nanorods; b) HRTEM image of one nanorod particle viewed along [100]. The inset denotes the power spectra recorded on either side of the defect; c) HAADF-STEM image of condensed [001] oriented MnWO ₄ nanorods. The surface termination was identified by phase analysis of corresponding atomic resolution HAADF-STEM images; d) and e) atomic resolution HAADF-STEM images of (c); f) Schematic representation of the crystal structure of MnWO ₄ viewed along [001]. The Mn atoms are presented in white, W is coloured green and O atoms are displayed in red. The original images are given in the SI (Figure S2.1, 6c).	11
Figure 2.2 Surface termination of the <i>b</i> plane viewed along the growth direction [001] by FFT filtered atomic resolution STEM images a) HAADF, and b) inverted HAADF; The violet and green circles denote W and Mn atoms, respectively. The micrographs correspond to magnified images of Figure 1d. Original images are given in the SI (Figure S2.6).	12
Figure 2.3 Depth profile of elemental composition of MnWO ₄ nano-rods at two different depths represented by the inelastic mean free path (IMFP) of electrons measured by synchrotron-based NAP-XPS at T=300°C applying a total pressure of 0.25 mbar O ₂ and He at flows of 2 and 2.2 sccm, respectively.	12
Figure 2.4 <i>In-situ</i> Raman spectra in the 280-1000 cm ⁻¹ range measured during hydrothermal synthesis of MnWO ₄ nano-rods; Bands denoted with asterisks belong to the sapphire window of the Raman probe.	14
Figure 2.5 Catalytic performance of nano-structured MnWO ₄ (T=400°C, W/F=1.8-0.9 g s/ml) in comparison to VO _x /SiO ₂ (T=400-420°C, W/F=1.8 g s/ml) and various manganese oxides (T=330-395°C, W/F=1.8 g s/ml) in the oxidative dehydrogenation of propane in a feed composed of C ₃ H ₈ :O ₂ :N ₂ in a ratio of 10:5:85. The selectivity to propene is shown as a function of propane conversion. Other C-containing products are mainly CO, and CO ₂ .	16
Figure 3.1 In situ Raman spectra recorded during the synthesis of the catalysts a) AR1.5 and c) AR3.9 and the corresponding profiles of temperature and pH during synthesis of b) AR1.5 and d) AR3.9; The symbol * in the Raman spectra indicates the bands of the sapphire window of the Raman probe.	39

Figure 3.2 Electron microscopy images of the as-synthesized (top row) and thermally treated (bottom row) nanostructured MnWO ₄ materials AR1.5 (a) and f)), AR1.7 (b) and g)), AR3.2 (c) and h)), AR3.9 (d) and i)), and AR5.1 (e) and j)); Uncoloured TEM images are presented in the Supporting Information (Fig. S3.4).	41
Figure 3.3 HAADF-STEM images of MnWO ₄ nanoparticles viewed along <001> with different aspect ratios: a) AR1.5, b) AR5.1 and c) perspective model for a typical faceted nanoparticle. The original uncoloured images including Fast Fourier transform analysis are given in the Supporting Information, Fig. S3.6.	42
Figure 3.4 Schematic representation of the proposed anisotropic mechanism of particle growth.....	43
Figure 3.5 Selectivity in ethanol oxidation over the nanostructured MnWO ₄ catalysts at 10% ethanol conversion.	44
Figure 3.6 a) Specific reaction rates measured at T=310°C and normalized to surface area, and apparent activation energy as a function of the aspect ratio; Red solid circle: acetaldehyde formation rate; red open circle: apparent activation energy of acetaldehyde formation; black solid triangle: ethylene formation rate; black open triangle: apparent activation energy of ethylene formation; b) Rate of formation of ethylene as a function of Brønsted acid site density at the catalyst surface determined by ammonia adsorption and specific surface area measurements.....	44
Figure 3.7 a) Infrared spectra in the region of OH stretching vibrations after thermal treatment of the catalyst in the infrared cell in vacuum at 300°C; The measurement was performed in vacuum at 40°C; W 4f spectra (b)), and O 1s spectra (c)) of the catalysts AR1.5 and AR5.1 measured by synchrotron-based near ambient pressure X-ray photoemission spectroscopy (NAP-XPS) at an inelastic mean free path (IMFP) of ca. 0.6 nm in 0.25 mbar in O ₂ /He at a total gas flow of 4.2 sccm at 300°C.....	46
Figure 4.1 In situ Raman spectra recorded during the synthesis of the catalysts a) CoW6.2, b) CoW7.6 and c) CoW8.5.	60
Figure 4.2 XRD patterns of as-synthesized CoWO ₄ catalyst precursors.	60
Figure 4.3 SEM images of the a) CoW6.2, b) CoW7.6, c) CoW8.1 and d) CoW8.5 catalysts.....	62
Figure 4.4 HAADF-STEM images of the CoW8.5 catalyst.	62
Figure 4.5 a) HAADF-STEM image of one particle in the CoW8.5 catalyst viewed along the <001> direction, b) HR-STEM-HAADF and c) HR-STEM-BF images of the surface of the same catalyst viewed along the <100> direction.....	63
Figure 4.6 Catalytic performance of mesoporous WO ₃ , commercial Co ₃ O ₄ and nanostructured CoWO ₄ catalysts (T=400°C, W/F=0.9-2.4 g s mL ⁻¹) in the oxidative dehydrogenation of propane in a C ₃ H ₈ /O ₂ /N ₂ feed (10:5:85). The selectivity to propene is shown as a function of propane conversion. Other carbon-containing products are mainly CO and CO ₂	64
Figure 4.7 Steady state propane consumption rate as a function of Co/W ratio in the near surface region determined by XPS.	65
Figure 4.8 FT-IR spectra of CoWO ₄ catalysts in He flow at a) room temperature and b) 400°C.	66

Figure 4.9 Influence of partial pressure of a) propane, b) oxygen and c) water on the specific product formation rate on CoW6.2 catalyst.	67
Figure 4.10 Influence of partial pressure of a) propane, b) oxygen and c) water on the specific product formation rate on CoW8.5 catalyst.	68

List of tables

Table 2.1. Active site density and reactivity of the catalysts in the oxidative dehydrogenation of propane at T=400°C, W/F=1.8 g s/ml in a feed composed of C ₃ H ₈ :O ₂ :N ₂ in a ratio of 10:5:85.	16
Table 3.1 Specific surface area, results of shape analysis based on TEM, and crystallite size calculated from anisotropic fitting in Rietveld refinement of the XRD patterns	43
Table 4.1 Specific surface area, synthetic parameters and crystallite size calculated from anisotropic fitting in Rietveld refinement of the XRD patterns.....	61
Table 4.2 Surface-near molar ratios of CoWO ₄ according to XPS.....	63
Table 4.3 Apparent reaction orders with respect to propane, oxygen and water on tungsten containing catalysts.....	68

List of schemes

Scheme 1.1 Reaction network (adapted from ref. [11]) on supported V-, Mo- and W-oxide catalysts.....	2
Scheme 1.3 Termination model of the M1 phase (reproduced from ref. [42]).	5
Scheme 1.4 Scheme of the wolframite crystal structure. A= Fe, Mn, Co, Ni, Mg and Zn.	7

List of supporting figures

Figure S 2.2 Rietveld refinement of the powder XRD of the MnWO ₄ catalyst (ID 19116).....	25
Figure S 2.3 Particle size distribution in the thermally treated nano-structured MnWO ₄ catalyst (ID 19116) based on the analysis of approximately 146 particles in TEM images (see for example Figure 2.1a in the main manuscript).	26
Figure S 2.4 HRTEM images and fast Fourier transform (FFT) analysis of two MnWO ₄ nanorods in the catalyst (ID 19116).	26
Figure S 2.5 Inverse Fast Fourier transformation (IFFT) of the 110 spots in Figure 2.1b.....	27

Figure S 2.6 FFT filtered HR-STEM images of MnWO ₄ (ID 19116) a) HAADF, b) inverted HAADF and c) HR-HAADF-STEM images.	28
Figure S 2.7 Raman spectrum of the MnWO ₄ catalyst (ID 19116) (black line) compared to the Raman spectrum of commercial MnWO ₄ (orange line).....	29
Figure S 2.8 HRTEM images and electron diffraction patterns of MnWO ₄ nano-rods.	29
Figure S 2.9 Schematic representation of the crystal structure of MnWO ₄ viewed along a) the [001] axis and b) the [100] axis. White ball represents Mn ²⁺ , green ball represents W ⁶⁺ , red ball represents O ²⁻ (bridging oxygen) and wine ball represents terminal oxygen atoms (tungsten oxygen double bond).....	30
Figure S 2.10 Recorded workflow during hydrothermal synthesis of nano-structured MnWO ₄ ; blue line: pH value measured in the autoclave, red line: temperature of the synthesis gel.....	31
Figure S 2.11 Time on stream plot of propane conversion and selectivity to propene in the oxidative dehydrogenation of propane at T=400°C, and W/F=1.8 g s/ml over nano-structured MnWO ₄ (catalyst ID 19116); The feed was composed of C ₃ H ₈ :O ₂ :N ₂ =10:5:85; The changes in the conversion (X) of propane and the selectivity (S) to propylene and carbon oxides (CO _x : CO + CO ₂) are shown with time on stream.....	32
Figure S 2.12 Mn 2p spectra of nano-structured MnWO ₄ within different detection depths represented by the inelastic mean free path (IMFP) of electrons measured by synchrotron-based NAP-XPS at T=300 °C applying a total pressure of 0.25 mbar O ₂ and He flows of 2 and 2.2 sccm, respectively.....	33
Figure S 2.13 Mn 2p spectra of nano-structured MnWO ₄ within different detection depths represented by the inelastic mean free path (IMFP) of electrons measured by synchrotron-based NAP-XPS at T=300 °C applying a total pressure of 0.25 mbar under different reaction atmospheres; Red lines: O ₂ and He flows of 2 and 2.2 sccm, respectively; Blue lines: O ₂ , C ₃ H ₈ , and He flows of 1, 2, and 1.2 sccm, respectively.....	34
Figure S 2.14 NEXAFS of nano-structured MnWO ₄ measured at the Mn L _{2,3} -edge in total electron yield (TEY) in different reaction atmospheres at T=380°C; Red lines: O ₂ and He flows of 1 and 3.2 sccm, respectively; Blue lines: O ₂ , C ₃ H ₈ , and He flows of 1, 2 and 1.2 sccm, respectively.	35
Figure S 2.15 Temperature-programmed oxidation (TPO) (top), and temperature-programmed reduction (TPR) (bottom) profiles of nano-structured MnWO ₄	36
Figure S 3.1 SEM image of the intermediate formed by reaction of manganese nitrate with sodium tungstate at room temperature.	51
Figure S 3.2 XRD patterns of the hydrothermal products; The pH of the starting solution is provided in the legend of the figure. For allocation of the corresponding final catalyst, please refer to Table 3.1 in the main text.....	52

Figure S 3.3 XRD patterns of the catalysts after activation by thermal treatment of the hydrothermal products in flowing Ar at 400°C.	52
Figure S 3.4 TEM micrographs of as-synthesized (top row) and at 400 °C thermally activated (bottom row) nanostructured MnWO ₄ catalysts with different aspect ratio: 1.5 (a) and (f), 1.7 (b) and (g), 3.2 (c) and (h), 3.9 (d) and (i), 5.1 (e) and (j).	53
Figure S 3.5 Distribution of A) diameter, B) length and C) aspect ratio of the nanostructured MnWO ₄ catalysts after thermal treatment; In each plot, a, b, c, d, and e represent the catalysts AR1.5, AR1.7, AR3.2, AR3.9, and AR5.1, respectively.	53
Figure S 3.6 HAADF_STEM images of MnWO ₄ nanoparticles viewed along <001> with different aspect ratios: a) AR1.5, b) AR5.1 and c) perspective model for a typical faceted nanoparticle.	54
Figure S 3.7 Catalytic performance of top-left) AR1.5, top-right) AR1.7, middle-left) AR3.2, middle-right) AR3.9, and bottom-left) AR5.1 sample in ethanol oxidation reaction at different temperatures; For reaction conditions see Experimental in the main text.	54
Figure S 3.8 Schematic representation of the formation of W-OH groups at (001) planes during dissolution-recrystallization under hydrothermal conditions at 180°C.	55
Figure S 3.9 FTIR spectra of NH ₃ adsorbed at the surface of the catalysts AR1.5, AR1.7, and AR3.9 after pretreatment at 300°C for 1h in vacuum; Adsorption of ammonia was performed at 40°C; The spectra have been recorded in presence of gas phase ammonia ($p=6.508-7.042$ mbar).	55
Figure S 3.10 W 4f spectra (a)), and O 1s spectra (b)) of the catalysts AR1.5 and AR5.1 measured by synchrotron-based near ambient pressure X-ray photoemission spectroscopy (NAP-XPS) at an inelastic mean free path (IMFP) of ca. 1.6 nm in 0.25 mbar in O ₂ /He at a total gas flow of 4.2 sccm at 300°C.	56
Figure S 3.11 Mn 2p spectra of the catalysts AR1.5 and AR5.1 measured by synchrotron-based near ambient pressure X-ray photoemission spectroscopy (NAP-XPS) at an inelastic mean free path (IMFP) of ca. 0.6 nm (a) and 1.6 nm (b) in 0.25 mbar in O ₂ /He at a total gas flow of 4.2 sccm at 300°C.	56
Figure S 4.1 Raman spectra of tungsten containing compounds measured as solids using 633 cm ⁻¹ excitation wavelength.	71
Figure S 4.2 Raman spectra of ammonium paratungstate (APT), ammonium metatungstate (AMT) and sodium tungstate in aqueous solution at room temperature. Bands denoted with asterisks belong to the sapphire window of the Raman probe.	71
Figure S 4.3 Co2p(3/2), O1s and W4f (and 5p3/2) core level XPS spectra of the CoWO ₄ samples after Shirley background subtraction and charging correction.	72
Figure S 4.4 CO ₂ /CO ratio in the ODP reaction over m-WO ₃ , Co ₃ O ₄ and CoWO ₄ catalysts. W/F=1.8-2.4 g s mL ⁻¹ in the oxidative dehydrogenation of propane in a C ₃ H ₈ /O ₂ /N ₂ feed (10:5:85).	73

Figure S 4.5 a) Propene formation, b) CO ₂ formation and c) CO formation rates over m-WO ₃ and CoWO ₄ catalysts. W/F=0.75-2.4 g s mL ⁻¹ in the oxidative dehydrogenation of propane in a C ₃ H ₈ /O ₂ /N ₂ feed (10:5:85).	74
Figure S 4.6 FT-IR spectra of CoW6.2 catalyst in He flow.....	75
Figure S 4.7 FT-IR spectra of CoW7.6 catalyst in He flow.....	75
Figure S 4.8 FT-IR spectra of CoW8.1 catalyst in He flow.....	76
Figure S 4.9 FT-IR spectra of CoW8.5 catalyst in He flow.....	76
Figure S 4.10 Influence of partial pressure of a) propane, b) oxygen and c) water on the specific product formation rate on m-WO ₃ catalyst.	77

List of supporting tables

Table S 2.1 Average crystallite sizes <i>D</i> of the particles in the MnWO ₄ catalyst (ID 19116) along the <i>a</i> , <i>b</i> , and <i>c</i> axis calculated from anisotropic fitting in Rietveld refinement based on the XRD patterns presented in Figure S2.2.	21
Table S 2.2 Intensity ratio of the peaks at 640 and 641.4 eV in the NEXAFS of nano-structured MnWO ₄ at the Mn L _{2,3} -edge. The spectra in Total Energy Yield (TEY) are presented in Figure S2.14.	22
Table S 2.3 Hydrogen consumption during TPR and oxygen consumption during TPO experiments with nano-structured MnWO ₄	22
Table S 2.4 Chemical composition of the washing solution after treatment of nano-structured MnWO ₄ with nitric acid as determined by XRF.....	23

Table of contents

Acknowledgement	I
Abstract.....	III
Zusammenfassung.....	V
List of figures.....	VII
List of tables.....	IX
List of schemes	IX
List of supporting figures.....	IX
List of supporting tables.....	XII
1 Introduction.....	1
1.1 Lower alkane utilization	1
1.2 Reaction networks and mechanisms in ODP reaction on metal oxide catalysts.....	1
1.3 Active site in oxidative dehydrogenation of propane	3
1.4 Nano-structuring of metal oxide	3
1.5 Surface termination of bulk metal oxides under reaction condition	4
1.6 Metal tungstate in the wolframite crystal structure.....	6
1.7 Motivation and aim of the thesis.....	7
1.8 Outline of the thesis	8
2 Selective Alkane Oxidation by Manganese Oxide: Site Isolation of MnO _x Chains at the Surface of MnWO ₄ Nanorods	9
2.1 Introduction:	9
2.2 Results and discussion:	10
2.3 Conclusion:	16
2.4 Experimental details:	17
2.4.1 Synthesis of the catalyst.....	17
2.4.2 Catalyst characterization	18
2.5 Supporting information.....	21
2.5.1 Supporting tables.....	21
2.5.2 Supporting figures.....	24
2.6 Acknowledgements.....	36

3	Hydrothermal Synthesis of Bi-functional Nanostructured Manganese Tungstate Catalysts for Selective Oxidation	37
3.1	Introduction:	37
3.2	Results and discussion	38
3.2.1	Phase formation and particle growth under hydrothermal conditions	38
3.2.2	Ethanol oxidation	43
3.3	Conclusions	48
3.4	Experimental details	49
3.4.1	Hydrothermal synthesis.....	49
3.4.2	Characterization of catalysts	50
3.5	Supporting information.....	51
3.6	Acknowledgement	57
4	Hydrothermal Synthesis and Characterization of Nanostructured CoWO ₄ as Catalysts for Oxidative Dehydrogenation of Propane.....	58
4.1	Introduction:	58
4.2	Results and discussion	59
4.3	Conclusions	68
4.4	Experimental details:	69
4.4.1	Synthesis of the catalysts	69
4.4.2	Catalyst characterization	69
4.5	Supporting information.....	70
5	Conclusions.....	78
6	Bibliography	80
	Appendix.....	88
	Curriculum vitae	88

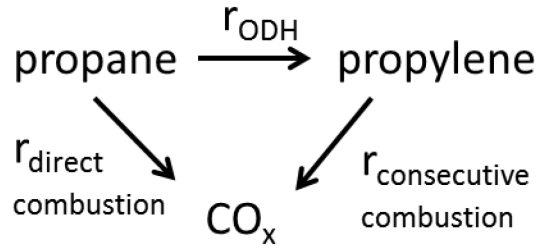
1 Introduction

1.1 Lower alkane utilization

Efficient utilization of lower alkanes (methane, ethane, propane and *n*-butane) to produce chemical intermediates, such as olefins and oxygenates, is economically attractive from a practical perspective because of their abundance and cheaper prices compared to their olefin counterparts. However, industrial applications of direct transformation of alkanes are limited due to insufficient selectivity and activity.[2] Currently, selective oxidation of *n*-butane to maleic anhydride on the so-called VPO catalyst is the only industrial process in selective oxidation using saturated alkane as feedstock.[3] In response to the low price of “shale gas”, the chemical industry shifted from naphtha towards ethane in the steam cracking process, which led to a lack of propylene and butadiene supplies. However, the increasing demand for propylene motivates “on purpose” production of it. Direct catalytic dehydrogenation of propane (DHP) to propylene is one of the solutions, but it requires low price pure propane resources. The current DHP industrial processes uses Pt-based catalysts[4]. However, the catalyst suffers from deactivation due to coke formation, and the conversion of the catalytic reaction is limited by thermodynamics caused by the endothermic nature of the reaction. On the other hand, oxidative dehydrogenation of propane (ODP) is advantageous since no coke formation and no thermodynamic limitations occur. Bulk or supported (mixed) metal oxides are the most promising catalytic material investigated.[5, 6] Vanadium containing oxides[7], molybdates [8, 9], tungstates[10] and cobalt and nickel containing mixed metal oxides are representative redox-type catalysts. At high temperatures it is also possible to activate propane by non-redox active materials. Despite the fact that a large number of catalytic materials has been investigated, the low selectivity to propylene still leaves the ODP process far away from industrial application. So far it is not comprehensively clear which factors determine selectivity in the catalytic oxidation of short-chain alkanes. To fully understand the structure-function relationships, deeper understanding of the reaction network is required.

1.2 Reaction networks and mechanisms in ODP reaction on metal oxide catalysts

The reaction network shown in Scheme 1.1 has been proposed for supported vanadium, molybdenum and tungsten oxide catalysts including direct combustion of propane and consecutive combustion of propylene as main unselective pathways.[11, 12]



Scheme 1.1 Reaction network (adapted from ref. [11]) on supported V-, Mo- and W-oxide catalysts.

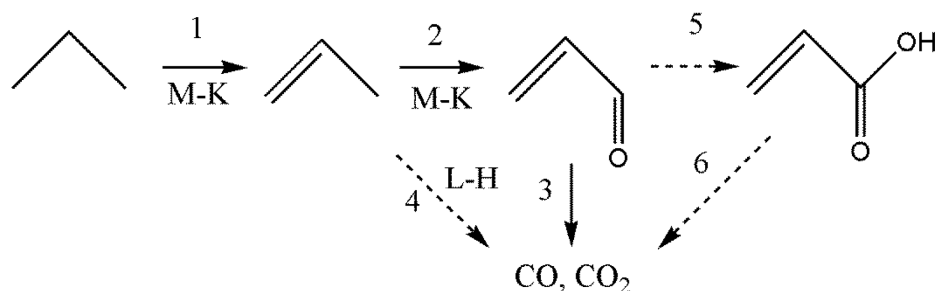
Irreversible C-H bond scission *via* abstraction of the first hydrogen atom in adsorbed propane (equ. 1.1) by nucleophilic oxygen species was suggested to be the rate-determining step (equ. 1.2) of the entire reaction on a supported vanadium oxide catalysts.[13] After two consecutive C-H bond abstraction reactions (eqs. 1.2 and 1.3), oxygen vacancies can be re-created by recombination of the hydroxyl groups formed (equ. 1.4). Gas phase oxygen molecules then fill the oxygen vacancies, completing the catalytic cycles (equ. 1.5).



Micro-kinetic investigations on supported and bulk vanadium oxide catalysts shows that the apparent reaction order of propane consumption is close to propane and close to 0 with respect to oxygen. The macrokinetics have been successfully treated using a following rate expression.[7]

$$r_{\text{C}_3\text{H}_8} = k P_{\text{C}_3\text{H}_8}^1 P_{\text{O}_2}^0 \quad (2.1)$$

However, on $\text{Co}_{0.5}\text{Ni}_{0.5}\text{MoO}_4$ catalysts, the reaction order of propane consumption with respect to propane partial pressure is close to 1, but the reaction order of carbon oxides formation with respect to oxygen partial pressure is close to 0.5.[9] It was suggested that the formation of propene follows a Mars-van Krevelen-type mechanism (Scheme 1.2, step 1) but the formation of carbon oxides from propene follows a Langmuir-Hinshelwood mechanism (Scheme 1.2, step 4). In other words, it was suggested that lattice oxygen is responsible for propene formation whereas dissociatively chemisorbed oxygen species are responsible for total oxidation of propene. A similar dependence of rates for propane consumption and carbon oxides formation on the partial pressures of propane and oxygen was reported on a $\text{Mg}_4\text{V}_2\text{Sb}_2\text{O}_x$ catalyst.[14, 15]



Scheme 1.2 Reaction network (adapted from ref. [9]) on $\text{Co}_{0.5}\text{Ni}_{0.5}\text{MoO}_4$.

Some other types of reaction mechanism were also proposed.[16] In general, limited propene selectivity on vanadium-based catalysts was attributed to consecutive combustion of propene.[12, 17] Supported molybdenum and tungsten oxide catalysts also suffer from such problems.[11] However, the consecutive combustion of propene was less severe on the $\text{Co}_{0.5}\text{Ni}_{0.5}\text{MoO}_4$. [9] Furthermore, in the catalytic cycle on supported vanadium oxide catalysts, it was generally believed that C-H bond activation proceeds much more slowly than the re-oxidation of the oxide.[18-21] The rate of the former step was estimated as 10^2 to 10^5 times as that of the latter step, depending on the structure of the vanadium oxide.[18, 19]

1.3 Active site in oxidative dehydrogenation of propane

The nature of the active site has an impact on the reaction network.[22] The active sites on supported vanadium oxide catalysts contain V-O moieties, although an unambiguous assignment of spectroscopic features to V=O, V-O-V or V-O-(Support) species has not been achieved so far.[23] In a study of Ni-W-O mixed metal oxide catalysts in the oxidative dehydrogenation of ethane, Ni-O sites were proposed as active sites.[24]

To be noted, site isolation was brought up as a very important concept guiding the improvement of selectivity for selective oxidation catalysts.[6, 25, 26] The following hypothesis has been proposed by Grasselli *et al.*: “Reactive surface lattice oxygens must be spatially isolated from each other in defined groupings on a catalyst surface to achieve selectivity. The number of oxygens in a given isolated grouping (domain) would determine the reaction channel through the stoichiometry requirements imposed on the reaction by the availability of oxygens, or lack thereof, at the reaction site”.

1.4 Nano-structuring of metal oxide

Nano-structuring of metal oxide catalyst is important not only because of higher surface areas possessed by the nanoparticles. The synthetic techniques developed during the recent “Nano Rush” can actually produce nanoparticles with tailored morphology and size, these are important in determining the surface geometric structure, *i.e.* facets exposure, and electronic structure of the

synthesized solids.[27] Moreover, morphology has been found to have important influences on catalytic properties of nano-crystalline metal oxides.[28, 29] Different intrinsic reaction rates have been found over the differently-shaped nanostructured metal oxides exposing various crystal planes, as exemplified by the research concerning Co_3O_4 , [30, 31] CeO_2 [32-34] and Cu_2O [35]. It has been proposed that mono-atomic step sites on the surface of MgO are the active sites for the oxidative coupling of methane,[36, 37] illustrating the important role of surface defects.

1.5 Surface termination of bulk metal oxides under reaction condition

A full understanding of the activity-structure relationship is, however, very challenging, since the complexity of the surface structure of metal oxides regarding surface termination mode (metal termination or oxygen termination),[38] hydroxylation, defects[39-41] and metal oxidation state is high although in some cases the prepared catalysts exposed regular facets. For example, the surface

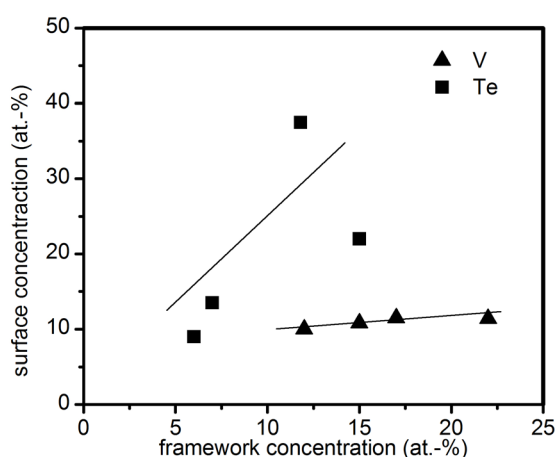
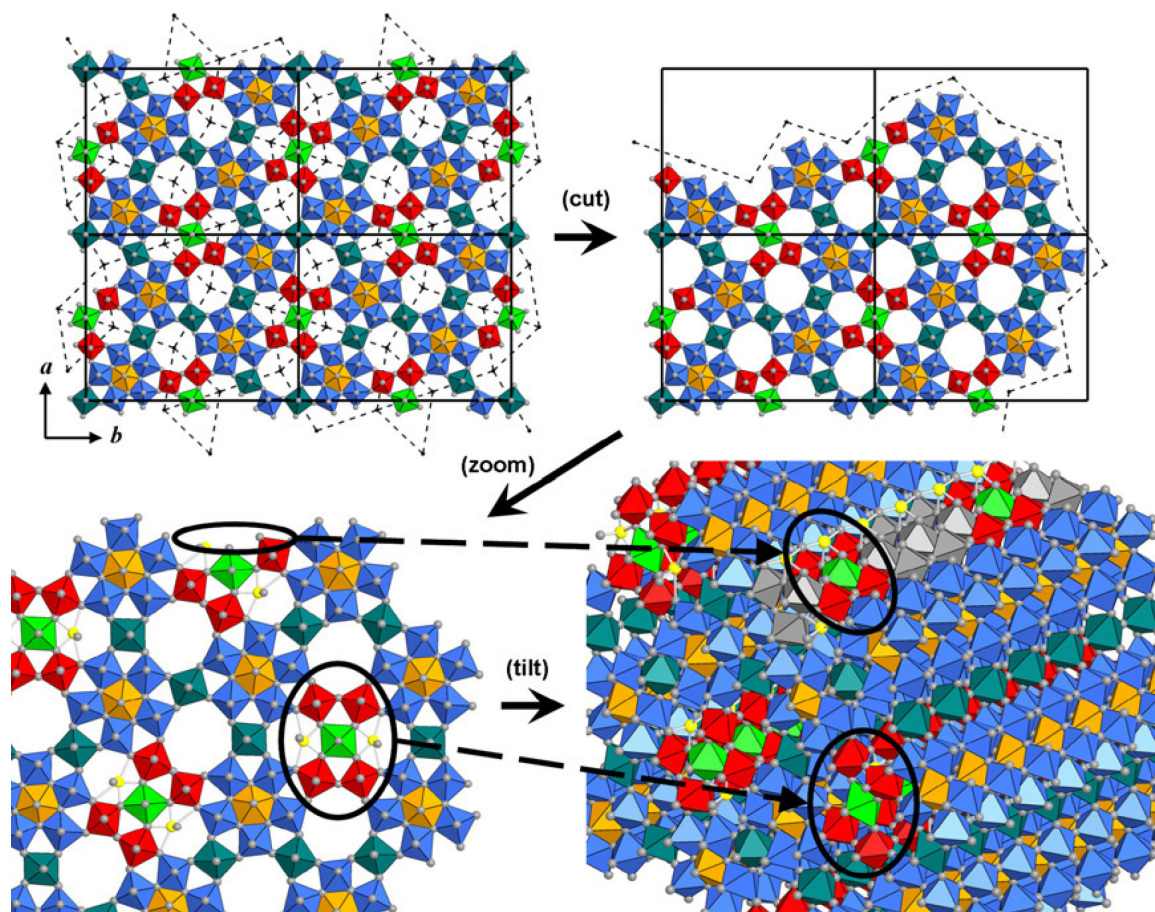


Figure 1.1 Near surface concentration of Te and V determined by XPS (escape depth 0.8 nm) at $T=298\text{ K}$, $p=30\text{ Pa O}_2$ as a function of the concentration in the crystalline M1 framework measured by EDX (redrawn from ref. [1]).

elemental composition of a Mo-V-Te-Nb-O mixed oxide in M1 crystal phase is different from that of the bulk (Figure 1.1). The difference might be partly attributed to the openness of the 6 or 7-membered rings at the surface, which then liberates Te originally contained in these closed channels (Scheme 1.3).



Scheme 1.3 Termination model of the M1 phase (reproduced from ref. [42]).

The surface termination mode was also investigated by transmission electron microscopy (Figure 1.2). More importantly, dynamic rearrangements of the catalyst surface responding to temperature and gas atmospheres have been observed. In situ synchrotron based X-ray photoelectron spectroscopic experiments indicate the formation of two-dimensional vanadium oxide layers terminating crystalline vanadium-containing phases, such as $(VO)_2P_2O_7$ and Mo-V-Te-Nb-O composed the M1 phase.[1, 42-45] The surface layer deviates significantly from the bulk crystal structure in terms of elemental composition and the vanadium oxidation state.

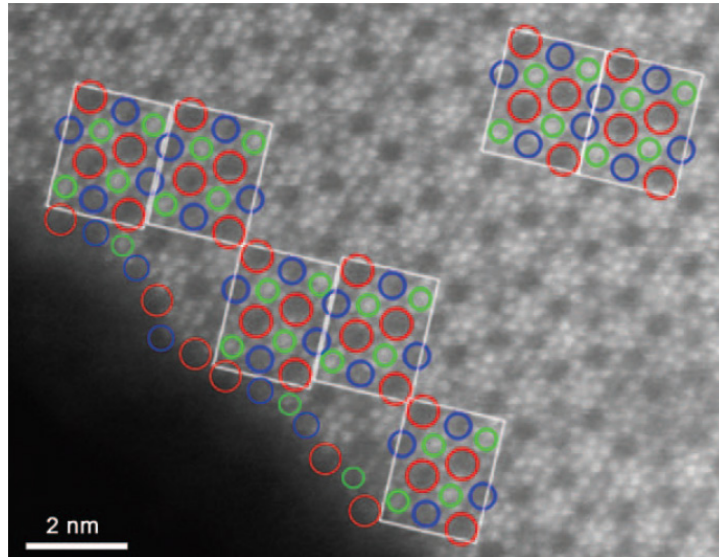
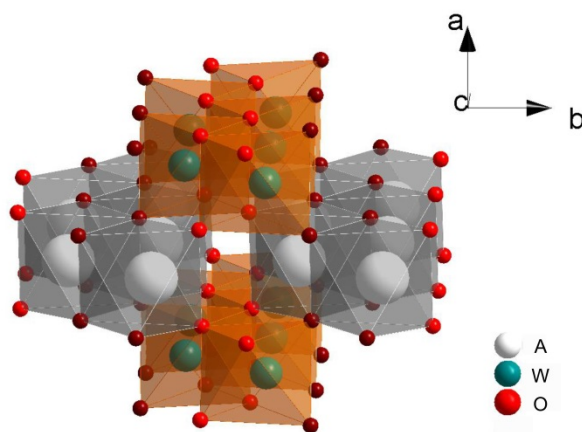


Figure 1.2 STEM image of one M1 particle along the $\langle 001 \rangle$ direction. Red and blue circles highlight heptagonal and hexagonal open channels, respectively. Green circles highlight the $M\{M_5\}$ structure. The bright dots represent columns of M-O polyhedra (reproduced from ref. [46]).

1.6 Metal tungstate in the wolframite crystal structure

Metal tungstates AWO_4 (A is bivalent ions with relatively small radius, such as Fe, Mn, Co, Ni, Mg, and Zn) crystallize in the wolframite-type structure. Metal tungstate materials attract much scientific interest in various fields such as in photonics and photoelectronics.[47, 48] Especially, optical (phonon) properties,[49, 50] electronic structure,[51-53] conductivity[54, 55] and magnetic properties[56, 57] of manganese tungstate have been widely investigated. In the wolframite crystal structure (Scheme 1.4), distorted WO_6 motifs form zigzag chains by edge sharing oxygen atoms along the c axis and bi-valent transition metal ions fill in the octahedrons by corner sharing oxygen atoms with WO_6 clusters forming also zigzag chains along the same crystallographic axis. Along the a axis the two types of zigzag chains stack alternately by edge sharing.



Scheme 1.4 Scheme of the wolframite crystal structure. A= Fe, Mn, Co, Ni, Mg and Zn.

1.7 Motivation and aim of the thesis

From the viewpoint of searching for new catalytic materials for selective activation of lower alkanes, a novel strategy is needed. Despite comprehensive investigation, the performance of vanadium-based materials is still far from industrial application. In the case of ODH of propane, selectivity to propene at high propane conversions is limited due to consecutive oxidation of propene. On the other hand, deeper understanding of the reaction network and mechanism of the oxidative dehydrogenation of propane and the nature of active site would be very beneficial for designing new catalytic materials. As outlined above, site isolation has been postulated as an important requirement for selectivity in partial oxidation on oxide catalysts. The surface structure of the vanadium-based multi-metal mixed oxide catalysts is extremely complex and dynamic as has been introduced above.

The aim of the thesis is, therefore, to gain knowledge about the structure-function relationships in propane activation over mixed metal oxides by reducing the chemical complexity of the catalyst. Metal tungstates have been chosen, since these oxide materials contain only of two metals. The tungstate motifs are supposed to provide a structure-stabilizing matrix that hosts redox-active metals, such as Mn, Fe, Ni, or Co.

This work focuses in particular on the influence of the morphology and surface termination of the catalyst particles on the oxidative dehydrogenation of propane over manganese and cobalt tungstate catalysts. Morphology and surface termination of catalyst particles will be tuned by systematic variation of the synthetic parameters. The iso-structure shared by the wolframite family renders comparative studies of the effect of composition in terms of the redox-active element possible. Besides hydrothermally synthesized tungstates, commercial manganese tungstate, cobalt oxide

(Co₃O₄), manganese oxides (MnO, Mn₃O₄, Mn₂O₃, MnO₂) and mesoporous tungsten trioxide have been included as references.

1.8 Outline of the thesis

In Chapter 2, the discovery of unexpected activity and selectivity of rod-shaped nanostructured manganese tungstate in the oxidative dehydrogenation of propane is discussed. The selectivity to propene over the mixed metal oxide is much higher than that over the binary manganese or tungsten oxides, respectively. The performance of the catalyst is attributed to “site isolation” of surface manganese oxide chains. The unique surface structure was formed under specific hydrothermal synthesis conditions.

In Chapter 3, hydrothermal synthesis of a series of manganese tungstate is described. The influence of acidity and basicity in the synthesis gel on the aspect ratio of the synthesized nanostructured manganese tungstate particles is highlighted. A “dissolution-re-crystallization” mechanism during the aging process of the hydrothermal synthesis was proposed to be responsible for the anisotropic crystal growth. The aspect ratio was found to determine the acid-base and redox properties of the catalysts.

In Chapter 4, hydrothermal synthesis of cobalt tungstate is illustrated. Again, a variation of the initial pH in the autoclave resulted in differently shaped nanostructured cobalt tungstate particles. Surface termination by cobalt oxide species was found to be beneficial for both activity and selectivity in the oxidative dehydrogenation of propane.

In Chapter 5, final conclusions and an outlook are given.

2 Selective Alkane Oxidation by Manganese Oxide: Site Isolation of MnO_x Chains at the Surface of MnWO₄ Nanorods¹

Abstract: The electronic and structural properties of vanadium-containing phases govern the formation of isolated active sites at the surface of these catalysts for selective alkane oxidation. This concept is not restricted to vanadium oxide. The deliberate use of hydrothermal techniques can turn the typical combustion catalyst manganese oxide into a selective catalyst for oxidative propane dehydrogenation. Nanostructured, crystalline MnWO₄ serves as the support that stabilizes a defect-rich MnO_x surface phase. Oxygen defects can be reversibly replenished and depleted at the reaction temperature. Terminating MnO_x zigzag chains on the (010) crystal planes are suspected to bear structurally site-isolated oxygen defects that account for the unexpectedly good performance of the catalyst in propane activation.

Keywords: propane oxidative dehydrogenation • hydrothermal synthesis • in situ Raman • manganese tungstate • heterogeneous catalysis

2.1 Introduction:

Prospective changes in the raw material basis in chemical industry to alternative feedstock bear new scientific challenges. This tackles, in particular, the area of oxidation catalysis where small saturated hydrocarbon molecules are going to be used as building blocks for olefins and aromatics.[58] The activation of inert C-H bonds in alkanes requires highly active catalysts. Often, high activity entails low selectivity due to over-oxidation of more reactive intermediates and desired products to CO and CO₂. [59] Vanadium oxide is the most prominent material that has been widely studied in selective oxidation of hydrocarbons and oxygenates.[7, 13, 60-64] Surface-sensitive *in-situ* experiments indicate that some well-known selective catalysts, composed of crystalline V-containing phases, are terminated by two-dimensional vanadium oxide layers.[1, 42-45, 65-69] These layers deviate in terms of composition and oxidation state of V significantly from the bulk crystal structure. The layer accounts for dynamic charge transfer between bulk and surface. This is reflected in the gas-phase-dependent response of the work function, electron affinity, and surface potential barrier, which was

¹The following chapter is the submitted version of [104], the peer reviewed published version can be found with publisher DOI link: <http://dx.doi.org/10.1002/anie.201510201>

not found for the less selective bulk V₂O₅.^[68]

2.2 Results and discussion:

Herein, we conceptually verified that the selectivity of other unselective oxides, like Mn oxide, is also tunable by applying this extended site-isolation approach. We present the first example of a vanadium-free analogue that accomplishes efficient activation of propane by establishing a two dimensional Mn oxide layer in form of MnO_x chains at the surface of phase-pure, rod-shaped, nanostructured MnWO₄ (Figure 1, Figure S2.1). The catalyst was prepared by hydrothermal synthesis. The synthesis procedure reported previously,^[70] was modified in the current work (description provided in the Supporting Information).

Phase purity of the synthesis product was confirmed by Rietveld refinement of powder X-ray diffraction (Figure S2.2) applying anisotropic fitting. Transmission electron microscopy (TEM) imaging reveals typical rod-shaped nanoparticles with diameters varying from 13 to 51 nm (Figure 1 a-b, Figure S2.3). Fast Fourier transform (FFT) analysis of bright field TEM images of several particles (Figure S2.4) indicates in contrast to a former report^[70] the preferential growth of the rods along the [001] direction. In addition, the power spectrum in Figure 1b reveals elongated spots, in particular for the (011) direction indicating a defective structure. Inverse Fast Fourier transformation (IFFT) of the 011 spots (Figure S2.5) indicates the occurrence of planar defects within the lattice. From the basal-area of two condensed nano-rods (Figure 2.1c) surface terminations can be distinguished that include (010), (110) and (100) planes. The dimensions of the oriented particles in *a* and *b* direction shown in Figure 1c are in reasonable agreement with the average crystallite size determined by anisotropic Rietveld refinement (Table S2.1). This implies that the particles chosen for TEM analysis are good representatives of the polycrystalline powder catalyst. A few bigger particles are also found by TEM (Fig. 2.1b). The atomic resolution high angle annular dark field- scanning transmission electron microscopy (HAADF-STEM) images (Figure 2.1d and e) viewed along [001] indicate the presence of two kinds of atomic dumbbells which can be distinguished by their different contrast. In HAADF-STEM the contrast is due to Rutherford scattering proportional to approximately Z^2 . Thus, the dumbbells can be attributed to W₂O₈ (high contrast) and Mn₂O_y (less contrast) dimers. In the schematic representation of the MnWO₄ crystal structure they correspond to the orange and white edge-sharing octahedrons, respectively (Figure 2.1f).

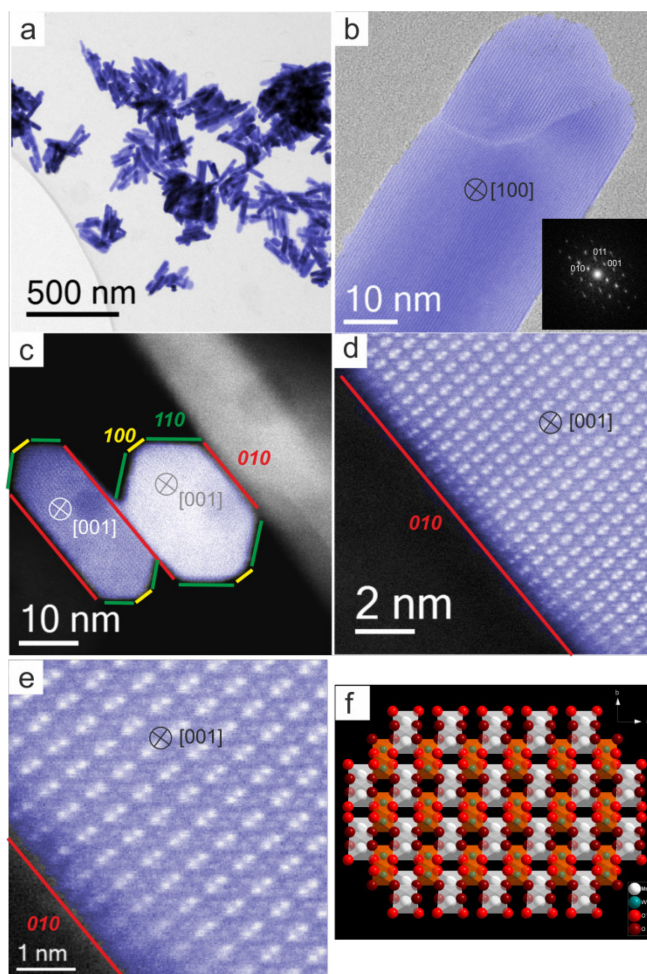


Figure 2.1 (S)TEM analysis of the MnWO₄ powder catalyst: a) Overview TEM micrograph of the MnWO₄ nanorods; b) HRTEM image of one nanorod particle viewed along [100]. The inset denotes the power spectra recorded on either side of the defect; c) HAADF-STEM image of condensed [001] oriented MnWO₄ nanorods. The surface termination was identified by phase analysis of corresponding atomic resolution HAADF-STEM images; d) and e) atomic resolution HAADF-STEM images of (c); f) Schematic representation of the crystal structure of MnWO₄ viewed along [001]. The Mn atoms are presented in white, W is coloured green and O atoms are displayed in red. The original images are given in the SI (Figure S2.1, 6c).

Atomic resolution HAADF-STEM images of the surface structure of the (010) plane viewed along [001] are shown in Figure 2.2 and illustrate a preferential surface exposure of Mn ions as unimers or dimers. The images indicate a slight out of center shift of some Mn ions compared to their bulk crystallographic position.

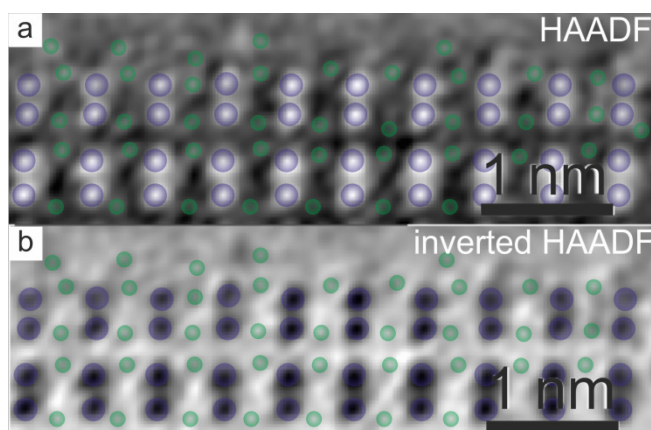


Figure 2.2 Surface termination of the *b* plane viewed along the growth direction [001] by FFT filtered atomic resolution STEM images a) HAADF, and b) inverted HAADF; The violet and green circles denote W and Mn atoms, respectively. The micrographs correspond to magnified images of Figure 1d. Original images are given in the SI (Figure S2.6).

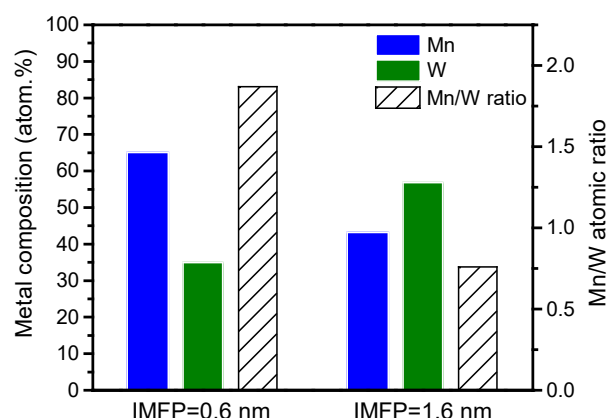


Figure 2.3 Depth profile of elemental composition of MnWO₄ nano-rods at two different depths represented by the inelastic mean free path (IMFP) of electrons measured by synchrotron-based NAP-XPS at T=300°C applying a total pressure of 0.25 mbar O₂ and He at flows of 2 and 2.2 sccm, respectively.

The Raman spectrum (Figure S7) of the nano-structured MnWO₄ agrees well with the spectrum of crystalline MnWO₄.^[49, 50] However, two additional, previously unreported bands appear at 615 and 665 cm⁻¹. Since phase purity and high crystallinity of the nano-structured material has been confirmed by TEM (Figure 1 and Figure S2.8) and XRD (Figure S2.2), these two bands are attributed to the MnO_x clusters at the surface of the nano-rods (Figure S2.9) that have been visualized by STEM (Figure 2.2).^[71, 72]

Synchrotron-based near ambient pressure X-ray photoelectron spectroscopy (NAP-XPS) reveals the enrichment of Mn on the outmost surface (Inelastic mean free path (IMFP) = 0.6 nm), within which the molar ratio of Mn to W is 1.9 (Figure 2.3). The Mn/W ratio decreases to 0.8 in the sub-surface (IMFP = 1.6 nm), which is close to bulk stoichiometry of Mn and W.

In summary, an enrichment of the surface of MnWO₄ nano-rods with manganese in the phase-pure, highly crystalline material was indicated by photoelectron spectroscopy. The specific surface termination is also reflected in the Raman spectrum. In line with these integral methods, the locally resolved atomic resolution HAADF-STEM images (Figure 2.2) present a partial Mn surface termination of the (010) planes. Thus, it is possible that the Mn enrichment observed by integral methods could be primarily attributed to an increased occurrence of the Mn terminated (010) planes (Figure 2.2) in the nano-structured material.

The specific surface / nano-structure of MnWO₄ is generated under hydrothermal conditions. *In-situ* Raman spectra taken during the synthesis (Figure 2.4) provide important information on the phase formation of MnWO₄. MnWO₄ nano-rods develop at around 125°C while the mixture of the aqueous solutions of Na₂WO₄ and Mn(NO₃)₂ is heated in the autoclave (Figure S2.10). An intermediate (910 cm⁻¹) is transformed to crystalline MnWO₄, indicated by the appearance of bands at 884, 325, 397, 510, 544, 672 and 698 cm⁻¹. The strongest band at 884 cm⁻¹ has been assigned to the stretching mode of W=O in distorted WO₆ octahedrons.[49, 50] Interestingly, two new bands at 615 and 665 cm⁻¹ assigned to surface MnO_x clusters[71, 72] grow in intensity with time when the synthesis temperature of 180°C has been reached. These changes in the Raman spectra are attributed to dissolution-recrystallization processes that most likely lead to the unique rod-shaped nano-structure and the specific surface modification of the nano-structured material. MnWO₄ crystallizes in a monoclinic structure (wolframite-type, ICSD-67906) in which WO₆ clusters form zigzag chains by sharing edges along the [001] axis (Figure S2.9). In the basic medium under hydrothermal conditions (pH=9), WO_x clusters on the surface of the (010) planes could be dissolved due to the nucleophilic attack of OH⁻ ions at the bridging W-O-W bonds (Equation 1) leaving behind leached (010) surfaces composed of MnO_x zigzag chains. Subsequently, the bridging oxygen anions at the (001) surface may condense with the dissolved WO₄²⁻ monomers (shoulder at 926 cm⁻¹ in Figure 2.4). Hence, the zigzag chains will propagate in one dimension by forming new O-W-O edge-sharing bridging bonds. Such a dissolution-recrystallization process may result in the observed anisotropic crystal growth along the [001] axis resulting in the rod-shaped morphology of the MnWO₄ particles.

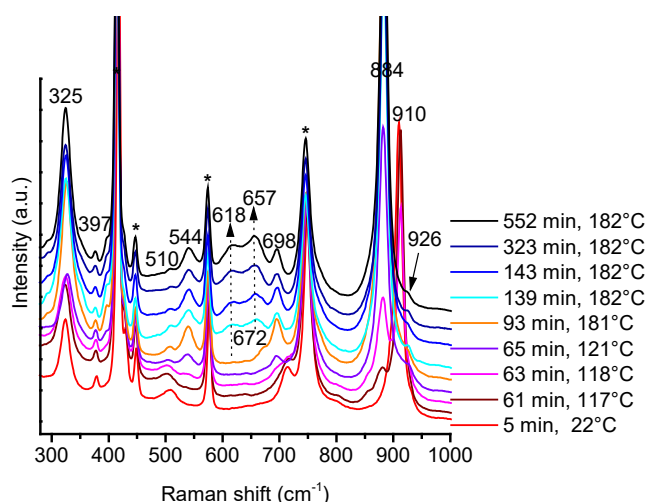
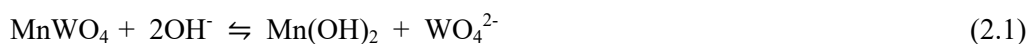


Figure 2.4 *In-situ* Raman spectra in the 280-1000 cm⁻¹ range measured during hydrothermal synthesis of MnWO₄ nano-rods; Bands denoted with asterisks belong to the sapphire window of the Raman probe.



The nano-structured MnWO₄ material was studied as a catalyst in oxidative dehydrogenation of propane. Conventional bulk crystalline MnWO₄ is rather inactive in the reaction, which is reflected in no measurable conversion at 450°C (reaction conditions described in the Supporting Information). Nano-structuring, however, as achieved by hydrothermal synthesis in the present work, can turn this material into an active catalyst. Moreover, the unique surface structure of the MnWO₄ nanorods exhibits superior selectivity to the desired product propylene than bulk manganese oxide (Figure 2.5). Manganese oxide is very active (Table 2.1), but not very selective and transforms propane almost completely into carbon oxides. Electronic modification and/or geometric separation of the MnO_x zigzag chains on the (010) planes by W₂O₈ units (Figure 2.2) apparently account for the improved performance. Propane conversion has been changed by varying the contact time at 400°C (Figure 2.5). The comparatively low temperature was chosen to avoid the influence of homogeneous gas phase reactions, which normally contribute to non-negligible conversion at elevated reaction temperatures above 450°C. The catalytic performance of MnWO₄ nano-rods reached steady state after 70 hours on stream and showed no sign of deactivation within 108 hours (Figure S2.11). Importantly, Mn terminating MnWO₄ nano-rods exhibit much higher apparent turnover frequency (TOF) than vanadium oxide species supported on silica (Table 2.1) when all Mn atoms at the (010) surfaces and all V atoms are taken into account as active sites. In reality, the number of active sites at the surface of the MnWO₄ nano-rods is, however, perhaps much lower. The Mn 2p XPS spectra (Figure S2.12) indicate the predominance of Mn in oxidation state two at the surface and within the subsurface. Tiny

differences have been observed in the spectra under different reaction atmospheres (Figure S2.13), however, the interpretation of the Mn 2p spectra is not straightforward due to less distinct variations in the binding energies of compounds containing Mn in different oxidation states, an elaborate multiplet splitting, and the appearance of satellites.[73, 74] In contrast, near edge X-ray absorption fine structure (NEXAFS) is sensitive to detect the surface oxidation of manganese oxides,[75, 76] and changes in the coordination environment of the Mn ions.[77] The measured line shape of the Mn L_{2,3}-edge (Figure S2.14) agrees well with those from large single crystals of MnWO₄. [57, 78] A predominance of Mn in oxidation state two is confirmed by the spectra both in oxygen and reaction atmosphere. Nevertheless, a small increase in the intensity ratio of the peaks at 640.0 and 641.4 eV has been observed during reaction (Table S2.2). With increasing oxidation state or, in other words, with increasing coordination of the Mn ions by oxygen atoms, intensity in the Mn L_{2,3}-edge spectrum occurs at higher energy.[75, 76] Hence, the changes in the intensity ratio of the peaks at 640.0 and 641.4 eV indicate that in reaction feed the concentration of oxygen defects is higher compared to oxygen atmosphere suggesting a substantial impact of oxygen defects on catalyst performance. Oxygen defects have been quantified by temperature-programmed oxidation (TPO) and reduction (TPR) cycles (Figure S15). Before first TPO run, the catalyst was heated in Argon at 400°C for 2 hours. Approximately 3 oxygen atoms per nm² could be replenished after this treatment (Table S2.3). This underlines the notion[22, 79] that only a fraction of surface atoms is catalytically active, which, however, holds great challenges in terms of the identification of active sites. The very similar hydrogen consumption profiles of the two TPR runs indicate that approximately 5% of the surface oxygen atoms were reversibly removed by reaction with H₂ (Table S2.3). In addition, twice as much oxygen atoms were replenished during the first TPO, indicating a higher oxygen vacancy density after Ar treatment, which was also reflected by the higher initial activity in oxidative dehydrogenation of propane during the first 18 hours on stream (Figure S2.11).

After washing with nitric acid solution and re-calcination under the same condition as that of the pristine MnWO₄ nano-rods, the catalytic activity decreased dramatically (Table 2.1). Only Mn was detected in the washing solution (Table S2.4). This further corroborates our argument that surface MnO_x chains are the active sites of the nano-structured MnWO₄ catalyst in oxidative dehydrogenation of propane.

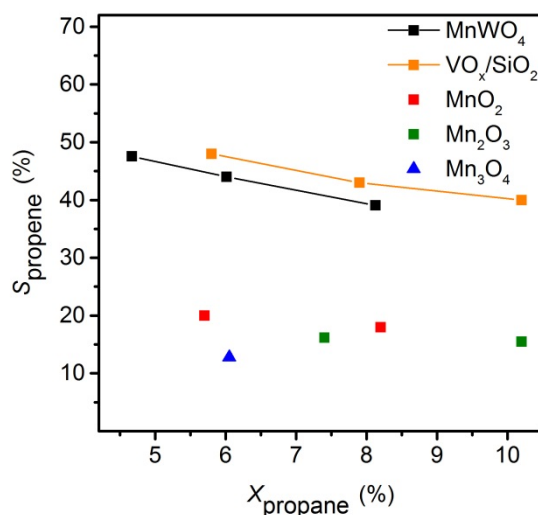


Figure 2.5 Catalytic performance of nano-structured MnWO_4 ($T=400^\circ\text{C}$, $W/F=1.8\text{--}0.9\text{ g s/ml}$) in comparison to VO_x/SiO_2 ($T=400\text{--}420^\circ\text{C}$, $W/F=1.8\text{ g s/ml}$) and various manganese oxides ($T=330\text{--}395^\circ\text{C}$, $W/F=1.8\text{ g s/ml}$) in the oxidative dehydrogenation of propane in a feed composed of $\text{C}_3\text{H}_8:\text{O}_2:\text{N}_2$ in a ratio of 10:5:85. The selectivity to propene is shown as a function of propane conversion. Other C-containing products are mainly CO and CO_2 .

Table 2.1. Active site density and reactivity of the catalysts in the oxidative dehydrogenation of propane at $T=400^\circ\text{C}$, $W/F=1.8\text{ g s/ml}$ in a feed composed of $\text{C}_3\text{H}_8:\text{O}_2:\text{N}_2$ in a ratio of 10:5:85.

Catalyst	MnWO_4 nanorods	Acid-washed MnWO_4 ^[a]	VO_x/SiO_2 ^[b]	Mn_2O_3
$r_{\text{C}_3\text{H}_8}$ [$\times 10^{-9}\text{ mol m}^{-2}\text{ s}^{-1}$]	8.69	2.46	0.27	550
Active-site density [nm^{-2}]	8.3 ^[c] /3 ^[d]	–	1.0	10.2 ^[e]
TOF [$\times 10^{-3}\text{ s}^{-1}$]	0.63/1.7	–	0.16	33

[a] Treatment described in the Supporting Information. [b] VO_x supported on modified SBA-15 with a surface vanadium density of 1 V atom/ nm^2 . [c] Assuming that only MnO_x species on (010) surface planes are active. [d] Assuming that only oxygen defect sites on the surface are active sites. [e] Mn density on the (100) plane.

2.3 Conclusion:

In summary, we demonstrated that a catalytically inactive solid, like MnWO_4 , was converted into a highly active and selective catalyst by knowledge-based synthesis. Hydrothermal techniques guided by *in-situ* spectroscopy[80] have been applied to control the surface termination. *In-situ* Raman

spectroscopy provided insight into molecular processes of crystallization, surface dissolution and recrystallization under hydrothermal conditions. The unique self-supported structure of one-dimensional MnO_x clusters at the surface of nano-structured MnWO₄ demonstrates the importance of understanding the synthetic inorganic chemistry from a molecular point of view[81] and the significance of studying the surface termination[1, 42, 46] of well-defined nano-structured metal oxides[82]. By identification of the highly active surface MnO_x on the MnWO₄ nano-rods, the promotional effect of Mn in many catalytic systems could be better understood. The design of selective oxidation catalysts will benefit from this knowledge and it will lead to an improvement of current Mn doped catalytic systems.

2.4 Experimental details:

2.4.1 Synthesis of the catalyst

2.4.1.1 Starting materials

Mn(NO₃)₂·4H₂O (98%, Roth), Na₂WO₄·2H₂O (99%, Sigma Aldrich), NaOH (98%, Alfa Aesar), were used as received. Ultrapure water was obtained by using the Milli-Q Synthesis System (MQ). Commercial MnWO₄ (ID 18507) used as reference catalyst was purchased from Alfa Aesar (99.9% metal basis, 200 mesh powder), the powder was then pressed and sieved to a particle size of 250-355 µm for catalytic testing.

2.4.1.2 Hydrothermal synthesis of nano-structured MnWO₄

Nano-structured MnWO₄ was synthesized by a method modified from literature.[70] In the first step, an aqueous 0.2 M solution of Mn(NO₃)₂ was added to an aqueous 0.2 M solution of Na₂WO₄ while stirring at 295 K. In the second step, 5.8 mL of an aqueous 0.1 M NaOH solution was added to adjust the pH value to 9.9. In the third step, the mixture was transferred to an analytical autoclave HPM-PT-040 (Premex Reactor GmbH), and the temperature was raised from 295 K to 453 K at a rate of 5 K/min. Hydrothermal synthesis was performed at 453 K at autogenous pressure for 12 h. During hydrothermal synthesis the pH was recorded (Figure S10) using a pH probe (ZrO₂ probe Model A2 and Ag/AgCl reference electrode, both with a 1/2" outer tubing made from C-276; Corr Instruments). In the fourth step, the solid product was separated from the mother liquor by centrifugation, and washed twice with de-ionized water. In the final step, the solid was dried in a muffle furnace in air at 353 K for 12 h. A brownish solid (ID 18942) was collected and thermally treated in argon (flow rate: 50 mL/min) at 673 K for 2 h in a rotating quartz tube to receive the final catalyst (ID 19116).

2.4.1.3 Washing of nano-structured MnWO₄ with nitric acid solution

As-prepared MnWO₄ (ID 18942) was washed with 2 M solution of nitric acid at 60°C for 1 hour. The solid was separated from the washing solution by centrifugation. The washing solution was

analysed by XRF. After centrifugation, the solid was washed with de-ionized water twice and dried in a muffle furnace in air at 353 K for 12 h (ID 20640). Then, the material was thermally treated in argon (flow rate: 50 mL/min) at 673 K for 2 h in a rotating quartz tube to receive the final acid washed catalyst (ID 20655).

2.4.1.4 Reference catalysts manganese oxides and VO_x/SiO₂

MnO₂ (ID 18625) with $S_{\text{BET}}=5.1 \text{ m}^2/\text{g}$ was achieved by thermal decomposition of Mn(NO₃)₂·4H₂O in O₂/Ar at 280°C. Mn₃O₄ (ID 18856) with $S_{\text{BET}}=11.0 \text{ m}^2/\text{g}$ was synthesized by mixing Na₂B₄O₇ (0.01 mol) and Mn(II)ac₂ (0.01 mol) dissolved in 100 mL milipore water and subsequent addition of a stated amount of aqueous solution of NaOH (0.1 mol) and then vacuum drying of the mixture. Mn₂O₃ (ID 19405) with $S_{\text{BET}}=0.5 \text{ m}^2/\text{g}$ was purchased from Aldrich.

VO_x/SiO₂ (ID 18341) with $S_{\text{BET}}=377 \text{ m}^2/\text{g}$ and vanadium loading of 4.1wt.% was prepared by ion exchange, in which an aqueous NH₄VO₃ solution was added to dispersed modified-SBA-15 (ID 18026) functionalized by (3-Aminopropyl) trimethoxysilane (APTMS) in de-ionized water as described before.[83] The catalyst was calcined in a rotating furnace (Xerion Advanced Heating GmbH) at 550°C for 8 h under O₂/Ar (20/80) (500ml/min). For preparation of modified SBA-15, 44.8g of Pluronic P-123 (poly(ethylene glycol)-poly(propylene glycol)- poly(ethylene glycol)) was dissolved in 1.6L of HCl (1.6M), stirred and heated at 35°C in an automated laboratory reactor (LabMax, Mettler-Toledo). After complete dissolution, 85.1g of TEOS were added. After 12h stirring at 35°C, another 45g of TEOS were added. After stirring, the solution was heated in autoclaves at 110°C for 24h. Then, the solid was filtered and washed until the filtrate was neutral. The solid was dried in a furnace at 80°C overnight (ID 18009) and then calcined in two batches at 550°C for 8h under O₂/Ar (20/80) (500ml/min) to obtain the final modified SBA-15 support (ID 18026).

2.4.2 Catalyst characterization

2.4.2.1 Electron microscopy

Transmission electron microscopy (TEM) studies were conducted on a Philips CM200 FEG transmission electron microscope operating at 200 kV. High resolution TEM (HRTEM) and high resolution high angle annular dark field scanning transmission electron microscopy (HAADF-STEM) were performed on a Cs corrected FEI TITAN 80-300 operated at 300 kV and a double corrected JEOL JEM-ARM200F equipped with CEOS CESCOR, and CEOS CETCOR hexapole aberration correctors for probe and image forming lenses, respectively, and a cold field emission gun (CFEG). The acceleration voltage was set to 200 kV. TEM samples were prepared by drop deposition from ethanolic suspensions onto lacey-carbon coated Cu grids. Field emission scanning electron microscopy (FESEM) was carried out with a Hitachi S4800 instrument operating at 5 kV.

2.4.2.2 X-ray diffraction (XRD) and Rietveld refinement analysis

The X-ray diffraction (XRD) measurement was performed in Bragg-Brentano geometry on a Bruker AXS D8 Advance theta/theta diffractometer, using Ni filtered Cu K α radiation and a position sensitive LynxEye silicon strip detector. The sample powder was filled into the recess of a cup-shaped sample holder, the surface of the powder bed being flush with the sample holder edge (front loading).

XRD data were evaluated by whole powder pattern fitting according to the Rietveld method as implemented in the TOPAS software [version 4.2, copyright 1999-2009 Bruker AXS]. During the routine fitting, which uses an isotropic peak width model (i.e. the diffraction profile widths are described as a smooth function of the diffraction angle, independent of hkl), systematic peak profile mismatches of varying degree were observed. With the anisotropic crystallite shape observed by electron microscopy in mind, we developed an appropriate anisotropic (i.e. hkl dependent) peak width model. A model, which worked well, was obtained by modifying the phenomenological model published by Stephens.[84] Due to the macro language implemented in TOPAS, user defined peak models can be implemented easily. The original Stephens model, which was derived to describe anisotropic strain broadening, did not work well with our data. Since we expected anisotropic crystallite size to be the predominant peak broadening factor in our case, we replaced the angular dependent term $\tan(\theta)$ (representing strain) of the original Stephens model with a $\cos(\theta)-1$ (i.e. size) term, while retaining the hkl dependent expression. In addition to a good overall fit, this modified model allowed us to obtain the nominal crystallite size for different crystal directions. The largest dimension was consistently calculated for the 00l direction. Nominal crystallite sizes are reported here for the principal crystal directions h00, 0k0 and 00l (Table S1). It should be noted that such values represent volume weighted average lengths of unit cell columns, LVol-IB. This includes averaging over parallel columns of different lengths within crystallites (shape dependent), as well as averaging over different crystallites of possibly different size (size distribution dependent). Thus, the reported LVol-IB values cannot be directly compared to physical dimensions of discrete crystallites as e.g. observed by electron microscopy. Nevertheless, the XRD derived dimensions may be considered to represent a (volume weighted) average crystallite morphology. To simplify a comparison with the results of other methods, “aspect ratio” D_a/D_b , and D_c/D_b , respectively, were calculated from the principal dimensions in Table S1.

2.4.2.3 Raman spectroscopy

Confocal Raman spectroscopy was performed using a Horiba Jobin LABRAM instrument equipped with a microscope (Olympus). A He-Ne laser (wavelength 632.8 nm, 1.5 mW at the sample position) was used for the excitation. A pressed wafer of the sample was mounted on the sample holder for recording spectrum.

In situ Raman during hydrothermal synthesis was carried out using a Raman probe (RXN1, immersion optics 1/4"OD (HC276); Kaiser Optical Systems). The Raman spectra were automatically recorded every 2 min at a wavelength of 785 nm with an exposure time of 30 s.

2.4.2.4 X-ray fluorescence (XRF)

XRF was performed using a Bruker S4 Pioneer X-ray spectrometer. For sample conditioning, beaker of 25 mm diameter with 6 μ MYLAR foil was used to contain 5 ml of sample solution without any pretreatment. Samples were measured under He atmosphere. The solvent (water) was assumed as matrix and iteratively calculated to sum up the total to 100 %.

2.4.2.5 X-ray photoelectron spectroscopy (XPS) and Near edge X-ray absorption fine structure (NEXAFS)

XPS and NEXAFS analyses were conducted at the near ambient pressure XPS end station of the ISSS beamline at HZB/BESSY II (Berlin, Germany). Details of the setup have been published earlier. [85] For the XPS measurements, the kinetic energy of the photoelectrons was varied between 150 eV and 750 eV separately for each core level, hence escape depths (63% of the detected signal stems from this depth) of ca. 0.6 nm (150 eV, denominated as surface) and ca. 1.6 nm (750 eV, denominated as subsurface) were probed. The experiments have been performed at a total pressure of 0.25 mbar in O₂/He or C₃H₈/O₂/He mixtures with a total gas flow of 4.2 sccm at temperatures between 300 °C and 400 °C. The error bar of the absolute elemental composition can be estimated to be 30% due to uncertainties in the monochromatic photon flux, cross sections and peak area determination. However, only the uncertainty in the peak area determination contributes to relative uncertainties in an experimental series (different conditions with the same catalysts or different catalysts under the same condition), and therefore the relative error bar in the XPS figures can be estimated to be approximately 5%. Might be that the roughness of the surface changes as a function of the catalytic conditions (oxidative or reductive). In this case the depth profile will change and therefore the error bar increases.

NEXAFS spectra were recorded simultaneously in total electron yield (TEY) and Auger electron yield (AEY) mode. Due to the low inelastic mean free path of electrons in solids, electron yield X-Ray absorption spectroscopy (XAS) is more surface sensitive than fluorescence based techniques. The highest surface sensitivity of XAS is given in the AEY mode in which Auger electrons on an selected energy interval are analyzed by the spectrometer.[86] In the case of the recorded Mn L_{2,3}- edge, electrons with a kinetic energy around 50 eV were analyzed.

2.4.2.6 Nitrogen adsorption

The surface area determination was carried out in a volumetric N₂ physisorption set-up (Autosorb-6-B, Quantachrome) at the temperature of liquid nitrogen. The sample was degassed in dynamic vacuum at a temperature of 573 K for 2 h prior to adsorption. The relative N₂ pressure was varied ($p/p_0=0.05$ –

0.3), and 11 data points were measured. The linear range of the adsorption isotherm was considered to calculate the specific surface area according to the BET method.

2.4.2.7 Temperature-programmed oxidation and reduction (TPO-TPR)

TPO was performed in a fixed-bed quartz reactor using 300 mg of the sample. Prior to the first TPO measurement, the sample was pretreated at 400 °C for 2h in Ar (flow rate 50 ml/min, heating rate of 5 °C/min). The TPO measurement was performed up to 400°C in a mixture 0.24% O₂/He (flow rate 100 ml/min), applying a heating rate of 5°C/min and a holding time of 60 min. O₂ consumption was monitored with a paramagnetic detector. After the TPO run, TPR was performed up to 400°C in 0.25% H₂/Ar (flow rate 100 ml/min), applying the same heating rate and holding time. H₂ consumption was monitored with a thermal conductivity detector (TCD). The TCD detector was calibrated by reducing a known amount of CuO. Then the second TPO measurement was done followed by the second TPR run applying the same procedures as in the first runs.

2.4.2.8 Catalytic testing of oxidative dehydrogenation of propane (ODP)

The catalytic tests were carried out using a setup for partial oxidation (Integrated Lab Solutions) with 8 fixed bed quartz reactors (6 mm inner diameter) in parallel. Each reactor was equipped with a thermocouple for measuring the temperature inside the catalyst bed containing 300 mg of catalyst previously sieved to a particle size of 250-355 µm and the catalytic performances were determined at atmospheric pressure. The reactant feed comprised the C₃H₈, O₂, and N₂ as diluent passed each reactor at a flow rate of 10 mL/min. The composition of the feed was 10 % C₃H₈, 5 % O₂ and 85% N₂.

The product (and bypass) gas mixtures were analyzed by an online gas chromatograph (Agilent 7890). A system of Plot-Q and Plot-molsieve columns connected to a thermal conductivity detector (TCD) separated the permanent gases CO, CO₂, N₂, O₂, and CH₄. A system of a FFAP and a Plot-Q column connected to a flame ionization detector (FID) allowed the separation of C₂-C₃ hydrocarbons and oxygenates.

2.5 Supporting information

2.5.1 Supporting tables

Table S 2.1 Average crystallite sizes *D* of the particles in the MnWO₄ catalyst (ID 19116) along the *a*, *b*, and *c* axis calculated from anisotropic fitting in Rietveld refinement based on the XRD patterns presented in Figure S2.2.

<i>D_a</i> /nm	<i>D_b</i> /nm	<i>D_c</i> /nm	Ratio <i>D_a</i> / <i>D_b</i>	Ratio <i>D_c</i> / <i>D_b</i>
24.0	17.3	55.4	1.4	3.2

Table S 2.2 Intensity ratio of the peaks at 640 and 641.4 eV in the NEXAFS of nano-structured MnWO₄ at the Mn L_{2,3}-edge. The spectra in Total Energy Yield (TEY) are presented in Figure S2.14.

Treatment	Mode ¹	I ₆₄₀	I _{641.5}	Peak ratio ²
O ₂ /He, n min	TEY	7.67	3.50	2.2
O ₂ /He, n min	AEY	7.48	4.45	1.7
O ₂ /He, n min		6.59	3.84	1.7
O ₂ /He, n min		6.15	3.54	1.7
O ₂ /He/C3, n min	TEY	8.11	3.59	2.3
O ₂ /He/C3, n min	AEY	6.97	3.59	1.9
O ₂ /He/C3, n min		7.14	3.33	2.1
O ₂ /He/C3, n min		7.32	3.25	2.2

¹ mode of measurement

² peak ratio 640/641.5

Table S 2.3 Hydrogen consumption during TPR and oxygen consumption during TPO experiments with nano-structured MnWO₄.

	TPO-1	TPR-1	TPO-2	TPR-2
O ₂ or H ₂ consumption /mmol mol ⁻¹	22.1	17.7	7.13	16.6
O ₂ or H ₂ consumption /10 ⁻⁶ mol m ⁻²	2.54	2.03	0.82	1.91
Number of oxygen atoms replenished or reduced ¹ /nm ⁻²	3.06	1.22	0.99	1.15
Percentage of surface oxygen atoms replenished or reduced ² /%	15.3	6.1	5.0	5.8
¹ Assuming that oxidation and reduction only occur at the surface;				
² Assuming a surface oxygen atom density of 20/nm ²				

Table S 2.4 Chemical composition of the washing solution after treatment of nano-structured MnWO₄ with nitric acid as determined by XRF.

	MnO	Na ₂ O	WO ₃	H ₂ O
Concentration /wt %	0.39	0.00	0.00	99.6

Table S5. Surface area and lattice parameters of the nano-structured MnWO₄ materials.

	S _{BET} /m ² g ⁻¹	unit cell parameters			
		<i>a</i> / Å	<i>b</i> / Å	<i>c</i> / Å	<i>β</i> / °
As-synthesized MnWO ₄ nano-rods (ID 18942)	31.0	4.824(1)	5.761(2)	4.998(7)	91.18(2)
Calcined MnWO ₄ nano-rods (ID 19116)	28.7	4.828(7)	5.762(5)	5.000(7)	91.18(9)
Nitric acid washed and re- calcined MnWO ₄ (ID 20655)*	29.5	4.828(5)	5.758(8)	4.997(7)	91.18(3)

* The catalyst contains small amounts of an unknown phase.

2.5.2 Supporting figures

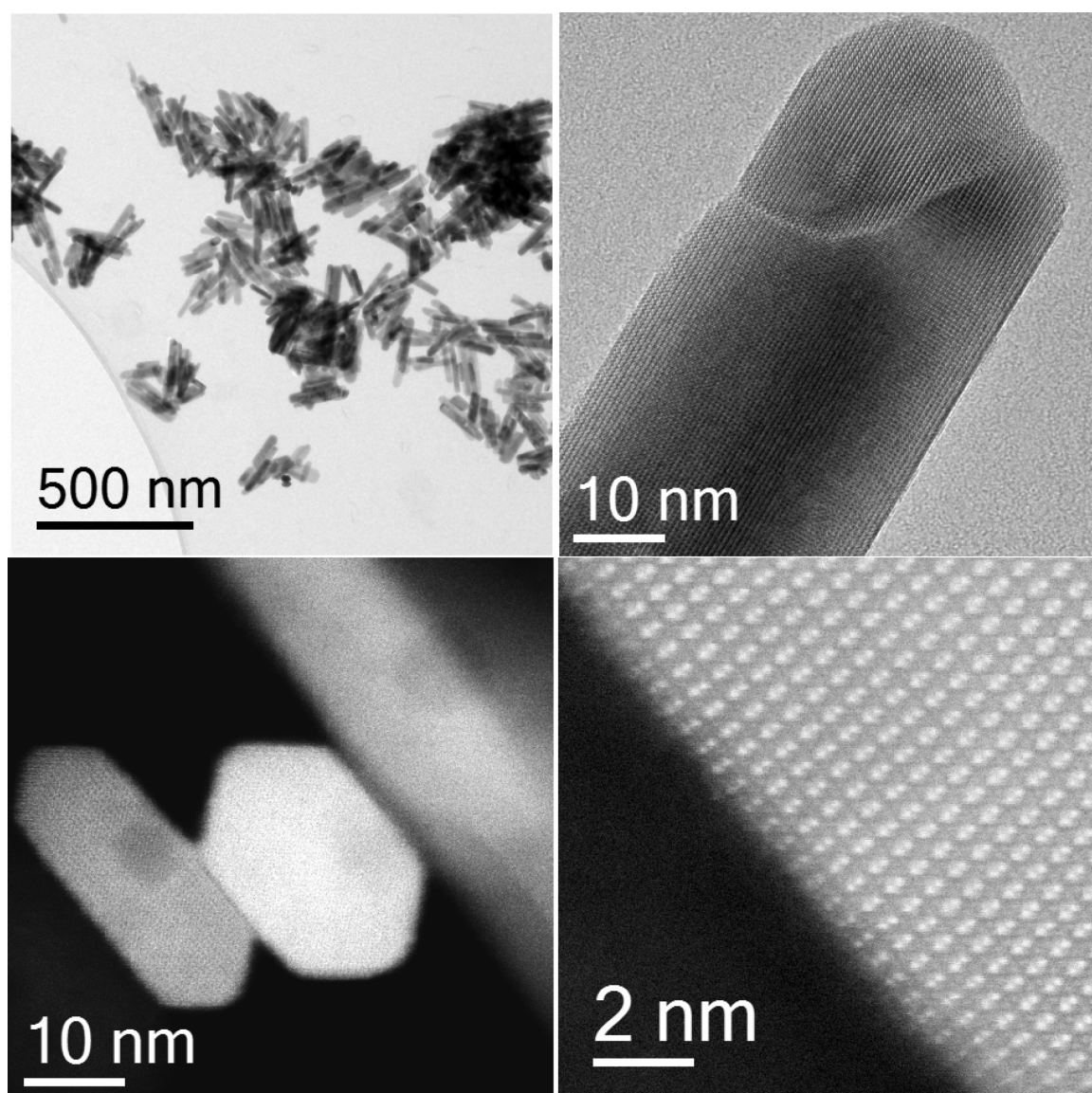


Figure S 2.1 Original images presented in Figure 2.1.

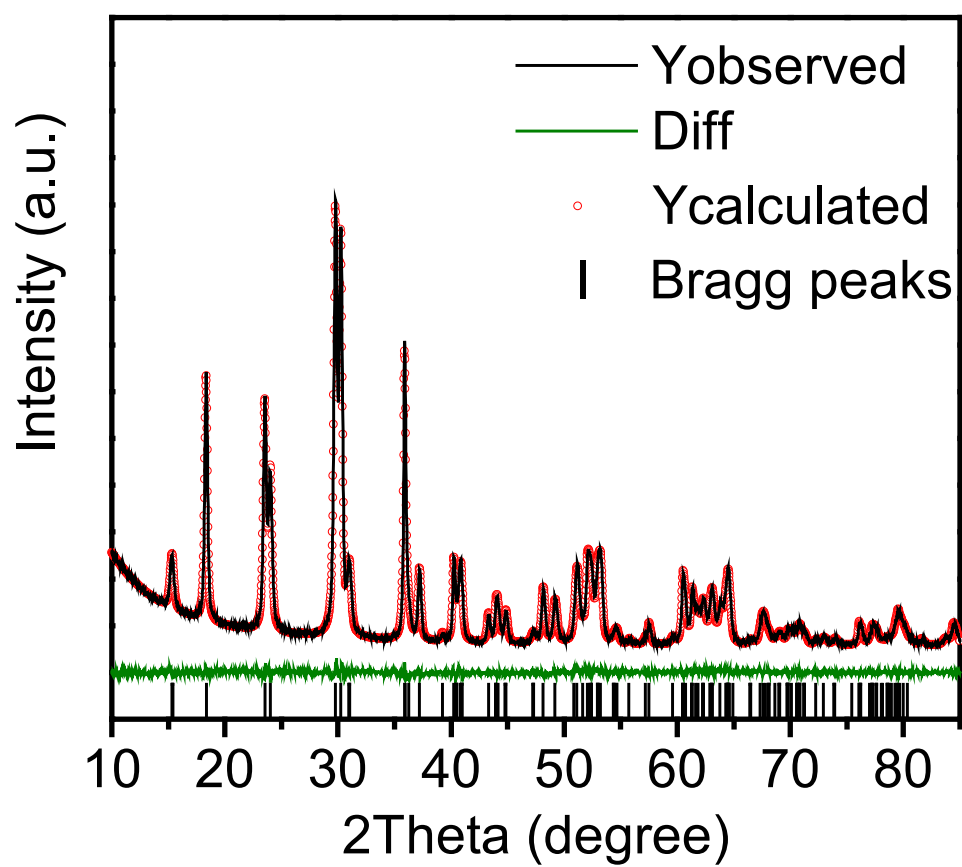


Figure S 2.2 Rietveld refinement of the powder XRD of the MnWO₄ catalyst (ID 19116).

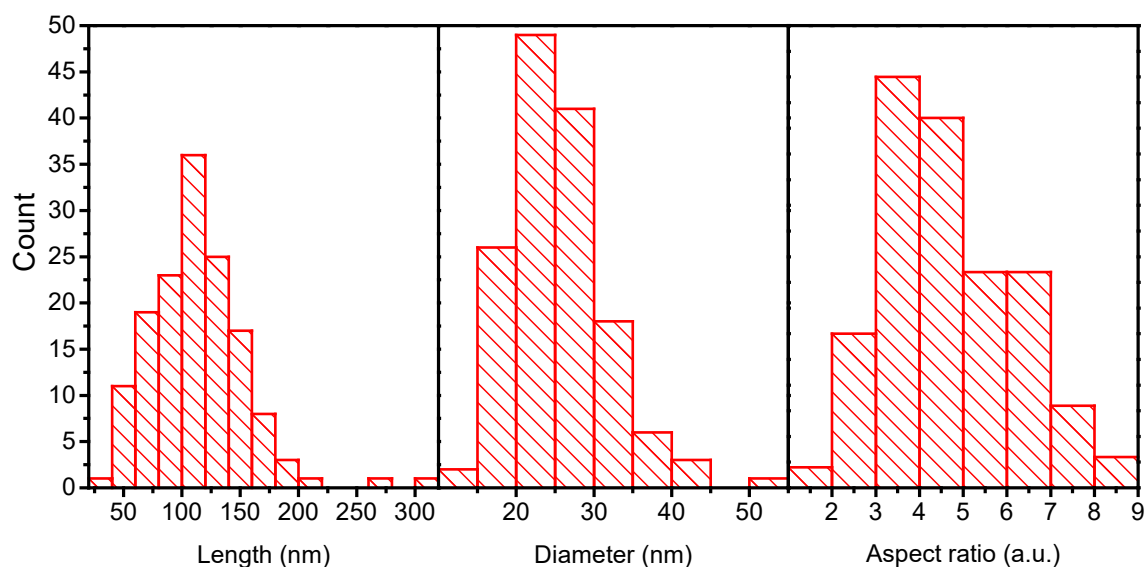


Figure S 2.3 Particle size distribution in the thermally treated nano-structured MnWO₄ catalyst (ID 19116) based on the analysis of approximately 146 particles in TEM images (see for example Figure 2.1a in the main manuscript).

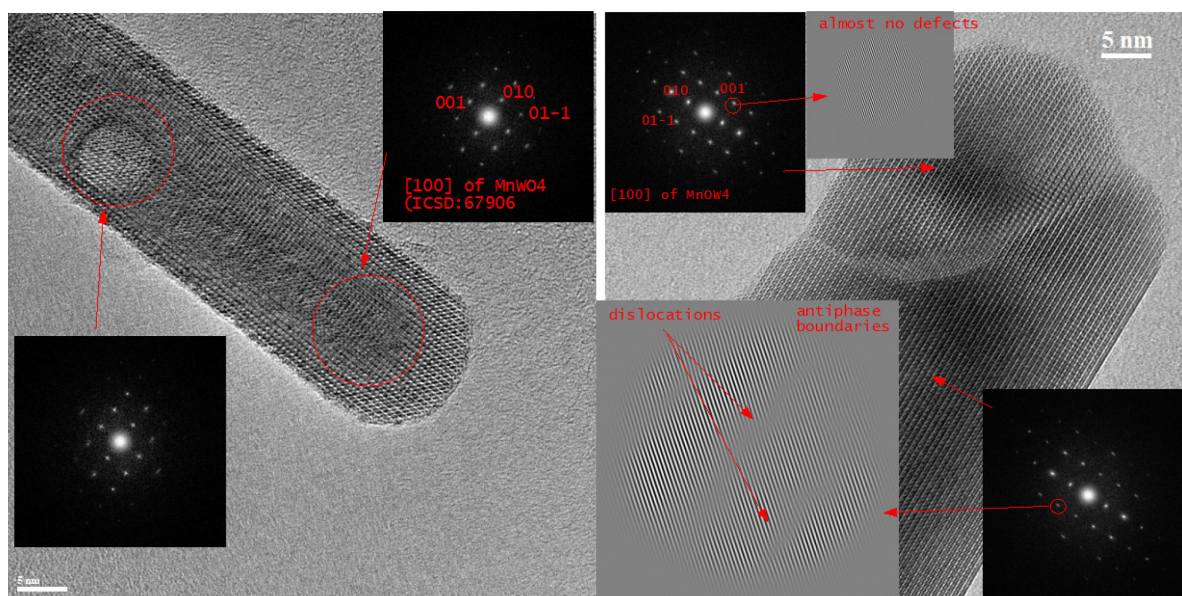


Figure S 2.4 HRTEM images and fast Fourier transform (FFT) analysis of two MnWO₄ nanorods in the catalyst (ID 19116).

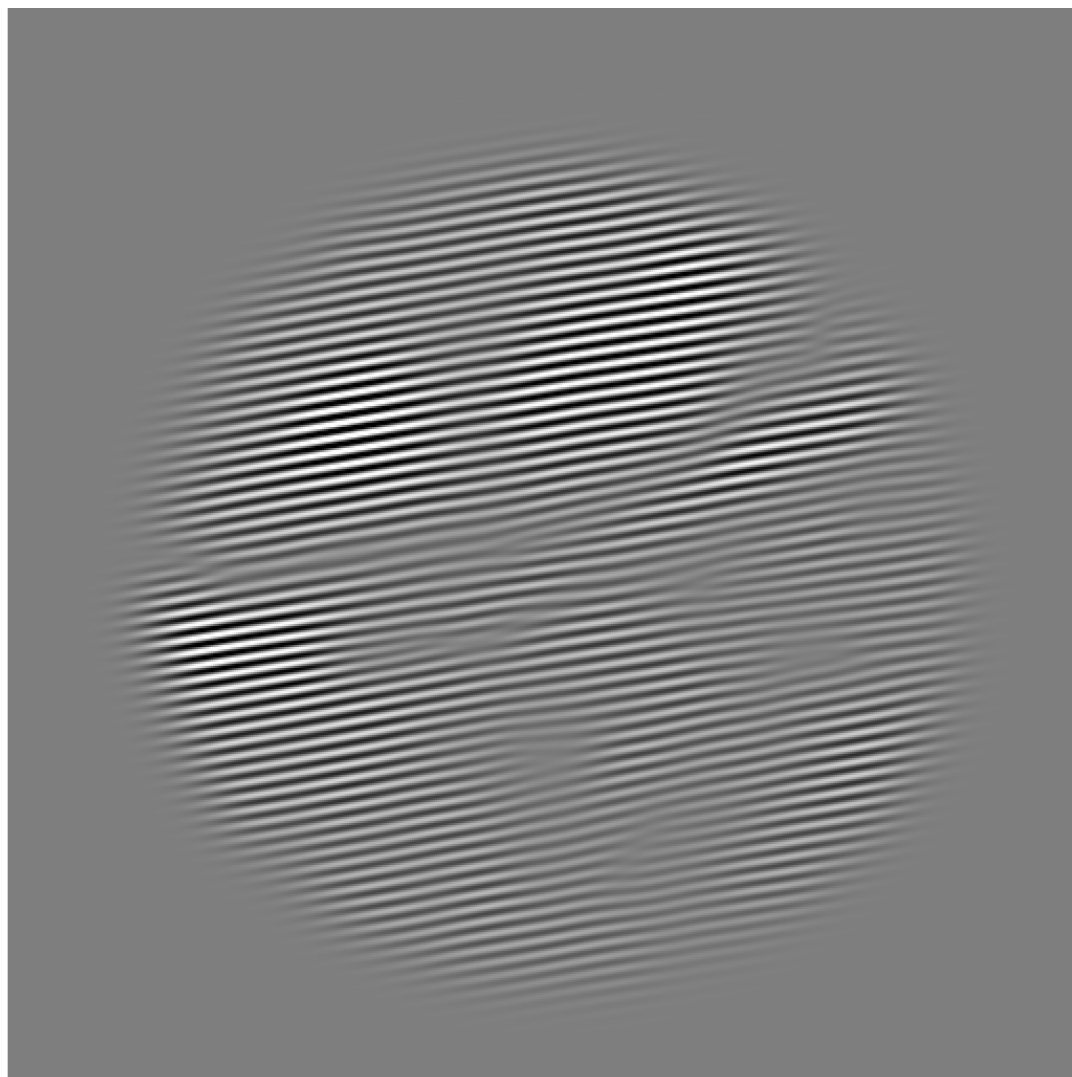


Figure S 2.5 Inverse Fast Fourier transformation (IFFT) of the 110 spots in Figure 2.1b.

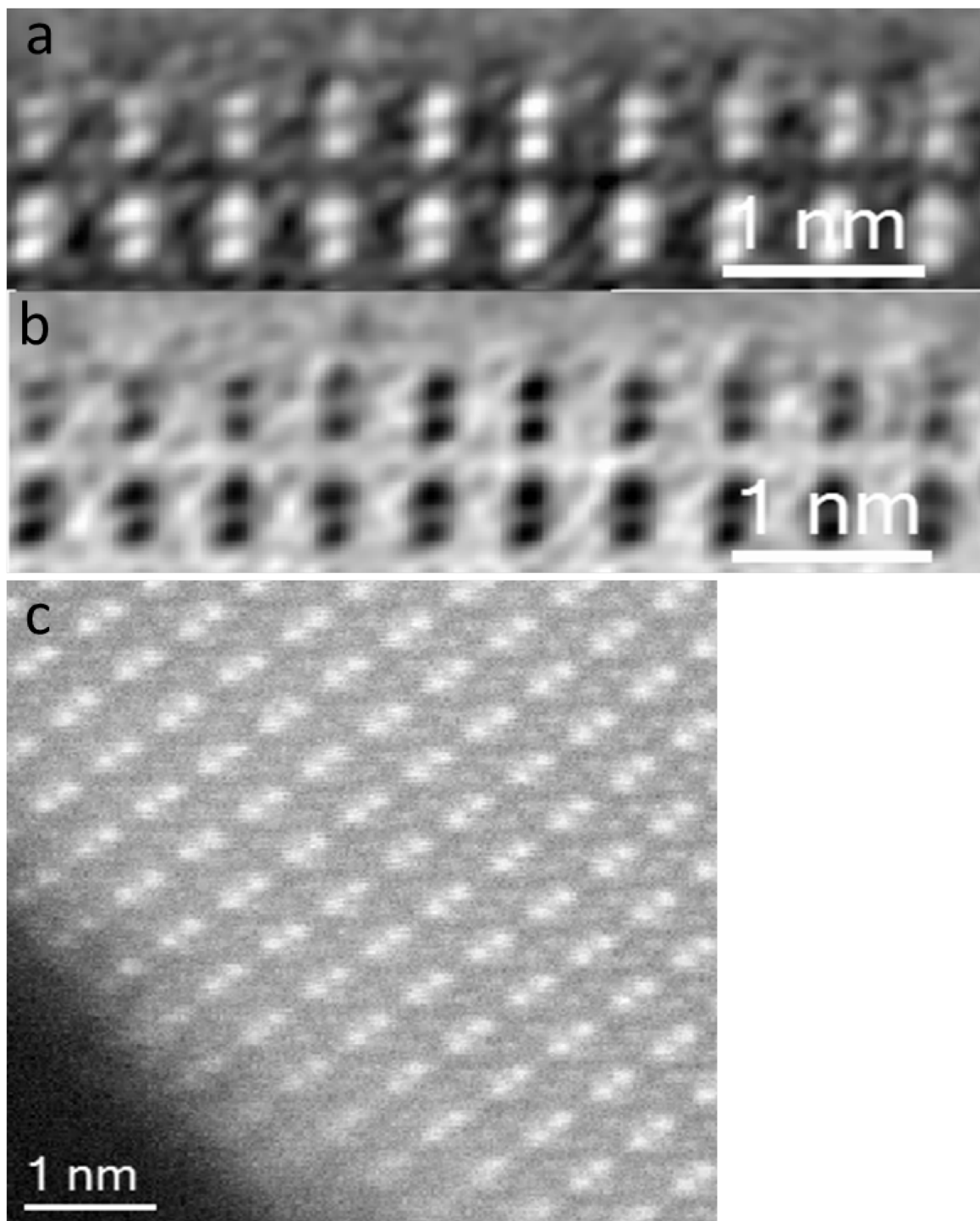


Figure S 2.6 FFT filtered HR-STEM images of MnWO₄ (ID 19116) a) HAADF, b) inverted HAADF and c) HR-HAADF-STEM images.

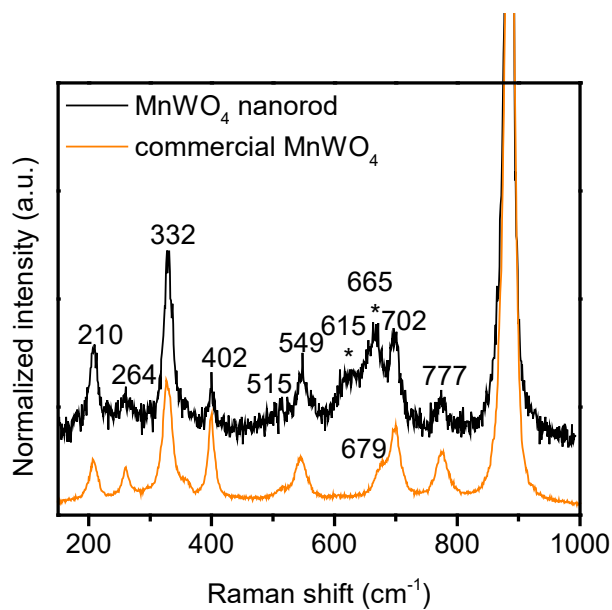


Figure S 2.7 Raman spectrum of the MnWO₄ catalyst (ID 19116) (black line) compared to the Raman spectrum of commercial MnWO₄ (orange line).

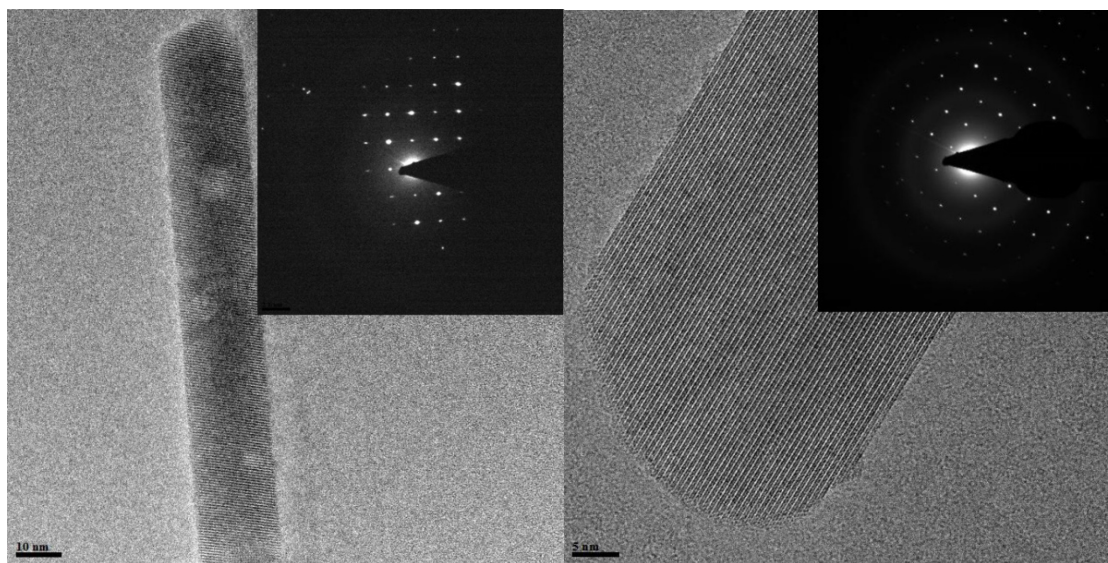


Figure S 2.8 HRTEM images and electron diffraction patterns of MnWO₄ nano-rods.

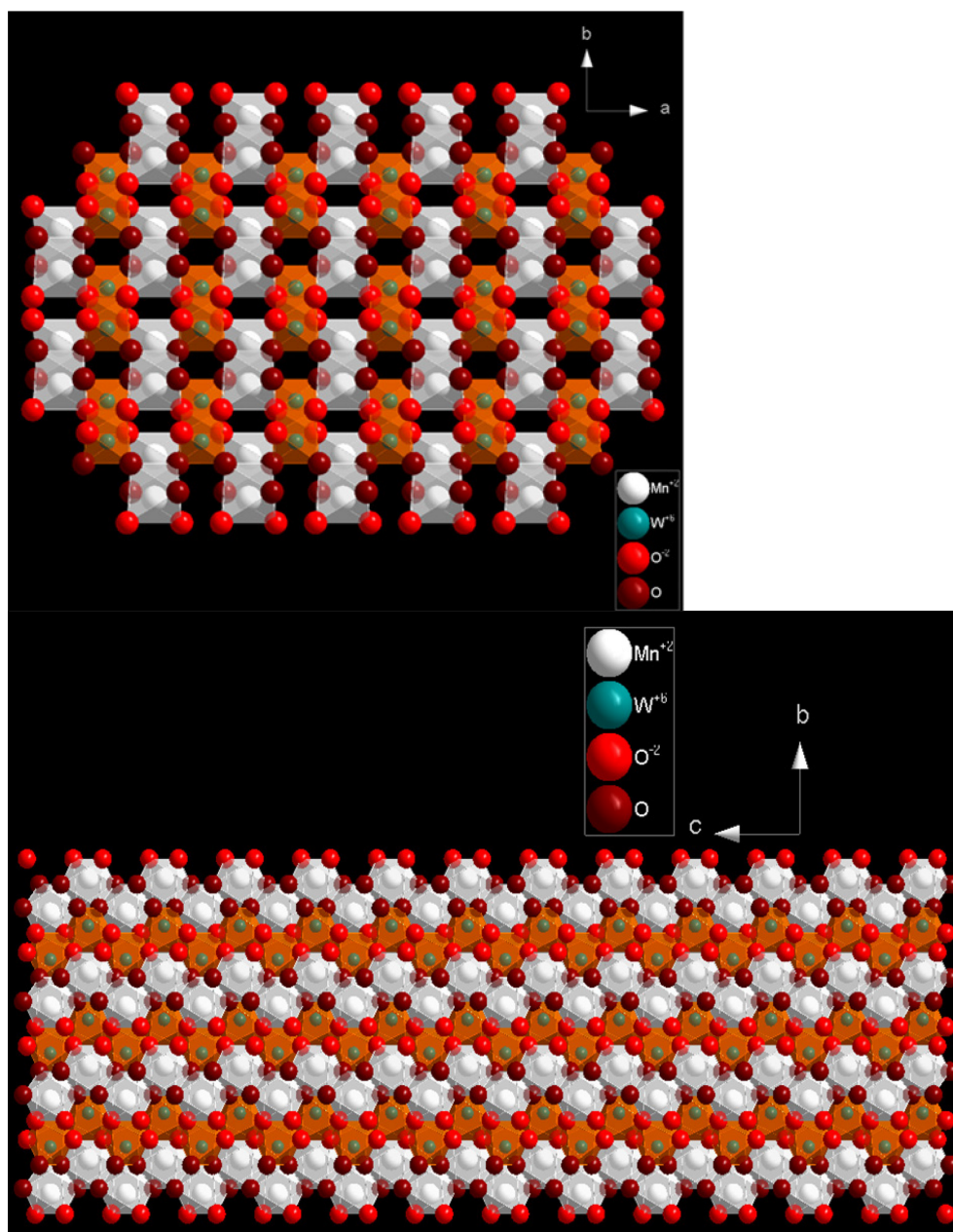


Figure S 2.9 Schematic representation of the crystal structure of MnWO₄ viewed along a) the [001] axis and b) the [100] axis. White ball represents Mn²⁺, green ball represents W⁶⁺, red ball represents O²⁻ (bridging oxygen) and wine ball represents terminal oxygen atoms (tungsten oxygen double bond).

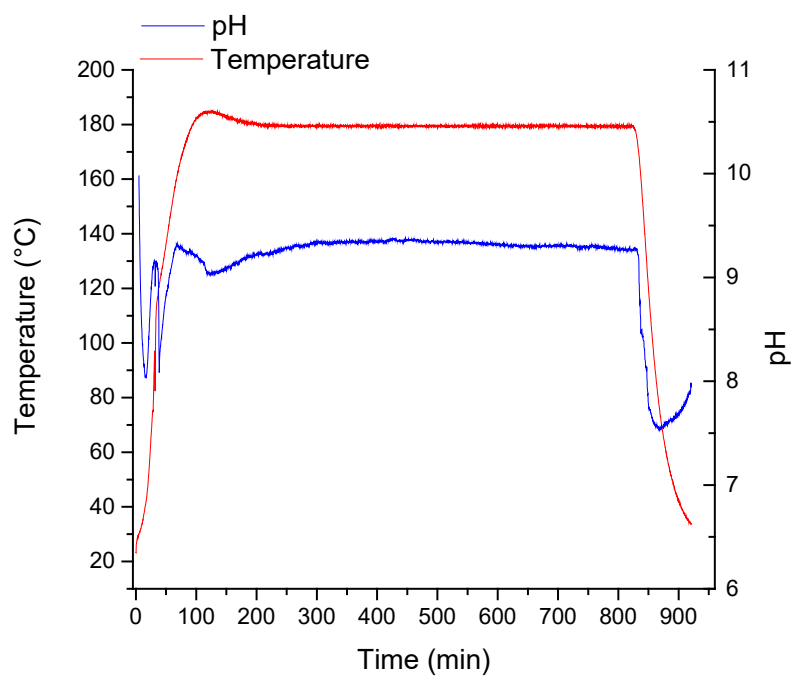


Figure S 2.10 Recorded workflow during hydrothermal synthesis of nano-structured MnWO₄; blue line: pH value measured in the autoclave, red line: temperature of the synthesis gel.

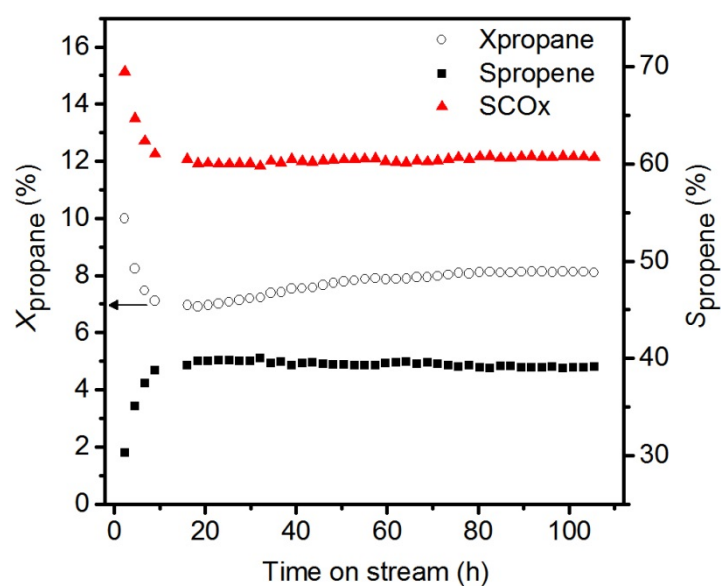


Figure S 2.11 Time on stream plot of propane conversion and selectivity to propene in the oxidative dehydrogenation of propane at T=400°C, and W/F=1.8 g s/ml over nano-structured MnWO₄ (catalyst ID 19116); The feed was composed of C₃H₈:O₂:N₂=10:5:85; The changes in the conversion (X) of propane and the selectivity (S) to propylene and carbon oxides (CO_x: CO + CO₂) are shown with time on stream.

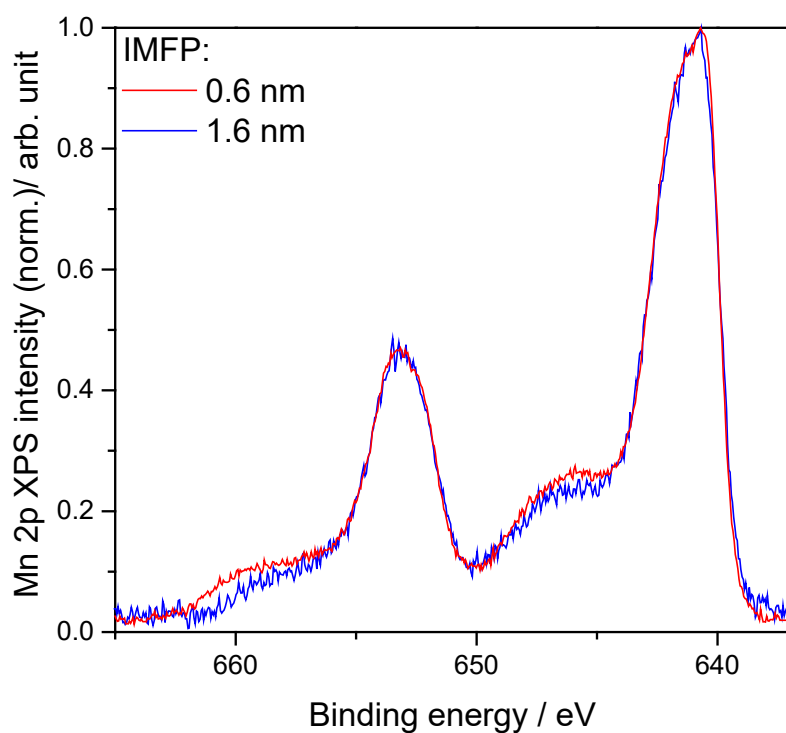
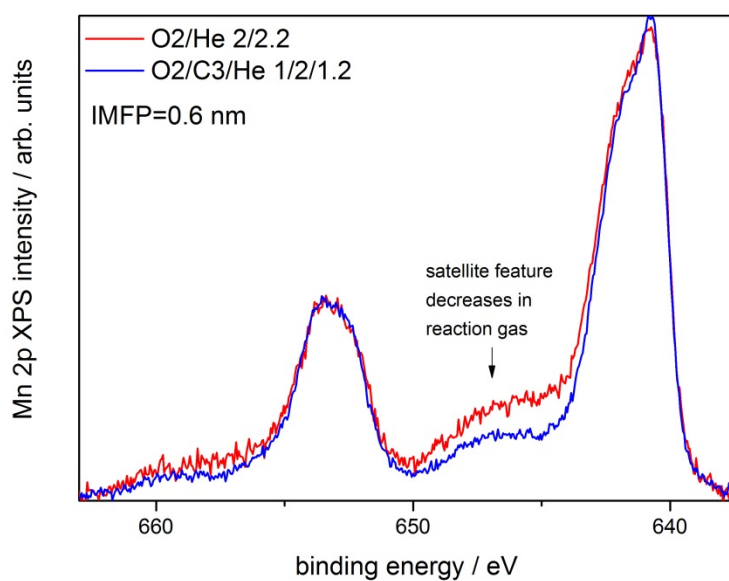


Figure S 2.12 Mn 2p spectra of nano-structured MnWO₄ within different detection depths represented by the inelastic mean free path (IMFP) of electrons measured by synchrotron-based NAP-XPS at T=300 °C applying a total pressure of 0.25 mbar O₂ and He flows of 2 and 2.2 sccm, respectively.



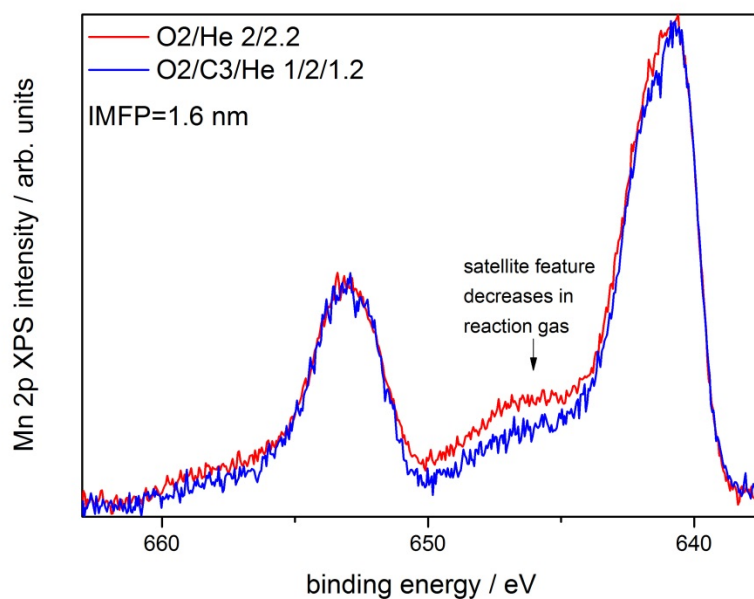


Figure S 2.13 Mn 2p spectra of nano-structured MnWO₄ within different detection depths represented by the inelastic mean free path (IMFP) of electrons measured by synchrotron-based NAP-XPS at T=300 °C applying a total pressure of 0.25 mbar under different reaction atmospheres; Red lines: O₂ and He flows of 2 and 2.2 sccm, respectively; Blue lines: O₂, C₃H₈, and He flows of 1, 2, and 1.2 sccm, respectively.

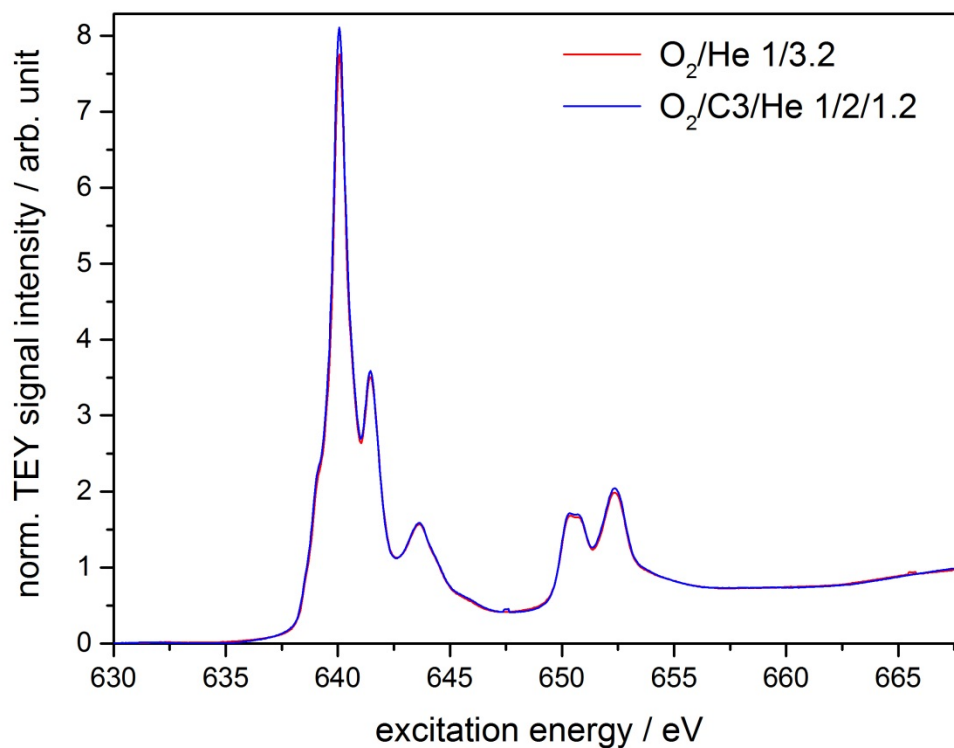


Figure S 2.14 NEXAFS of nano-structured MnWO₄ measured at the Mn L_{2,3}-edge in total electron yield (TEY) in different reaction atmospheres at T=380°C; Red lines: O₂ and He flows of 1 and 3.2 sccm, respectively; Blue lines: O₂, C₃H₈, and He flows of 1, 2 and 1.2 sccm, respectively.

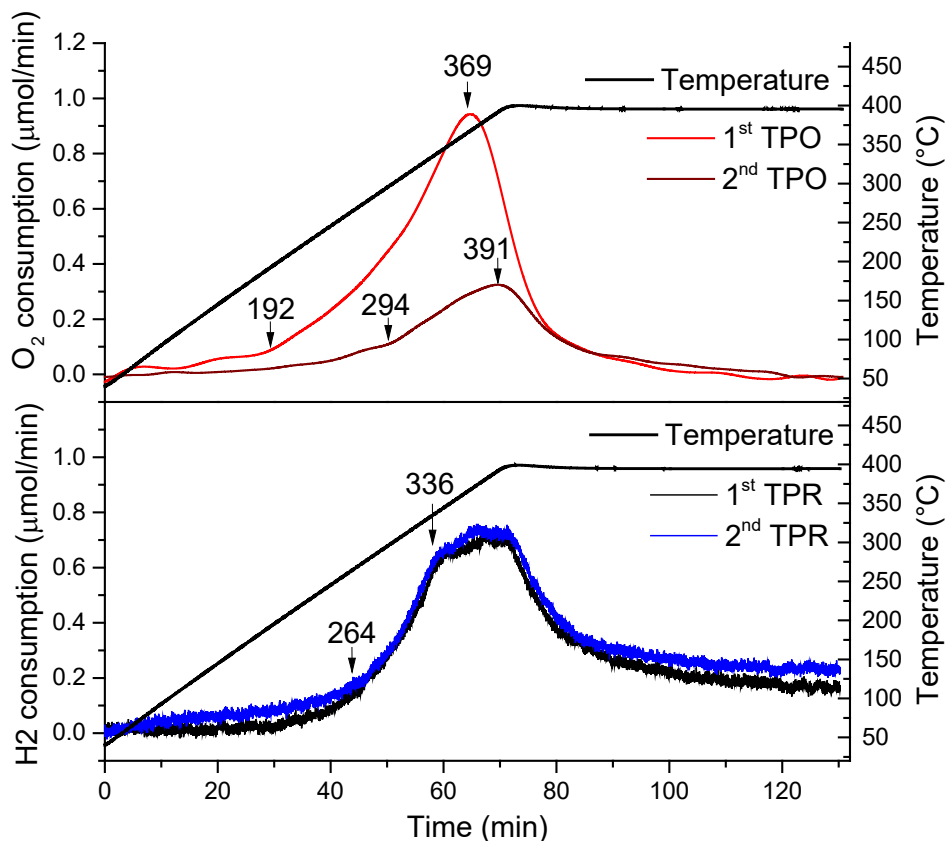


Figure S 2.15 Temperature-programmed oxidation (TPO) (top), and temperature-programmed reduction (TPR) (bottom) profiles of nano-structured MnWO_4 .

2.6 Acknowledgements

This work was conducted in the framework of the BasCat collaboration between BASF SE, TU Berlin, FHI, and the cluster of excellence “Unified Concepts in Catalysis”. X.L. acknowledges the Berlin International Graduate School of Natural Sciences and Engineering (BIG NSE) as part of UniCat for financial support. The authors thank Maike Hashagen, Jasmin Allan, Achim Klein-Hoffmann, Dr. Olaf Timpe, and Caroline Dessal for technical assistance. We thank the HZB staff for their continual support of the electron spectroscopy activities of the FHI at BESSY II.

3 Hydrothermal synthesis of bi-functional nanostructured manganese tungstate catalysts for selective oxidation¹

Abstract: The mechanism of C-H activation in selective oxidation reactions of short-chain alkane molecules over transition metal oxides is affected by the balance of acid-base and redox sites on the surface of the catalyst. Using the example of manganese tungstate we discuss how the relative abundance of these sites can be controlled via synthetic techniques. Phase-pure catalysts composed of the thermodynamic stable monoclinic MnWO_4 phase have been prepared by hydrothermal synthesis. Variation of the initial pH value resulted in rod-shaped nano-crystalline MnWO_4 catalysts composed of particles with varying aspect ratio. The synthesis products have been analysed by transmission electron microscopy, X-ray diffraction, infrared, and photoelectron spectroscopy. In-situ Raman spectroscopy was used to investigate the dissolution-re-crystallization processes occurring under hydrothermal conditions. Ethanol oxidation reaction was applied to probe the surface functionalities in terms of acid-base and redox properties. Changes of the aspect ratio of the catalyst particles are reflected in the product distribution induced by the different fraction of acid-base and redox sites exposed at the surface of the catalysts in agreement with the proposed mechanism of particle growth by re-crystallization during ageing under hydrothermal conditions.

3.1 Introduction:

Metal oxides are widely used as heterogeneous catalysts in the synthesis of chemicals, and in energy conversion and storage applications.[22, 87-89] High performance, selectivity, and stability of oxides in heterogeneous catalysis are bound to homogeneity of the solid.[90] In complex reactions, such as selective oxidation of hydrocarbons, multi-functionality is necessarily required and can be achieved either chemically or by nano-structuring.[58, 91] Solvothermal techniques have been efficiently used in the preparation of metastable phases or oxides with particular morphological properties.[92-97] However, the underlying preparation strategies are often based on experience and parameter variation. Targeted design of metal oxide catalysts with predictable functionalities needs deeper understanding of the chemistry in precursor solutions and during nucleation, growth, and ageing.

¹ The following chapter is the submitted version of [116], the peer reviewed published version can be found with publisher DOI link: <http://dx.doi.org/10.1039/C5FD00191A>

In-situ Raman spectroscopy has been proven beneficial in the investigation of condensation reactions of transition metal oxide species occurring at elevated temperature and pressure inside an autoclave.[98, 99] Our recent study concerning the speciation of molybdates in aqueous media revealed that the molecular structure of the oxo-anions in the temperature range between 100 and 200°C differs significantly from room temperature at comparable concentration and pH values.[99] Implicit understanding of the known condensation chemistry of molybdates under ambient conditions is, therefore, not beneficial in terms of knowledge-based planning the hydrothermal synthesis of molybdenum oxide-based catalysts. Likewise, systematic in-situ spectroscopic studies of the synthesis of complex metastable mixed oxide phases, like the so-called M1 phase of MoVTeNb oxide, resulted in the development of modular preparation techniques that yield the desired phase more effectively in shorter synthesis time with improved catalytic properties.[98]

Herein we present in-situ Raman spectroscopic and transmission electron microscopy studies that provide insight into the mechanism of particle growth and re-crystallization during the synthesis of the thermodynamic stable monoclinic manganese tungstate phase in wolframite-type structure (ICSD 67906).[100] Nano-structuring of manganese tungstate features a feasible strategy to control bi-functional properties of the mixed metal oxide with implications on the selectivity in oxidation reactions applied to upgrade alkanes. We demonstrate the viability of such a strategy by studying rod-shaped nano-crystalline MnWO_4 catalysts consisting of particles with varying aspect ratio (AR). The particle morphology was controlled via the concentration of OH^- ions under hydrothermal synthesis conditions. Oxidation of ethanol was chosen to probe the surface chemistry of the synthesized materials in a catalytic reaction. The substrate molecule may undergo multiple pathways depending on the nature of the active sites at the catalyst surface. Generally, the alcohol is oxidized to the aldehyde at redox active centres whereas dehydration of ethanol to ethylene or the formation of diethyl ether indicate surface sites that facilitate acid/base reactions.

3.2 Results and discussion

3.2.1 Phase formation and particle growth under hydrothermal conditions

The preparation of monoclinic manganese tungstate composed of the wolframite-type structure (ICSD 67906) was performed by hydrothermal synthesis for 12 hours at 180°C in aqueous medium. The formation of the solid within the autoclave has been monitored by in-situ Raman spectroscopy. Figure 3.1 shows the spectra taken during synthesis of a slightly acidulated synthesis gel (pH of the starting mixture 6.3, Figure 3.1a)) and a mixture in which the pH has been adjusted to 9.1 by addition of NaOH solution (Figure 3.1b). Reaction between manganese nitrate and sodium tungstate occurs immediately after mixing the precursor solutions at room temperature as it becomes evident from the Raman spectra. The Raman spectrum of the Mn precursor solution shows only the nitrate peak at 1048 cm⁻¹ and no peaks due to Mn-O stretching vibrations, since divalent manganese ions are present under these conditions as an octahedral aquo complex. In the Raman spectrum of sodium tungstate solution peaks at 931, 837, and 324 cm⁻¹ occur due to the presence of dissolved [WO₄]²⁻ ions. The peaks belong to the four Raman active fundamental vibrational modes (A_g+E_g+2F_{2g}) of an undistorted

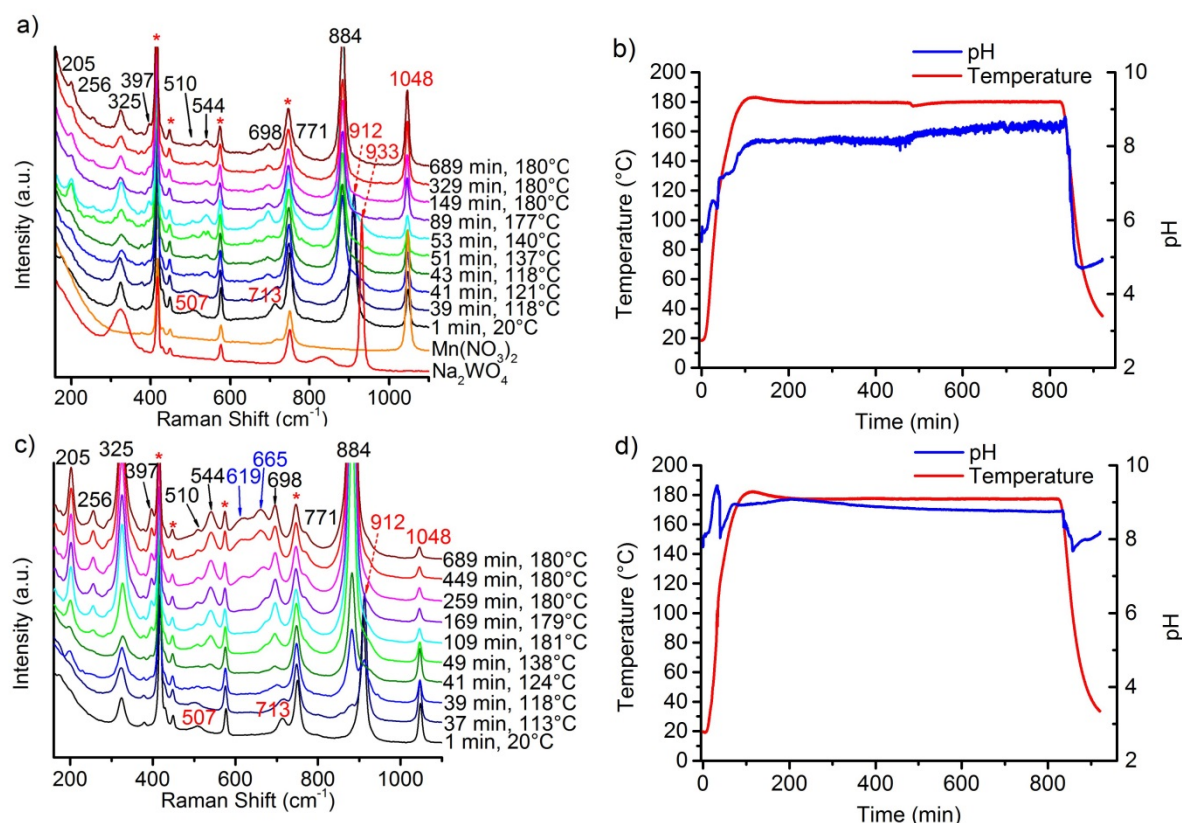


Figure 3.1 In situ Raman spectra recorded during the synthesis of the catalysts a) AR1.5 and c) AR3.9 and the corresponding profiles of temperature and pH during synthesis of b) AR1.5 and d) AR3.9; The symbol * in the Raman spectra indicates the bands of the sapphire window of the Raman probe.

tetrahedron (T_d symmetry). [101]

By mixing the two precursor solutions, the peak at 837 cm⁻¹ disappears immediately, peaks at 507 and 713 cm⁻¹ emerge, and the peak at 931 cm⁻¹ is shifted to 912 cm⁻¹ suggesting reaction between

manganese nitrate and sodium tungstate solution at room temperature. The bands are attributed to the formation of a partially crystalline product of unknown crystal structure that exhibits a layered-like morphology (Fig. S3.1), indicated also by a peak in the XRD patterns at small angles that suggests regular stacking with a d spacing of 0.8 nm. The intermediate contains Mn and W in a molar ratio close to 1. During heating, bands at 205, 256, 325, 397, 510, 544, 698, and 884 cm^{-1} indicate phase formation of MnWO_4 above 100°C that is completed at 120°C.[102, 103] It has to be noted at this point that the Raman spectra measured by using the immersion probe originate from contributions of dispersed nanoparticles as well as from molecular species dissolved in the mother liquor. The phase formation is additionally indicated by a sharp drop of the pH in the temperature range from 110-120°C. The pH at 180°C rises above 8 during the synthesis of all catalysts. The average value increases with increasing starting pH and amounts to 8.1 in the synthesis of the catalysts AR1.5 and AR1.7, to 9.0 in the synthesis of the catalysts AR3.2 and AR3.9, and to 9.3 in the synthesis of catalyst AR5.1. The regulation of the initial pH involves changes in the ionic strength of the mother liquor from 1.20 mol/L for catalyst AR1.5 to 1.22 mol/L for catalyst AR5.1. The interpretation of the evolution of the pH values during hydrothermal synthesis is not straightforward, since the measured value results from superimposing condensation and hydrolysis reactions. All peaks observed at 180°C except weak bands at 619 and 665 cm^{-1} belong to the normal modes of crystalline MnWO_4 . [102, 103] The extra peaks are tentatively attributed to manganese hydroxide species as will be discussed below. Irrespective of the initial pH value, crystallization occurs at 120°C (Fig. 3.1) implying that the crystallization process is determined by thermodynamics, since the monoclinic wolframite-type $P2_1/c$ structure is the thermodynamic stable phase under the applied synthesis conditions.[100] According to XRD, all synthesis products are phase-pure materials (Fig. S3.2). Thermal treatment in inert gas at 400°C does not change the phase composition of the products (Fig. S3.3).

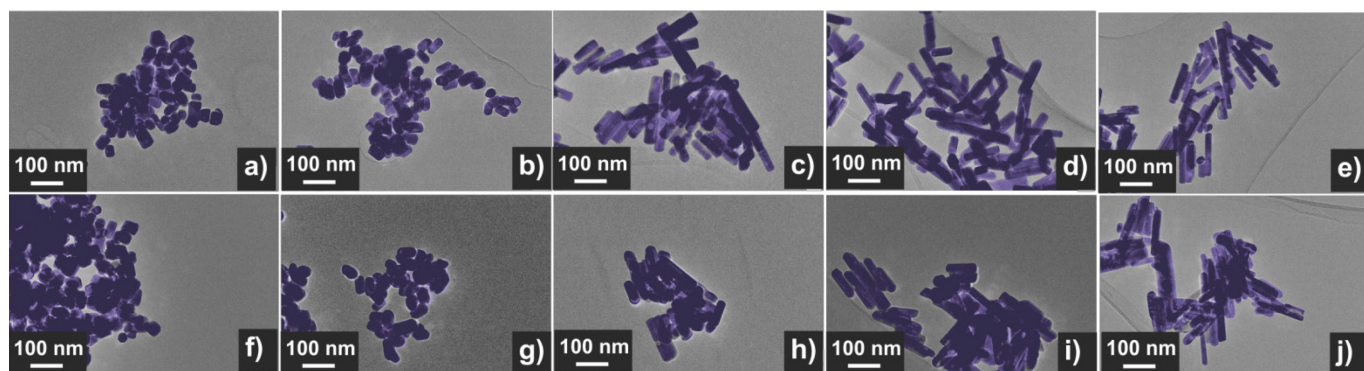


Figure 3.2 Electron microscopy images of the as-synthesized (top row) and thermally treated (bottom row) nanostructured MnWO_4 materials AR1.5 (a) and f)), AR1.7 (b) and g)), AR3.2 (c) and h)), AR3.9 (d) and i)), and AR5.1 (e) and j)); Uncoloured TEM images are presented in the Supporting Information (Fig. S3.4).

The morphology of nano-sized MnWO_4 can be tuned kinetically by adjusting the chemical potential during synthesis within the autoclave. The structural alterations are induced by different dissolution-recrystallization rates of the involved manganese tungstate species. These rates are predominantly controlled by the starting pH value of the synthesis gel. Thus, the shape of the primary MnWO_4 nanoparticles in the hydrothermal product crucially depends on the starting pH and varies from cube-like particles (starting pH=6.3) to anisotropic nano-rods (starting pH=9.9) (Fig. 3.2). These changes are reflected in the aspect ratio of the MnWO_4 nanoparticles, which can be obtained by measuring length and width of the nanoparticles from the TEM images (Figs. 3.2, S3.4, and S3.5, Tab. 3.1). Before catalytic testing the as-synthesised materials have to be thermally treated above the reaction temperature of the catalytic reaction. Annealing in argon at 400°C has no significant influence on shape and size of the nanoparticles (Fig. 3.2), but the specific surface areas are slightly reduced (Table 3.1). Electron microscopy indicates a defect-rich structure and preferential growth of the rods along the $\langle 001 \rangle$ axis. Normally, crystallization and particle growth are induced by minimization of the free energy of the system. At the given chemical potential this observation suggests that the (001) surface is a high-energy surface. Thus, growing along $\langle 001 \rangle$ avoids its exposure to the environment. In addition, the fraction of surfaces with lower energies increases significantly, which improves the stabilization of the nanoparticle. In fact, analysis of the HAADF-STEM images of AR1.5 and AR5.1 allows for the allocation of specific facets of the particles, including (100), (010) and (110) crystal planes as illustrated in Fig. 3.3.

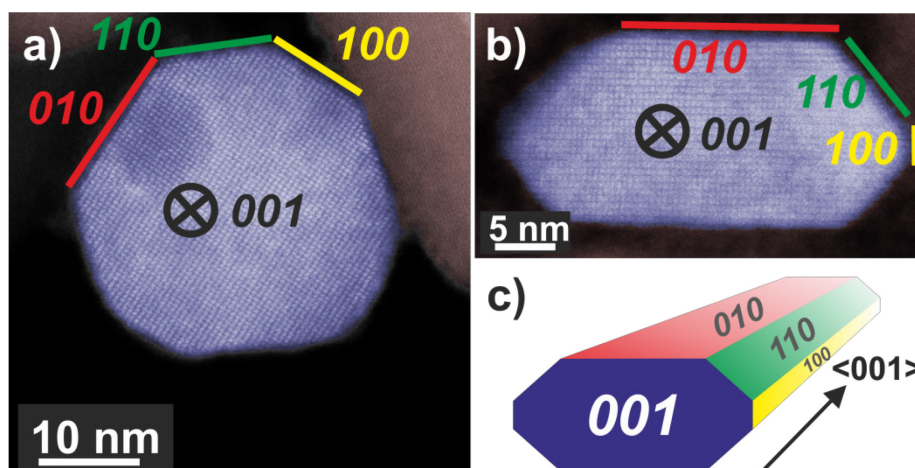


Figure 3.3 HAADF-STEM images of MnWO_4 nanoparticles viewed along $\langle 001 \rangle$ with different aspect ratios: a) AR1.5, b) AR5.1 and c) perspective model for a typical faceted nanoparticle. The original uncoloured images including Fast Fourier transform analysis are given in the Supporting Information, Fig. S3.6.

The dissolution-recrystallization processes occurring during ageing under hydrothermal conditions in the autoclave at 180°C are illustrated in Fig. 3.4. The dissolution of $[\text{WO}_4]^{2-}$ ions and the hydrolysis of $[\text{Mn}(\text{H}_2\text{O})_6]^{2+}$ species by deprotonation of water ligands is facilitated in basic environment in the presence of a high concentration of OH^- ions. Anisotropic growth is imaginable when the local structure of the WO_6 chains at different planes at the surface of the MnWO_4 crystals is taken into consideration. At the (010) crystal planes, edge sharing $-\text{O}-\text{W}-\text{O}-$ bonds are exposed that can be easily attacked by OH^- ions leading to dissolution of $[\text{WO}_4]^{2-}$ species. Hydrolysis is hindered at other planes, for example at (100) and (110), due to geometric reasons. Only half of the $-\text{O}-\text{W}-\text{O}-$ bridges in a WO_6 octahedron are exposed at these planes. Therefore, the WO_4 units cannot be dissolved. Free $[\text{WO}_4]^{2-}$ species could condense with $\text{W}-\text{O}(\text{H})$ groups at the high-energy (001) basal planes propagating the tungsten oxide zigzag chains by forming new edge sharing $\text{O}-\text{W}-\text{O}$ bonds (Fig. 3.4). Divalent manganese ions may interact with negatively charged tungstate chains and are in this way incorporated into the structure. With increasing OH^- concentration, the dissolution-recrystallization process is enhanced and nanoparticles with increased aspect ratio are formed as evidenced by particle size analysis (Fig. S3.5, Table 3.1). The statistical analysis based on the TEM images is in agreement with the average particle diameter found by XRD. With increasing initial pH value, the (010) peaks in the XRD patterns (Fig. S3.3) become more broadened, providing additional support for smaller crystallite sizes along the $\langle 010 \rangle$ direction with increasing pH (Table 3.1). During dissolution-recrystallization, hydrolysis of $[\text{Mn}(\text{H}_2\text{O})_6]^{2+}$ species leads to the formation of $\text{Mn}(\text{OH})_x$ species at the surface of the catalysts as indicated by an increasing intensity of the two bands at 619 and 665 cm^{-1} in the Raman spectra recorded during hydrothermal synthesis that are tentatively attributed to surface manganese oxide-hydroxide species.[71] The appearance of the corresponding bands is more distinct in reaction mixtures that contain a higher concentration of OH^- ions (compare Fig. 3.1a and c).

However, the concentration of dissolved tungsten oxide and manganese species is apparently rather low, since no peaks due to such species in solution are detectable by Raman spectroscopy using the immersion probe.

Table 3.1 Specific surface area, results of shape analysis based on TEM, and crystallite size calculated from anisotropic fitting in Rietveld refinement of the XRD patterns

Catalyst	Catalyst ID ^a	pH ^b	Surface area of hydrothermal product ^c (m ² /g)	Surface area of catalyst ^a (m ² /g)	Number of particles ^d	Mean particle length ^d (nm)	Mean particle diameter ^d (nm)	Mean aspect ratio ^d	$D_{<100>}$ ^e (nm)	$D_{<010>}$ ^e (nm)	$D_{<001>}$ ^e (nm)
AR1.5	19112	6.3	27.7	25.9	132	53.8	35.7	1.5	27.1	27.3	41.4
AR1.7	19113	6.7	26.1	22.9	124	59.0	35.1	1.7	27.2	26.3	46.8
AR3.2	19114	8.0	23.3	22.1	93	104	32.6	3.2	28.5	25.6	70.3
AR3.9	19251	9.1	25.7	24.0	125	119	30.8	3.9	27.2	22.1	65.3
AR5.1	19116	9.9	31.0	28.7	131	122	24.4	5.1	24.0	17.3	55.4

^a required to identify different batches of catalyst synthesis, catalyst after thermal activation at 400°C for 2 hours in Argon

^b pH value adjusted before the hydrothermal synthesis

^c after drying at 80°C

^d number average values analysed based on TEM images as shown in Figs. 2, S4 AND S5

^e based on XRD of the catalysts (Fig. S3)

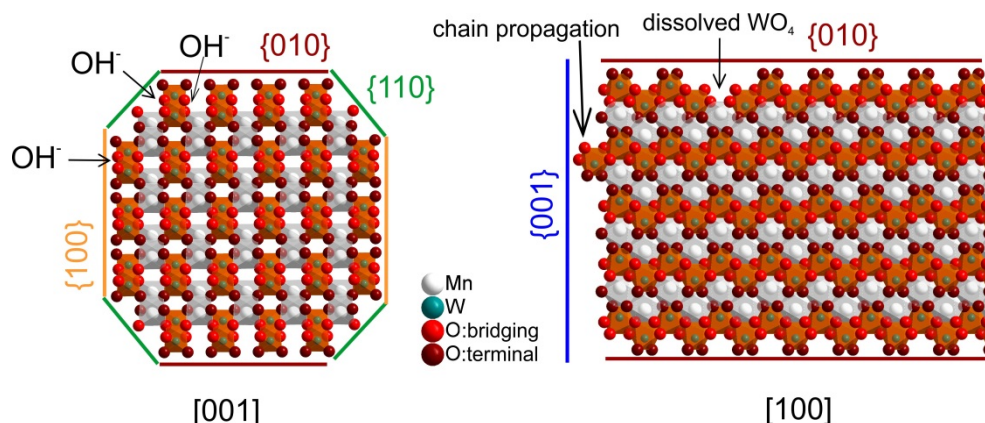


Figure 3.4 Schematic representation of the proposed anisotropic mechanism of particle growth.

3.2.2 Ethanol oxidation

The side products ethylene and diethyl ether in the oxidation of ethanol to acetaldehyde reveal the presence of extra acid/base functionalities at the catalyst surface of an oxidation catalyst. Ethanol oxidation has been performed over all catalysts within the reaction temperature range from 280 to 310°C achieving conversion of ethanol from 5 to 15% (Fig. S3.7). Under these conditions acetaldehyde as well as ethylene are formed over all catalysts, but the selectivity is different for the catalysts with different aspect ratios of their primary particles. In Fig. 5 the product distribution is

compared at 10% ethanol conversion. The ethylene selectivity is quite high over the catalyst AR1.5, but decreases as the aspect ratio increases.

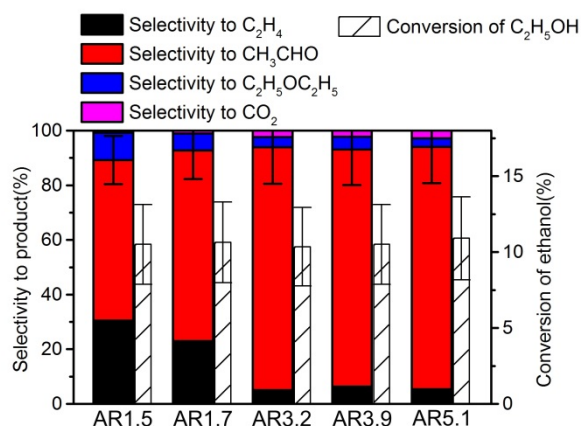


Figure 3.5 Selectivity in ethanol oxidation over the nanostructured MnWO₄ catalysts at 10% ethanol conversion.

The selectivity to acetaldehyde decreases with increasing temperature and conversion, whereas ethylene selectivity rises (Fig. S3.7). At constant temperature the selectivity to acetaldehyde decreases in general slightly with time on stream, whereas ethylene selectivity is quite constant or even increases (Fig. S3.7) suggesting no structural relations between redox and acid-base sites.

The specific rate of the acid-catalysed dehydration reaction decreases with increasing aspect ratio (Fig.

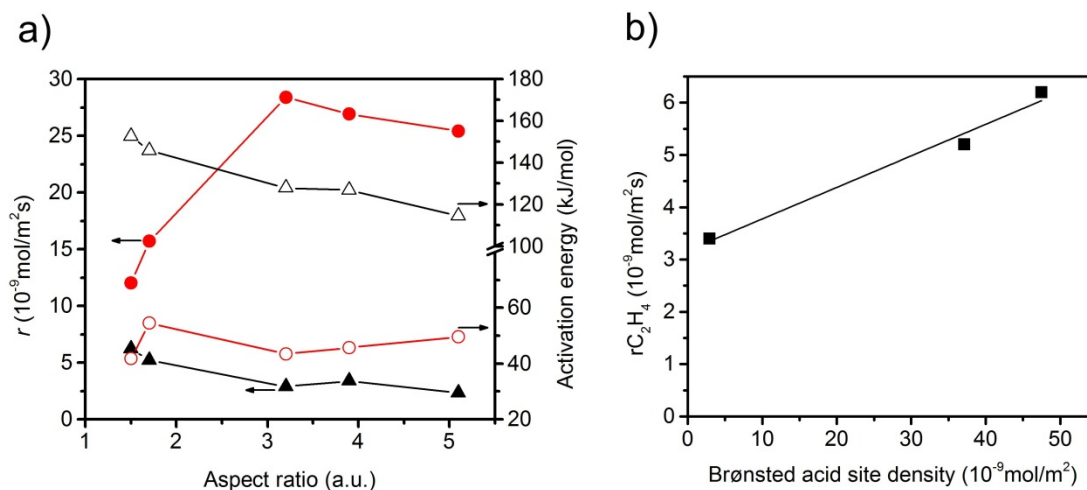


Figure 3.6 a) Specific reaction rates measured at T=310°C and normalized to surface area, and apparent activation energy as a function of the aspect ratio; Red solid circle: acetaldehyde formation rate; red open circle: apparent activation energy of acetaldehyde formation; black solid triangle: ethylene formation rate; black open triangle: apparent activation energy of ethylene formation; b) Rate of formation of ethylene as a function of Brønsted acid site density at the catalyst surface determined by ammonia adsorption and specific surface area measurements.

3.6). In contrast, the specific redox reaction rate exhibits a flat maximum at the aspect ratio 3.2. It should be noted at this point that the rates are integral rates. Conclusions about the intrinsic activity are not possible from these values. However, the apparent activation energy of ethanol oxidation is quite constant (48 ± 6 kJ/mol) suggesting that not the nature, but the number of active sites changes in the current catalyst series.

The observed trends may be related to a change in the relative fraction of acid-base and redox species at the catalyst surface that may be, again, related to differences in the termination of the catalyst particles within the current series. The presence of a defect rich MnO_x chain-like 2D over-layer, particularly, at the (010) termination of particles in the catalyst AR5.1 has been verified by electron microscopy and photoelectron spectroscopy.[104] These MnO_x chains might bear oxygen defects, which are believed to provide the active sites in the activation of propane. The same manganese oxide sites might be relevant for oxidation of ethanol in the present experiments as well. Due to the preferential growth of the particles along the $\langle 001 \rangle$ direction, the relative abundance of (010) planes that host these manganese oxide sites for oxidation catalysis may increase with increasing aspect ratio (Fig. 3.3). Therefore, an aspect ratio above three is reflected in increased integral rates of the oxidation reaction compared to the integral rates of acid-catalysed dehydration reaction over the corresponding catalysts. The sites responsible for dehydration may be, in contrast, preferentially located at the two ends of the rods, which are terminated by (001) crystal planes. According to structural considerations, Brønsted acid sites might be preferentially located at these planes (Fig. S3.8). Therefore, the two catalysts AR1.5 and AR1.7 exhibit enhanced acid-base functionalities, which is in agreement with the shape (Figs. 3.2, 3.3a)) and the proposed dissolution-recrystallization mechanism (Figs. 3.4, S3.8).

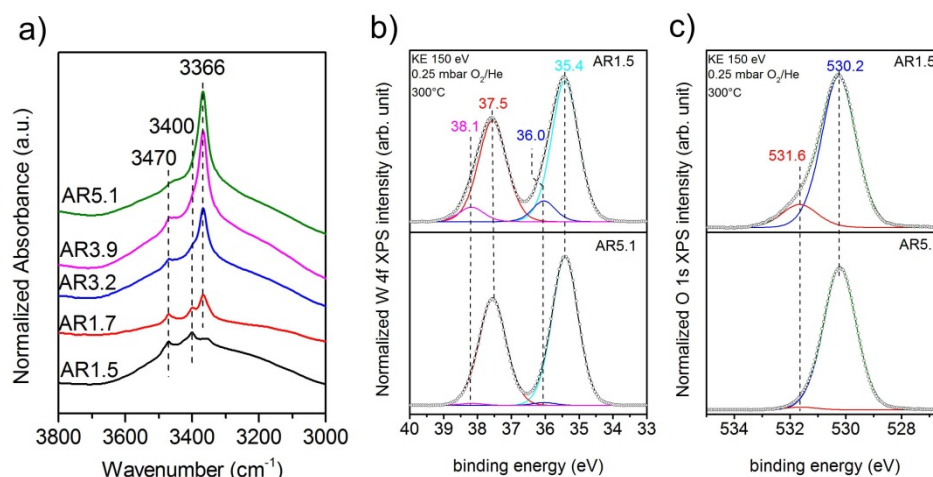


Figure 3.7 a) Infrared spectra in the region of OH stretching vibrations after thermal treatment of the catalyst in the infrared cell in vacuum at 300°C; The measurement was performed in vacuum at 40°C; W 4f spectra (b)), and O 1s spectra (c)) of the catalysts AR1.5 and AR5.1 measured by synchrotron-based near ambient pressure X-ray photoemission spectroscopy (NAP-XPS) at an inelastic mean free path (IMFP) of ca. 0.6 nm in 0.25 mbar in O₂/He at a total gas flow of 4.2 sccm at 300°C.

Experimentally, the acidity of the catalysts has been studied by infrared spectroscopy. After heating to reaction temperature of ethanol oxidation (300°C) in vacuum, three bands located at 3470, 3400, and 3366 cm⁻¹ are observed in the O-H stretching region on top of a broad feature (Fig. 3.7a)). The latter is attributed to hydroxy groups that undergo hydrogen bonding or strongly adsorbed water molecules, respectively. A residual band is observed at 1642 cm⁻¹ that might be due to the bending mode of molecular water, but discrimination of this band from overtones and combination vibrations of MnWO₄ is difficult. Based on the very low frequency and the unusual narrow bandwidth, the three sharp bands at 3470, 3400, and 3366 cm⁻¹ are tentatively assigned to hydroxy groups that form well-ordered hydrogen bonding networks at the surface. Further investigations are necessary to clarify the origin of these bands that are characterized by unusual low O-H stretching frequencies. To investigate the acidity of the hydroxy groups, NH₃ was adsorbed at the surface of the catalysts after evacuation at 300°C for 1 hour at 40°C. Unfortunately, the bands of adsorbed ammonia in the N-H stretching vibration region between 3400 and 3000 cm⁻¹ overlap with the hydroxy bands due to the low frequency of the latter (Fig. 3.7a)). Therefore, the consumption of particular OH species in the reaction with ammonia cannot be monitored. But weak acidity is confirmed by formation of a weak but distinct band at 1439 cm⁻¹ due to the asymmetric deformation vibration of ammonium ions formed by reaction of ammonia with Brønsted acid sites at the surface of the catalysts AR1.5, AR1.7, and AR3.9 (Fig. S3.9). No clear indications regarding redox processes of adsorbed ammonia molecules have been observed in the spectra. The concentration of acid sites at the surface of catalyst AR5.1 was below the detection limit. The small number of acid sites (in the range from 0 for AR5.1 to 1.2 μmol

g^{-1} for AR1.5) suggests that most of the OH groups observed in the infrared spectra of the catalysts after dehydroxylation at 300°C in vacuum (Fig. 3.7a)) are nonacidic in nature. Essentially all OH groups observed at the surface of catalyst 5.1 are not able to protonate ammonia. Therefore, the band at 3366 cm^{-1} that represents the dominant hydroxy species at the surface of catalyst AR5.1 is tentatively assigned to Mn-OH groups. A sharp band below 3500 cm^{-1} has been attributed to Mn-OH in the layered Mn^{2+} hydroxide $\text{Mn}_2(\text{OH})_2\text{SO}_4$. [105] The surface concentration of acid sites correlates with the formation rate of ethylene (Fig. 3.6b), demonstrating the involvement of these sites in dehydration of ethanol. The non-zero intercept of the fitting line in Fig. 3.6b) suggests that Lewis acid sites may be involved in dehydration of ethanol as well. Pathways leading to ethylene from ethanol adsorbed on Ce^{4+} have been discussed. [106] Similar reaction routes might also be possible at coordinatively unsaturated manganese or tungsten sites that are present at the surface of the catalysts as it becomes evident from ammonia adsorption (Fig. S3.9). The peak at 1591 cm^{-1} may arise from the asymmetric bending vibration of ammonia molecules adsorbed at Lewis acid sites.

A high concentration of hydroxy groups at the surface of the catalyst AR1.5 is also confirmed by NAP-XPS measured in presence of oxygen at 300°C . The O 1s core level spectra of the catalysts AR1.5 and AR5.1 are shown in Fig. 3.7c). The main peak at 530.2 eV is assigned to lattice oxygen, while the component at 531.6 eV is attributed to hydroxy groups. Fig. 3.7c) shows that catalyst AR 1.5 comprises a higher concentration of hydroxy groups than catalyst AR5.1. A detailed analysis of the W 4f core level reveals that also the W $4f_{7/2}$ and W $4f_{5/2}$ doublet (Fig. 3.7 b)) can be deconvoluted into two contributions. The low binding energy doublet at 35.4 and 37.5 eV is in good agreement with the binding energy values reported in the literature for metal tungstates. [107, 108] The high binding energy doublet at 36.0 and 38.1 eV is more pronounced in the AR 1.5 catalyst than in the AR5.1 catalyst, in line with the higher hydroxyl concentration observed in the O 1s spectrum of catalyst AR1.5. Furthermore, the contributions of the high binding energy W 4f doublet as well as the hydroxide component in the O 1s spectrum are decreasing with increasing probing depth (compare Figs. 3.7 b), 3.7 c), S3.10 a), S3.10 b)). Therefore, we tentatively assign the high binding energy doublet in the W 4f spectrum to modified tungsten atoms bearing hydroxy groups at the surface of the catalyst. Thus, the XPS measurements indicate that more W-OH groups are present at the surface of the catalyst containing primary particles with a low aspect ratio (AR1.5). These results are complementary to the characterization of the catalysts by ammonia adsorption. The acid sites probed by FTIRS of adsorbed ammonium ions are attributed to W-OH groups at the surface of the catalyst, which is also plausible in terms of the acid-base chemistry of tungsten compared to manganese. Mn-OH groups are apparently not resolved by XPS, neither in the O 1s spectra (Fig. 3.7c)), nor in the Mn 2p spectra (Fig. S3.11). The discrepancy between FTIRS and XPS concerning the presence of hydroxy groups at the surface of the two catalysts might be due to the fact that the Mn-OH contributions are enveloped by M-O contributions in the O1s (Fig. 3.7c)) and Mn2p (Fig. S3.11)

spectra, or due to differences in the pretreatment procedures before IR (vacuum, 300°C) and XPS (0.25 mbar O₂ at 300°C) measurements, respectively.

In summary, the variation of the initial pH in the hydrothermal synthesis of nanostructured MnWO₄ affects the dissolution-recrystallization kinetics of the freshly formed particles during ageing at 180°C. Although these dissolution and recrystallization processes are responsible for anisotropic particle growth, more important is that ageing provides the basis for the formation of the catalytically active sites. With increasing pH under hydrothermal conditions the fraction of acid W-OH groups at the surface of the final catalyst decreases and, consequently, acid-base catalysed side reactions during ethanol oxidation are increasingly suppressed, which is reflected in enhanced selectivity to acetaldehyde with increasing starting pH (Fig. 3.5).

Selectivity is the major issue in oxidation catalysis.[58, 109] Activation of C-H bonds in saturated hydrocarbons is challenging because the formed reaction products and intermediates easily undergo consecutive and parallel reactions. Minimization of rates of undesired pathways requires co-ordinated design of bulk electronic properties and surface dynamics of oxidation catalysts.[68] C-H bond activation may involve multiple mechanisms including carbenium or carbonium intermediates and homolytic splitting of C-H bonds at metal oxide surface functional groups under formation of radical species.[110, 111] Model calculations, generally based on small cluster models, favour the homolytic pathway over transition metal oxide catalysts.[112] However, Lewis acid sites in terms of coordinatively unsaturated metal cations and Brønsted acid sites may be present at the surface of a transition metal oxide under reaction conditions as well. Brønsted acid sites are particularly expected since water is an unavoidable coproduct in oxidation reactions and, as demonstrated in the current example, the dehydroxylation temperature is often above the reaction temperature.

Whereas acidity at the surface of nanostructured MnWO₄ catalysts is attributed to the presence of W-OH groups and coordinatively unsaturated metal cations, the origin of redox activity is not that straightforward. During particle growth under hydrothermal conditions the formation of defects may occur. In the course of dissolution and recrystallization chemical defect in terms of cationic vacancies or OH⁻ groups at anionic positions are generated that may be related to structural defects.[113] Establishing relations between defect chemistry and redox activity requires further kinetic studies and more comprehensive characterization of the catalysts, which is currently under way.

3.3 Conclusions

Nanostructured MnWO₄ catalysts have been prepared by hydrothermal synthesis. The aspect ratio of the primary MnWO₄ particles increases with increasing pH during ageing at 180°C under hydrothermal conditions. Electron microscopy revealed that the particles grow along the <001> axis. A mechanism of particle growth by dissolution re-crystallization is proposed that leads to an increase

in the fraction of terminating (010) planes with increasing aspect ratio. At the same time, the fraction of (001) planes, which are terminated by W-OH groups, is decreasing. These changes are reflected in the selectivity patterns of the ethanol oxidation reaction that probes both, redox and acid-base sites. Metastable structures are required to achieve catalytic activity over MnWO_4 . Solid-state synthesis provides these structures only on a limited scale. The implementation of chemical defects as basis for catalytic activity of MnWO_4 succeeded via the variation of the chemical potential under mild hydrothermal conditions.

3.4 Experimental details

3.4.1 Hydrothermal synthesis

The hydrothermal synthesis of MnWO_4 was performed in an analytical autoclave HPM-PT-040 (Premex Reactor GmbH) described before[99] adopting a synthesis method that has been reported previously.[100] In the first step, a 0.2 M aqueous solution of $\text{Mn}(\text{NO}_3)_2$ ($\text{Mn}(\text{NO}_3)_2 \cdot 4\text{H}_2\text{O}$, 98%, Roth) was added to a 0.2 M aqueous solution of Na_2WO_4 ($\text{Na}_2\text{WO}_4 \cdot 2\text{H}_2\text{O}$, 99%, Sigma Aldrich) while stirring leading to a mixed solution of pH=6.7. Subsequently, the pH of the mixed solution was adjusted to 6.3, 8.0, 9.1, and 9.9 by adding appropriate amounts of 0.1 M HNO_3 (64-66%, Sigma Aldrich) or 0.1 M NaOH (98%, Alfa Aesar), respectively. The mixtures were transferred to the autoclave and the temperature was raised from 20°C to 180°C at a rate of 5 °C/min. The synthesis temperature was kept at 180°C for 12 h. During hydrothermal synthesis the pH was recorded using a pH probe (ZrO_2 probe Model A2 and Ag/AgCl reference electrode, both with a 1/2" outer tubing made from Hastelloy C-276; Corr Instruments). The pH probes were calibrated by use of four buffer solutions at the given reaction temperatures prior to the experiments. At the same time the Raman spectra of the synthesis gels were recorded using a Raman probe (RAMAN RXN1, immersion optic 1/4"OD (HC-276); Kaiser Optical Systems). After cooling down the gel at a rate of 5 °C/min, the products of hydrothermal synthesis were filtered by centrifugation and washed twice with de-ionized water (MilliPore®). In the final step, the solids were dried in a muffle furnace in air at 80°C for 12 h. Depending on the pH value before hydrothermal treatment, yellowish to brownish solids were collected. The solids were annealed in Argon (flow rate: 50 mL/min) at 400°C (heating rate 5 °C/min) for 2 h using a rotary tube furnace (XERION) resulting in five phase-pure MnWO_4 catalysts with different mean aspect ratios (AR) characterized by the identification numbers 19112 (AR=1.5), 19113 (AR=1.7), 19114 (AR=3.2), 19251 (AR=3.9), and 19116 (AR=5.1). The catalysts are called AR_{x.x}, whereas x.x corresponds to the mean aspect ratio of the particles in the materials after thermal activation as determined by analysis of transmission electron microscopy images.

3.4.2 Characterization of catalysts

Transmission electron microscopy (TEM) studies were conducted on a Philips CM200 FEG transmission electron microscope operating at 200 kV. High resolution TEM (HRTEM) and high resolution high angle annular dark field scanning transmission electron microscopy (HAADF-STEM) were performed on a Cs corrected FEI TITAN 80-300 operated at 300 kV. TEM samples were prepared by drop deposition from ethanolic suspensions onto lacey-carbon coated Cu grids, and by cross section preparation.

Field emission scanning electron microscopy (FESEM) was carried out with a Hitachi S4800 instrument operating at 5 kV.

XRD measurements were conducted as described in section 2.4.2.2

The specific surface area was measured in a volumetric N₂ adsorption device (Autosorb-6-B, Quantachrome) at the temperature of liquid nitrogen. The sample was degassed in dynamic vacuum at a temperature of 300°C for 2 h prior to adsorption. The relative N₂ pressure was varied and 11 data points were measured. The linear range of the adsorption isotherm ($p/p_0=0.05-0.3$) was considered to calculate the specific surface area according to the BET method.

Ethanol oxidation was performed at atmospheric pressure in a feed composed of 30.2 mL N₂, 2.8 mL O₂ and 1.2 mL CH₄. The feed was passed through a saturator at 15°C to achieve a concentration of 4 vol% ethanol. A laboratory quartz U-tube fixed bed reactor (4 mm inner diameter, 6 mm outer diameter, 26 cm length) was used, which contained 200 mg of the catalyst previously pressed and sieved to a particle size of 250-355 µm. Gas analysis was performed by online gas chromatography (GC 6890A, Agilent) equipped with two channels. A combination of two capillary columns (GS-Carbonplot and Plot Mole Sieve 5A) in connection with a thermal conductivity detector (TCD) was used to analyse the permanent gases CO₂, O₂, N₂ and CO. A combination of two capillary columns (HP-FFAP and HP Plot Q) connected to a flame ionization detector (FID) was applied to analyse alkanes, olefins and oxygenates.

Transmission Fourier transform infrared spectroscopy (FTIRS) measurements were carried out using a Varian 670 spectrometer equipped with a MCT detector. The spectra were recorded at a resolution of 4 cm⁻¹ accumulating 512 scans. Self-supported wafers (area weight of 23-29 mg cm⁻²) were transferred into an IR cell that was connected to a vacuum system, in which residual pressures of ca. 1·10⁻⁶ mbar can be employed. Prior to the adsorption of gases, the catalysts were heated in dynamic vacuum at 300°C for 1h. A reference spectrum of the solid was taken after cooling down to 40°C. Then, the sample chamber was charged with 7 mbar partial pressure of NH₃ at 40°C. After 30 min, spectra were recorded applying the spectrum of the pretreated MnWO₄ as background. The Brønsted acid site density was calculated applying the extinction coefficient 16 cm µmol⁻¹. [114]

Near-ambient-pressure X-ray photoelectron spectroscopy (NAP-XPS) was conducted at the end station of the ISSS beam line at BESSY II/HZB (Helmholtz-Zentrum Berlin, Germany). Details of the setup have been published earlier.[115] For the XPS measurements, Mn 2p, O 1s, and W 4f core level spectra were collected at constant kinetic energies (KE) of the photoelectrons of 150 eV and 750 eV, resulting in inelastic mean free paths (IMFP) of the excited photoelectrons of ~0.6 nm (150 eV, denominated as surface) and ~1.6 nm (750 eV, denominated as deep), respectively. The experiments were performed at 300°C and a total pressure of 0.25 mbar in a 1/1.1 O₂/He mixture with a total gas flow of 4.2 sccm.

3.5 Supporting information

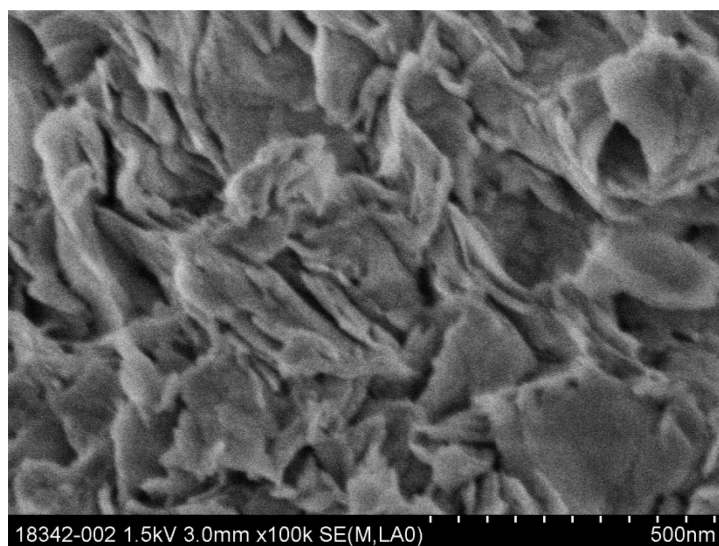


Figure S 3.1 SEM image of the intermediate formed by reaction of manganese nitrate with sodium tungstate at room temperature.

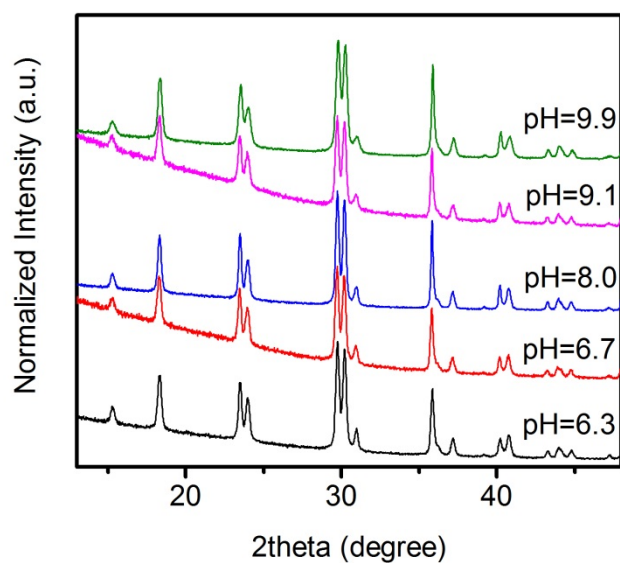


Figure S 3.2 XRD patterns of the hydrothermal products; The pH of the starting solution is provided in the legend of the figure. For allocation of the corresponding final catalyst, please refer to Table 3.1 in the main text.

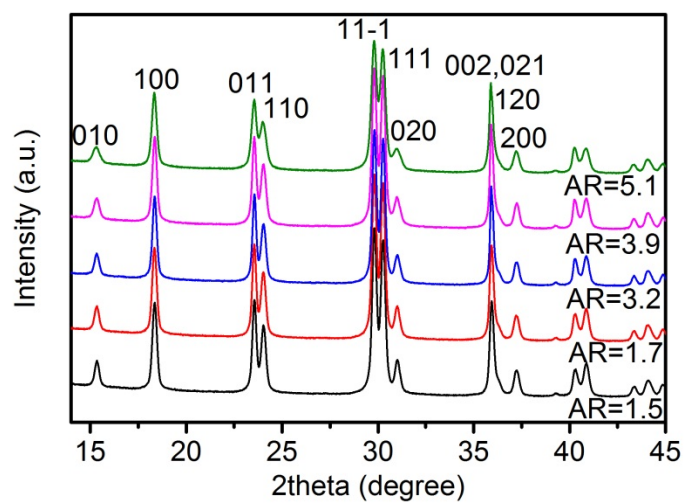


Figure S 3.3 XRD patterns of the catalysts after activation by thermal treatment of the hydrothermal products in flowing Ar at 400°C.

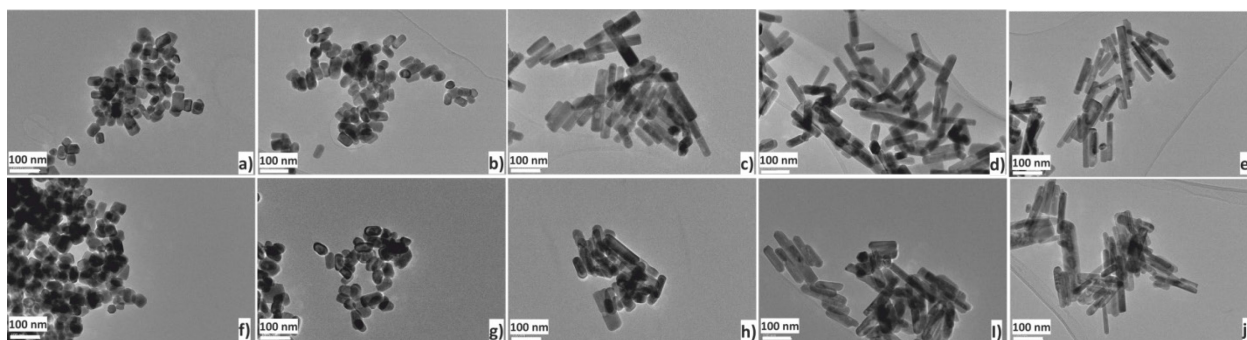


Figure S 3.4 TEM micrographs of as-synthesized (top row) and at 400 °C thermally activated (bottom row) nanostructured MnWO_4 catalysts with different aspect ratio: 1.5 (a) and (f), 1.7 (b) and (g), 3.2 (c) and (h), 3.9 (d) and (i), 5.1 (e) and (j).

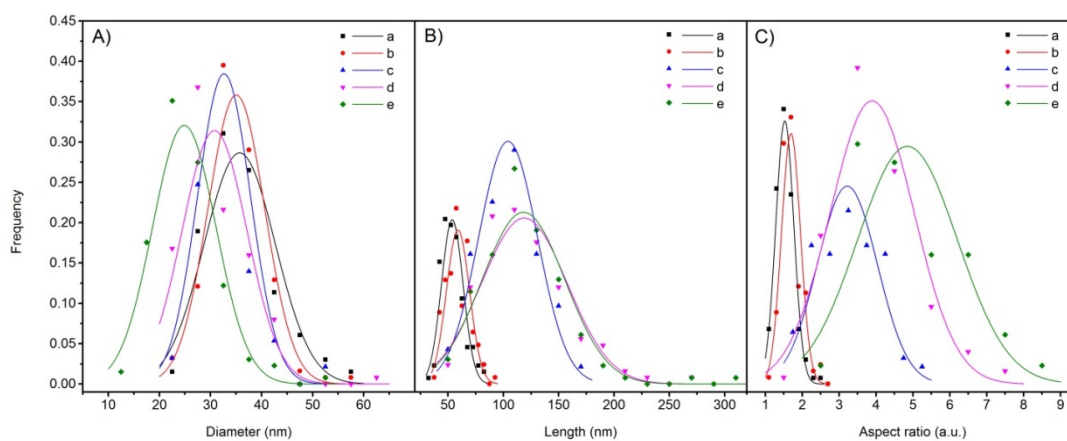


Figure S 3.5 Distribution of A) diameter, B) length and C) aspect ratio of the nanostructured MnWO_4 catalysts after thermal treatment; In each plot, a, b, c, d, and e represent the catalysts AR1.5, AR1.7, AR3.2, AR3.9, and AR5.1, respectively.

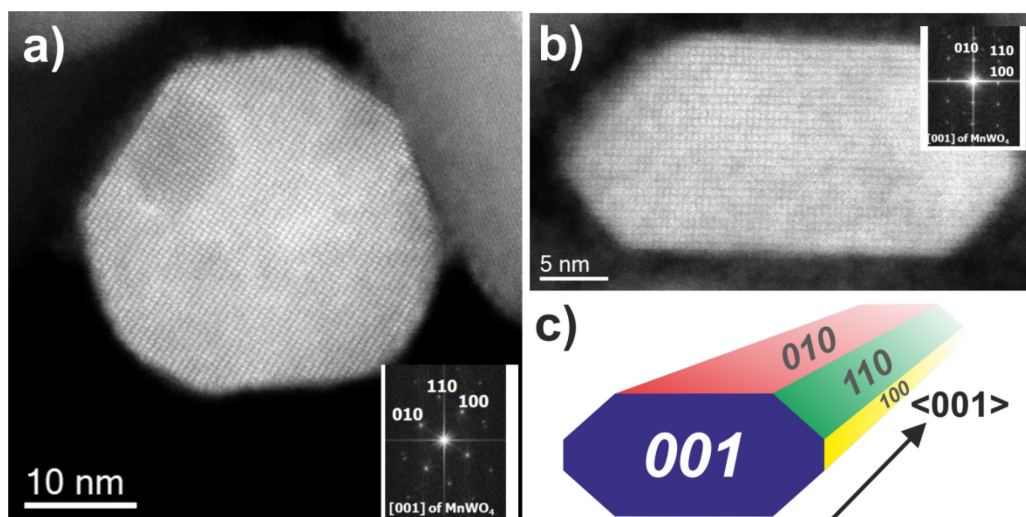


Figure S 3.6 HAADF-STEM images of MnWO_4 nanoparticles viewed along $\langle 001 \rangle$ with different aspect ratios: a) AR1.5, b) AR5.1 and c) perspective model for a typical faceted nanoparticle.

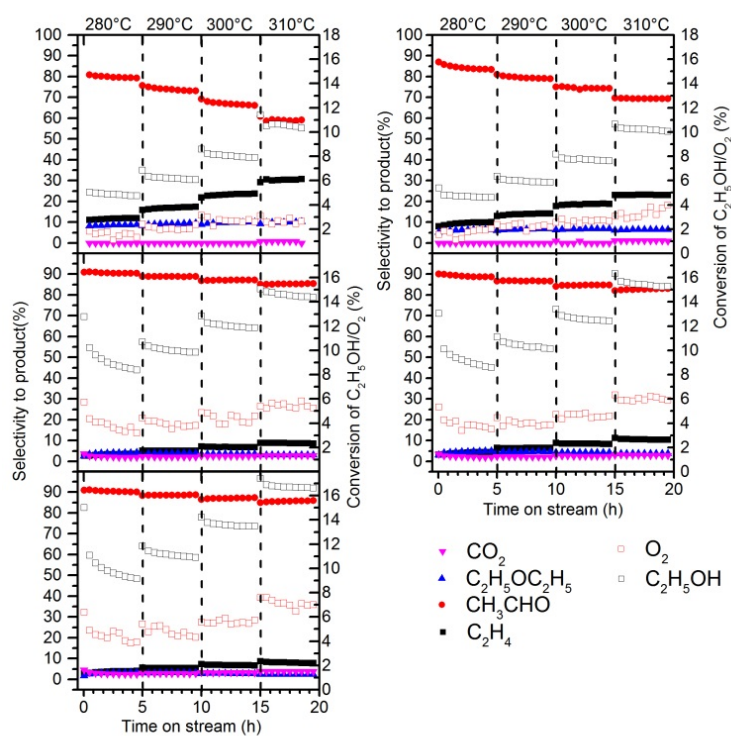


Figure S 3.7 Catalytic performance of top-left) AR1.5, top-right) AR1.7, middle-left) AR3.2, middle-right) AR3.9, and bottom-left) AR5.1 sample in ethanol oxidation reaction at different temperatures; For reaction conditions see Experimental in the main text.

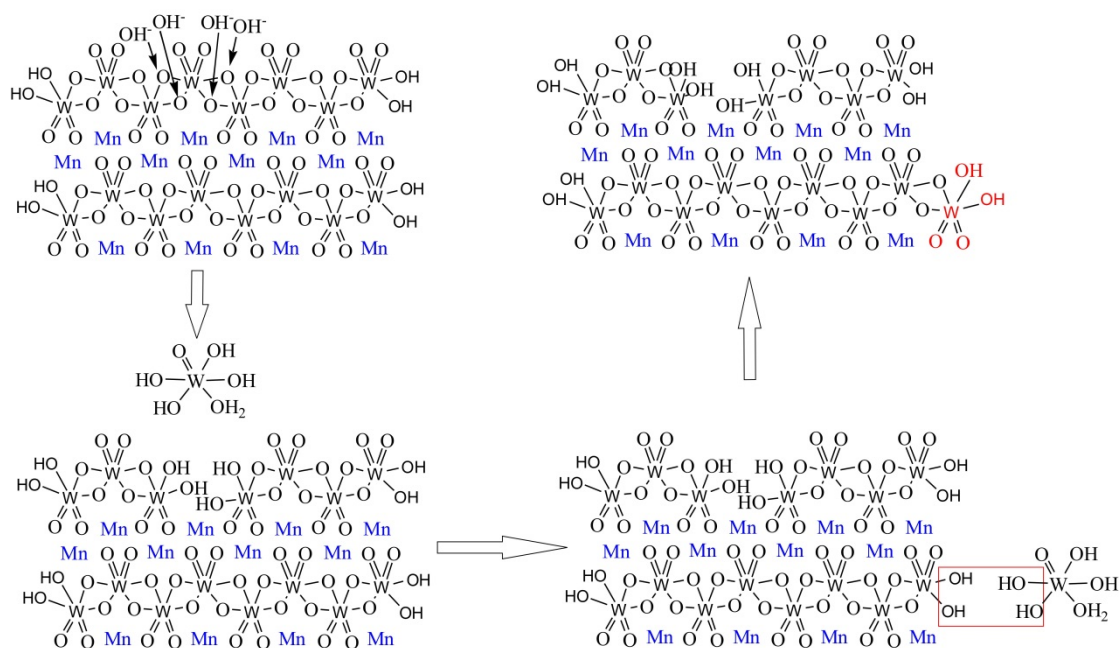


Figure S 3.8 Schematic representation of the formation of W-OH groups at (001) planes during dissolution-recrystallization under hydrothermal conditions at 180°C.

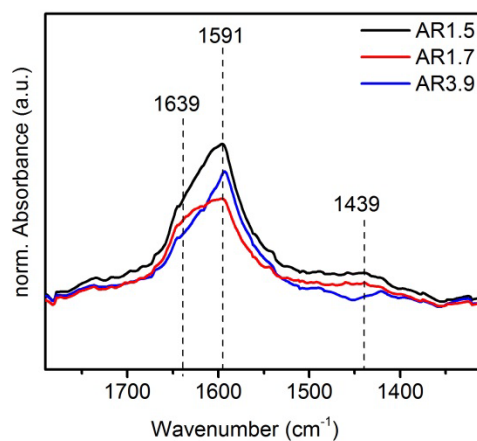


Figure S 3.9 FTIR spectra of NH_3 adsorbed at the surface of the catalysts AR1.5, AR1.7, and AR3.9 after pretreatment at 300°C for 1h in vacuum; Adsorption of ammonia was performed at 40°C; The spectra have been recorded in presence of gas phase ammonia ($p=6.508\text{--}7.042$ mbar).

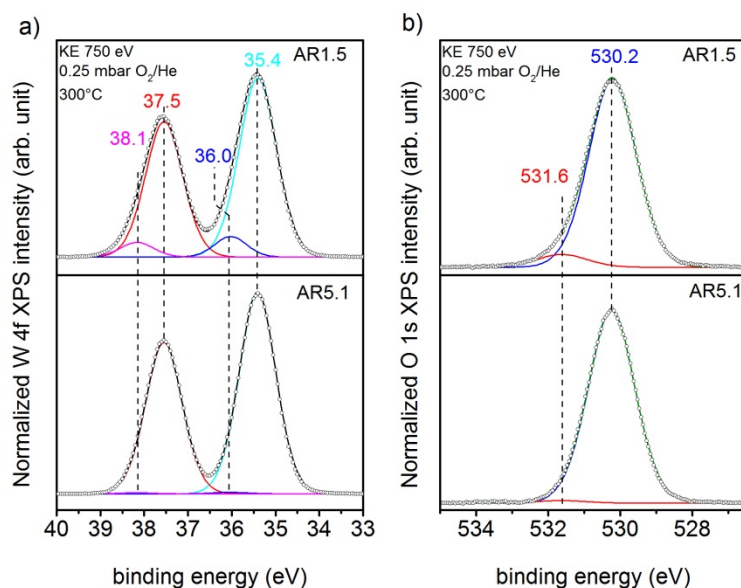


Figure S 3.10 W 4f spectra (a)), and O 1s spectra (b)) of the catalysts AR1.5 and AR5.1 measured by synchrotron-based near ambient pressure X-ray photoemission spectroscopy (NAP-XPS) at an inelastic mean free path (IMFP) of ca. 1.6 nm in 0.25 mbar in O₂/He at a total gas flow of 4.2 sccm at 300°C.

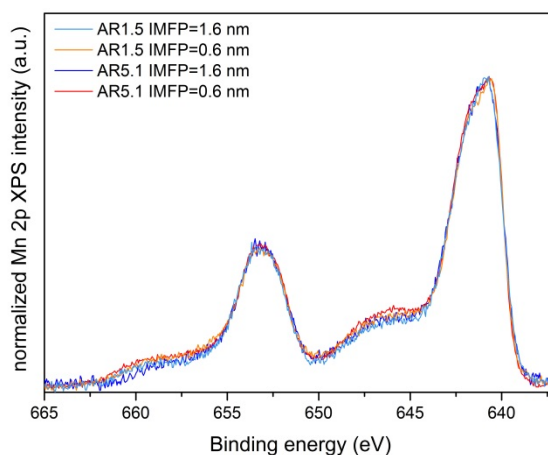


Figure S 3.11 Mn 2p spectra of the catalysts AR1.5 and AR5.1 measured by synchrotron-based near ambient pressure X-ray photoemission spectroscopy (NAP-XPS) at an inelastic mean free path (IMFP) of ca. 0.6 nm (a) and 1.6 nm (b) in 0.25 mbar in O₂/He at a total gas flow of 4.2 sccm at 300°C.

3.6 Acknowledgement

This work was conducted in the framework of the BasCat collaboration between BASF SE, TU Berlin, FHI, and the cluster of excellence “Unified Concepts in Catalysis” (UniCat). X.L. acknowledges the Berlin International Graduate School of Natural Sciences and Engineering (BIG NSE) as part of UniCat for financial support. The authors thank Maike Hashagen and Jasmin Allan for technical assistance. We thank the HZB staff for their continual support of the electron spectroscopy activities of the FHI at BESSY II.

4 Hydrothermal Synthesis and Characterization of Nanostructured CoWO₄ as Catalysts for Oxidative Dehydrogenation of Propane

Abstract: Phase-pure CoWO₄ catalysts were prepared by hydrothermal synthesis followed by thermal treatment in Ar at 400°C for 2 hours. The catalysts were characterized by different techniques, such as N₂ adsorption, X-ray diffraction, X-ray photoelectron spectroscopy, scanning electron microscopy, transmission electron microscopy, and Raman spectroscopy. The tungstate and binary reference oxides were tested in the oxidative dehydrogenation of propane. Higher pH value before hydrothermal treatment gives rise to higher Co/W ratio in the near surface region. Moreover, a correlation between the specific propane consumption rate and the Co/W ratio determined by XPS was observed. Enrichment of the surface in W leads to low selectivity to propene. The selectivity to conversion trajectory of such a catalyst resembles that of mesoporous tungsten oxide. The catalyst with the highest Co/W ratio exhibits termination by a Co chain structure on the (010) crystal planes as confirmed by HRTEM. FT-IR spectroscopy reveals surface Co bridging hydroxyl groups, which are responsible for a band centered at 3387 cm⁻¹. The presence of such an Co oxo-hydroxy terminating layer might be responsible for the high activity and selectivity in oxidative dehydrogenation of propane *via* a redox-type hydrogen abstraction.

KEYWORDS: cobalt tungstate, oxidative dehydrogenation of propane, hydrothermal synthesis, nanostructure, site-isolation

4.1 Introduction:

Oxidative dehydrogenation of propane (ODP) is advantageous compared to catalytic dehydrogenation of propane in view of several aspects including, for example, thermodynamic limitation, coke formation, heat of reaction, and stability.[7, 16, 59]. However, consecutive oxidation of propene to carbon oxides in ODP represents the major obstacle in terms of economic feasibility.[11, 59] Novel catalytic materials are required, which are able to activate C-H bonds in propane selectively. A class of molybdates has been investigated in the oxidative dehydrogenation of propane.[8] The study revealed that mixed Ni-Co molybdates show most promising performance in terms of selectivity, but at comparatively high reaction temperatures (550°C). Tungstates are generally less selective than molybdates, but an acceptable selectivity was reported for CoWO₄. [10] In a recent work dealing with mixed Ni-W-O oxides, the author concluded that Ni oxide is more active and shows constant

selectivity in a wide range of propane conversion, whereas W oxide is less active and selective.[24] However, in all previous studies, the preparation procedure is based on precipitation followed by a calcination step at relatively high temperature (above 500°C) resulting in low surface area materials and/or a mixture of phases.

When hydrothermal techniques are applied, the variation of process conditions may result in particles with varying shape, bulk electronic structure, and surface termination. The shape of MnWO₄ particles influences acid base properties and the nature of the catalytically active sites on the surface.[104, 116] The regular shape of the nanoparticles facilitates the application of a combination of integral methods and local methods, such as TEM, to investigate the nature of active sites. Mn oxide chains on the (010) surface of MnWO₄ crystals have been proposed to be responsible for selective propane activation. The unique nanostructure makes MnWO₄ active at comparatively low temperature (400°C) and almost as selective as VO_x/SBA-15.[104] In our previous study, general structural requirements of an ODP catalyst are proposed. It is postulated that bridge-type hydroxyl groups connecting redox active elements, which are embedded in an inert bulk oxide, are ideal active site precursors. To verify our hypothesis, nanostructured CoWO₄ was prepared by hydrothermal synthesis and investigated in the oxidative dehydrogenation of propane.

4.2 Results and discussion

The preparation of monoclinic cobalt tungstate composed of the wolframite-type structure was performed by hydrothermal synthesis at 180°C for 12 hours in aqueous medium. The formation of the solid inside the autoclave has been monitored by in-situ Raman spectroscopy (Figure 4.1). The synthesis products are denominated as CoW_{x.x}, whereas x.x indicates the pH value of the initial suspension obtained after mixing the aqueous cobalt nitrate and sodium tungsten precursor solutions in the autoclave at room temperature. During the synthesis of CoWO₄, an intermediate is formed as evidenced by the appearance of a band at 937-941 cm⁻¹, which can be attributed to polytungstate species (Figure S 1 and 2). With increasing temperature, mono- or poly- tungstate species are transformed into the wolframite type metal tungstate as evidenced by the occurrence of a peak at 884-885 cm⁻¹. Phase transition is accelerated with increasing the pH.

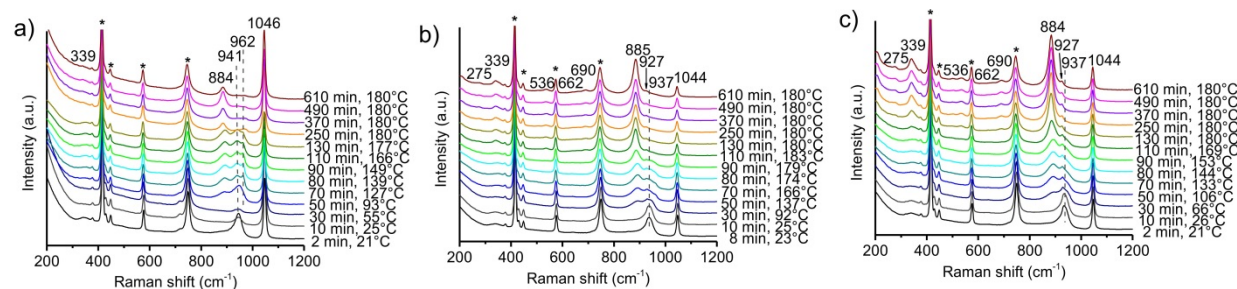


Figure 4.1 In situ Raman spectra recorded during the synthesis of the catalysts a) CoW6.2, b) CoW7.6 and c) CoW8.5.

Rietveld refinement of the XRD patterns (Figure 4.2) confirms phase-purity of all CoWO₄ catalysts. The aspect ratio (AR) of the catalysts (Summarized in Table 4.1) is estimated based on anisotropic fitting of the data.

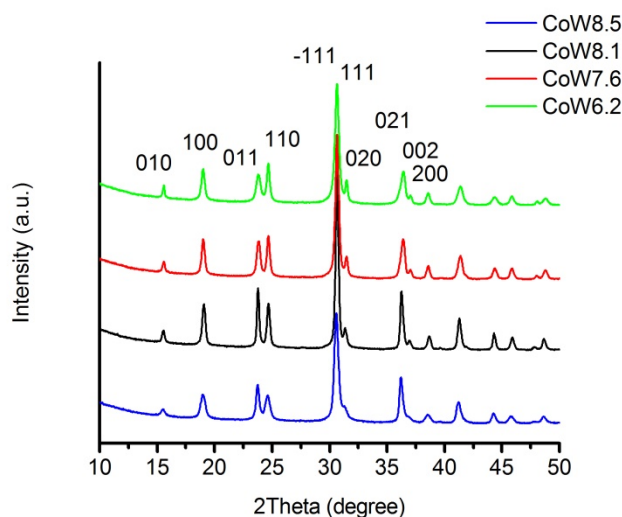


Figure 4.2 XRD patterns of as-synthesized CoWO₄ catalyst precursors.

The SEM images (Figure 4.3) show that the hydrothermally synthesized CoWO₄ materials are nanostructured. It can be seen that CoW8.5 is more rod-shaped than the other CoWO₄ catalysts in agreement with the aspect ratio determined by XRD (Table 4.1). The ratio of the dimension in different crystallographic directions ($\langle 001 \rangle / \langle 010 \rangle$) increases monotonically with increasing pH value.

Table 4.1 Specific surface area, synthetic parameters and crystallite size calculated from anisotropic fitting in Rietveld refinement of the XRD patterns.

Catalyst	Catalyst ID ^a	pH before hydrothermal synthesis	Acid ^b or Base ^c used (g)	pH after hydrothermal synthesis	S _{BET} (m ² g ⁻¹)	D _{<100>} ^d (nm)	D _{<010>} (nm)	D _{<001>} (nm)	D _{<100>/D_{<010>}}	D _{<001>/D_{<010>}}
CoW6.2	22787	6.2	27.1 ^b	1.6	42.0	20.1	37.1	12.8	0.5	0.3
CoW7.6	22785	7.6	0	n.d.	33.5	22.0	30.4	18.4	0.7	0.6
CoW8.1	23615	8.1	6.2 ^c	n.d.	22.4	22.5	23.2	44.5	1.0	1.9
CoW8.5	22786	8.5	13.1 ^c	9.5	35.6	13.6	13.1	35.8	1.0	2.7

^a Solid sample after thermal treatment in Ar at 400°C for 2 h

^b 1 mole L⁻¹ aqueous HNO₃

^c 1 mole L⁻¹ aqueous NaOH

^d based on XRD of the catalysts (Figure 4.2)

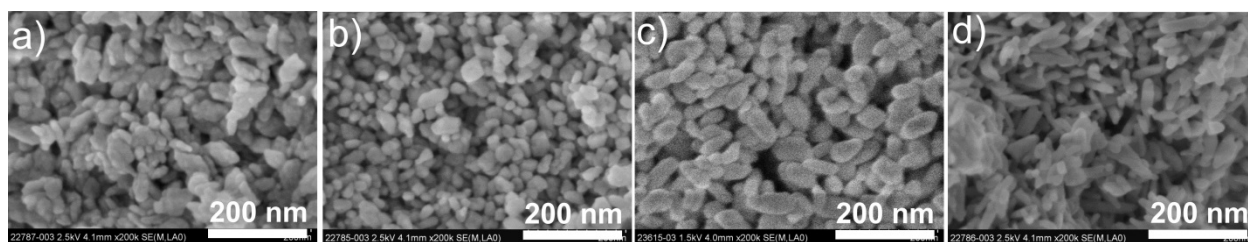


Figure 4.3 SEM images of the a) CoW6.2, b) CoW7.6, c) CoW8.1 and d) CoW8.5 catalysts.

In addition to the rod shaped structure, particles with flat surfaces can be detected by STEM (Figure 4.4). Particles with a diameter of 10-20 nm and length of 20-60 nm can be observed. At higher magnification, one image revealed a hexagonal shape of the cross section viewed along the $\langle 001 \rangle$ direction (Figure 4.5 a). The side planes can be determined as (110), (100) and (010) facets. At an atomic level, viewing from $\langle 100 \rangle$ direction, smaller bright dots with lower contrast at the outmost surface are observed in zig-zag chains on top of the larger brighter dots (Figure 4.5 b). Because in HAADF-STEM the contrast is due to Rutherford scattering proportional to approximately Z^2 , the smaller bright dots with less contrast should be attributed to Co atoms, suggesting surface termination on the (010) crystal planes by Co chains. Another bright field image along the $\langle 100 \rangle$ direction also indicates Co surface termination (Figure 4.5 c).

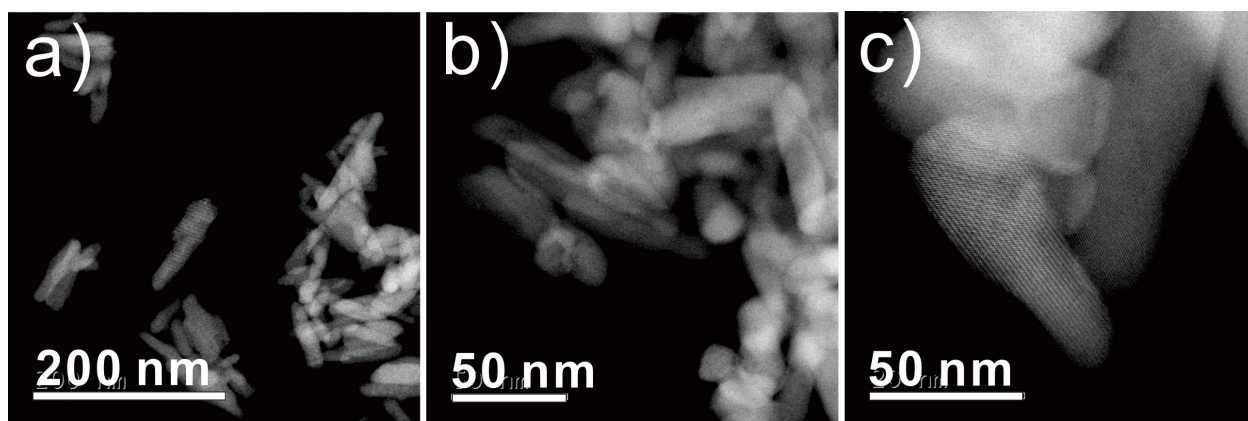


Figure 4.4 HAADF-STEM images of the CoW8.5 catalyst.

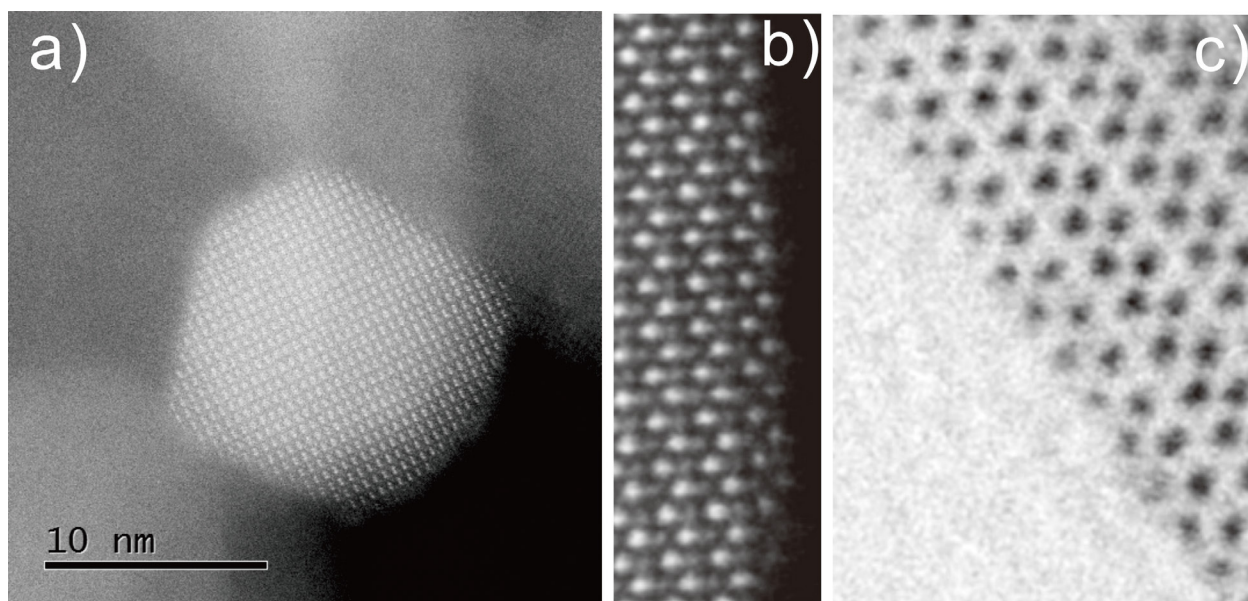


Figure 4.5 a) HAADF-STEM image of one particle in the CoW8.5 catalyst viewed along the $\langle 001 \rangle$ direction, b) HR-STEM-HAADF and c) HR-STEM-BF images of the surface of the same catalyst viewed along the $\langle 100 \rangle$ direction.

Table 4.2 Surface-near molar ratios of CoWO₄ according to XPS.

	Co/W	O/(Co+W)	Na/(Co+W)	C/(Co+W)
CoW6.2	0.83	2.53	0.034	0.16
CoW7.6	0.92	2.45	0.21	0.073
CoW8.1	1.24	2.00	0.10	0.065
CoW8.5	1.52	2.05	0.092	0.064

The Co/W ratio (Table 4.2) increases monotonically with higher pH before hydrothermal synthesis, which might be caused by dissolution of tungsten oxide in alkaline medium under hydrothermal condition. The high Co/W ratio of the CoW8.5 catalyst suggests an enrichment of Co surface. The Co 2p spectra indicate that cobalt exists in the oxidation state 2+ after thermal activation in He gas atmosphere at 400°C (Figure S4.3).

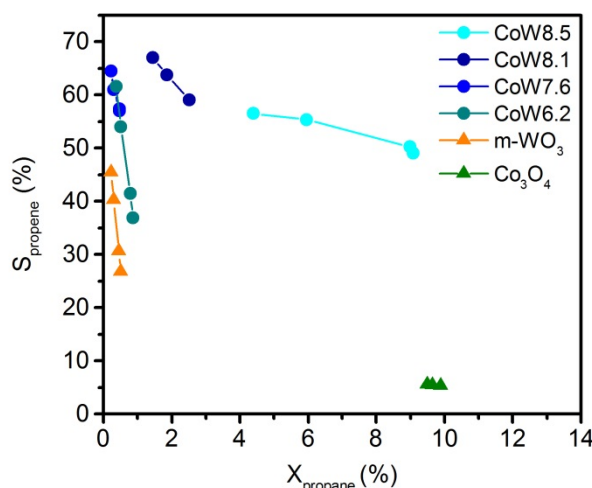


Figure 4.6 Catalytic performance of mesoporous WO₃, commercial Co₃O₄ and nanostructured CoWO₄ catalysts (T=400°C, W/F=0.9-2.4 g s mL⁻¹) in the oxidative dehydrogenation of propane in a C₃H₈/O₂/N₂ feed (10:5:85). The selectivity to propene is shown as a function of propane conversion. Other carbon-containing products are mainly CO and CO₂.

The catalysts and reference oxides have been studied in propane oxidation at 400°C (Figure 4.6). CoW6.2 and CoW7.6 are only slightly more active than m-WO₃ (Figure 4.6). CoW8.5 shows 50% selectivity to propene at 9% propane conversion. The reaction temperature was 160°C compared to the reaction temperature applied in previous studies over molybdates and tungstates prepared by precipitation.[10] The CoW8.5 catalyst also shows the highest specific propane consumption rate (Figure 4.7). The steady state propane consumption rate correlates with the Co/W ratio in the near surface region on the CoWO₄ catalysts (Figure 4.7), indicating that cobalt oxide species might be responsible for activity. Interestingly, the most active CoW8.5 catalyst, which is enriched in Co on the surface, is much more selective than pure cobalt oxide. The latter is a combustion catalyst, giving ca. 6% selectivity to propene at 10% propane conversion. In analogy to MnWO₄ catalysts, site isolation of the redox active species might be responsible for the much higher selectivity of CoWO₄ compared to bulk Co₃O₄.

The superior performance of the CoW8.5 catalyst might be attributed to its surface termination by CoO_x chains on (010) planes as suggested by STEM and XPS. The very high CO₂/CO ratio, (325 to 410), on this catalyst is another indication that CoO_x species are active sites, because pure cobalt oxide shows a CO₂/CO ratio over 1000 (Figure S4.4). The CO₂/CO ratio on the CoWO₄ catalysts series increases with increasing Co/W ratio in the near surface region. At the ODP reaction temperature, it is highly likely that the formed CO can be consecutively oxidized to CO₂. With higher

contact time, the propene formation rate decreases, whereas the CO₂ formation rate increases (Figure S4.5), suggesting a possible consecutive combustion of propene into carbon dioxide.

At room temperature, the infrared spectrum of CoW8.5 in the O-H stretching region is characterized by a strong signal at 3377 cm⁻¹ due to well-defined OH groups on the surface (Figure 4.8 a). Interestingly, the band is not very much perturbed by adsorption of molecular water that causes the broad base line in the room temperature spectrum in the range 3800-3000 cm⁻¹. Dehydration and perhaps also partial dehydroxylation at 400°C in He flow results in a sharp peak at 3387 cm⁻¹ attributed to Co-(OH)-Co type hydroxyl groups. However, a direct correlation between the surface concentration and the intensity of the peak is not observed. Dehydroxylation of the surface may result in surface defect formation, which is essential for oxygen activation in the oxidative dehydrogenation of propane. A partially de-hydroxylated, oxidized surface would then tend to abstract hydrogen from propane. The catalysts CoW6.2, CoW7.6, and CoW8.1 show sharply decreasing selectivity with increasing conversion (Figure 4.6). The infrared spectra of these catalysts exhibit a band at 3674 cm⁻¹ due to acidic W-OH groups, which is missing on the surface of the catalysts CoW8.5 that displays the best performance. Dehydroxylation of W-OH groups requires higher temperatures, since the intensity of the band at 3674 cm⁻¹ barely decreases at reaction temperature (Figure 4.8 b, Figures S4.6-S4.9).

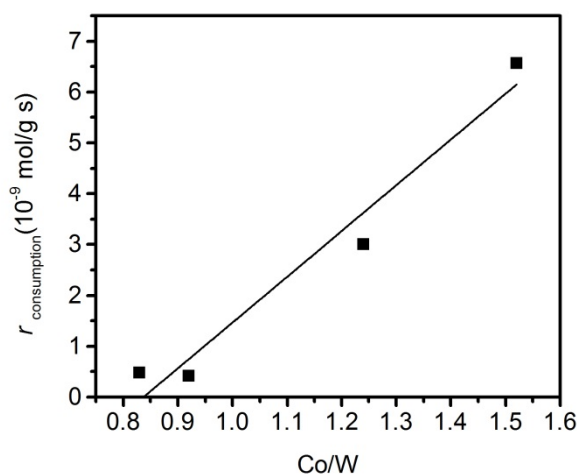


Figure 4.7 Steady state propane consumption rate as a function of Co/W ratio in the near surface region determined by XPS.

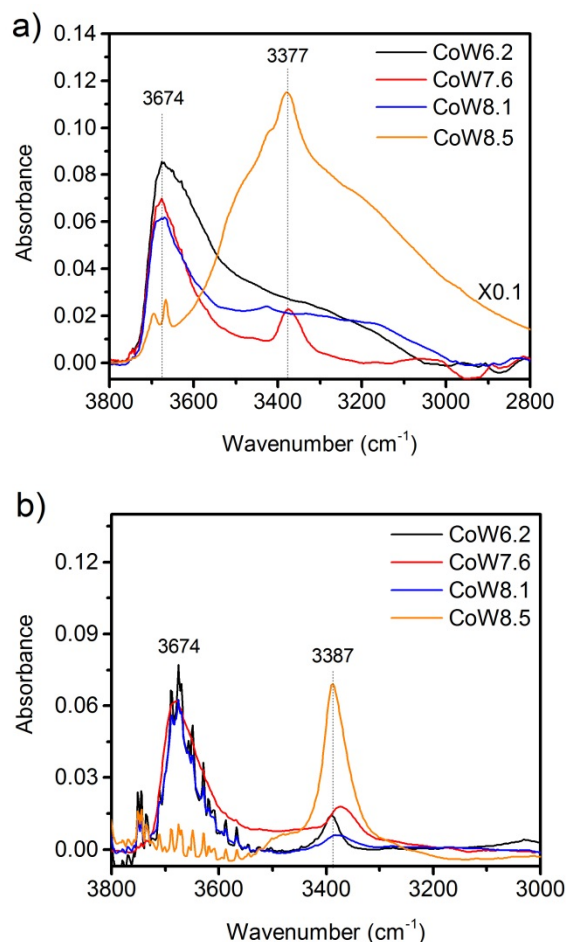


Figure 4.8 FT-IR spectra of CoWO₄ catalysts in He flow at a) room temperature and b) 400°C.

The effects of varying concentrations of propane, oxygen and water on the formation rate of propene, carbon monoxide and carbon dioxide were determined on m-WO₃, CoW6.2 and CoW8.5 catalysts. On the m-WO₃ catalyst (Figure S4.10), the propene formation rate increases almost linearly with increasing propane partial pressure, but only slightly with increasing oxygen partial pressure, and decreases with increasing water partial pressure. On the CoW6.2 catalyst (Figure 4.9), the propene formation rate increases almost linearly with increasing propane partial pressure, whereas the carbon oxides formation rates increase to a lesser extent with increasing propane partial pressure. The increasing oxygen partial pressure leads to unchanged propene formation rate but higher carbon dioxide and carbon monoxide formation rates. On the CoW8.5 catalyst (Figure S 4.10), the propene and carbon oxide formation rates increase almost to the same extent with increasing propane partial pressure. With increasing oxygen partial pressure, the propene formation rate decreases whereas the carbon oxides formation rates increase. Propene and carbon dioxide formation rates decrease with

increasing water partial pressure. The influence of water on carbon monoxide formation rates is very weak.

Some general trends can be noted from this preliminary study. Increasing partial pressure of oxygen is detrimental to the propene selectivity on all three studied catalysts indicating that oxygen activation is crucial in terms of selectivity. Increasing water partial pressure is not beneficial for the selectivity to propene on CoW8.5.

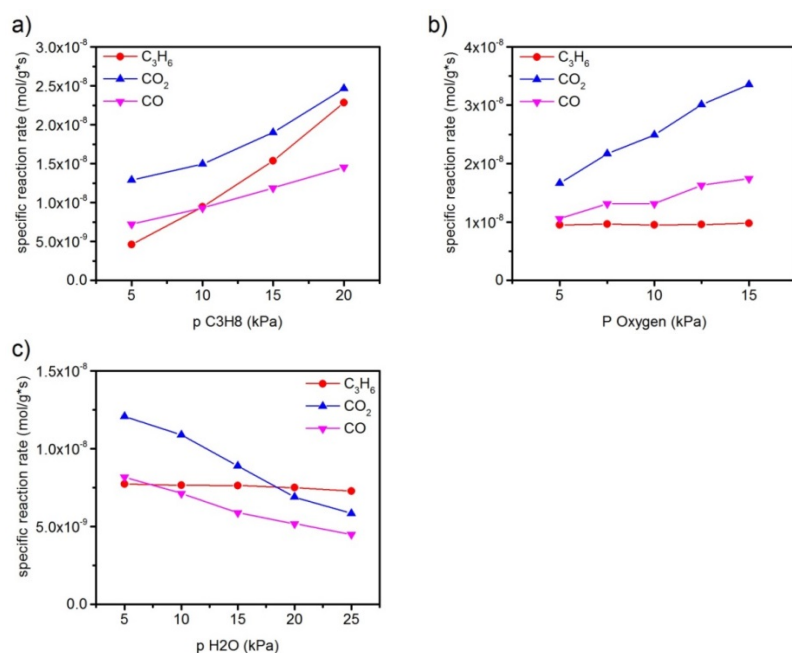


Figure 4.9 Influence of partial pressure of a) propane, b) oxygen and c) water on the specific product formation rate on CoW6.2 catalyst.

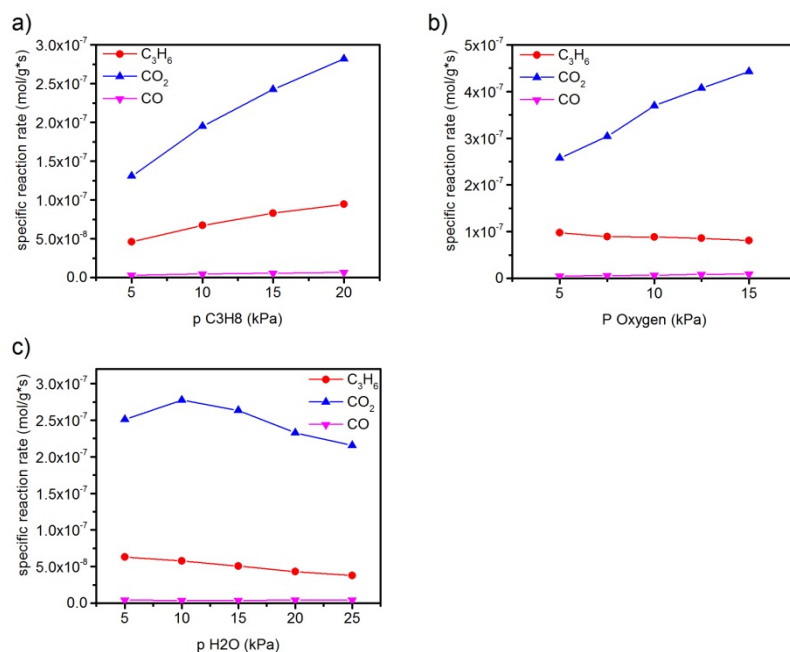


Figure 4.10 Influence of partial pressure of a) propane, b) oxygen and c) water on the specific product formation rate on CoW8.5 catalyst.

Table 4.3 Apparent reaction orders with respect to propane, oxygen and water on tungsten containing catalysts.

Apparent reaction order with respect to	m-WO ₃			CoW6.2			CoW8.5		
	p C ₃ H ₈	p O ₂	p H ₂ O	p C ₃ H ₈	p O ₂	p H ₂ O	p C ₃ H ₈	p O ₂	p H ₂ O
C ₃ H ₈ Consumption	0.78	0.11	-0.31 ^a	0.82	0.32	-0.18	0.54	0.22	-0.18

^a: in this study, only C₃H₆ is detected in reaction products

4.3 Conclusions

The size, shape and the surface termination of the cobalt tungstates can be controlled by the pH value in the solution before the hydrothermal synthesis. The Co/W ratio in the near surface region of the nanostructured CoWO₄ catalysts increases monotonically as determined by XPS analysis with the increasing initial pH. Nanostructuring of the cobalt tungstate enables the propane activation at a

temperature as low as 400°C, whereas the cobalt tungstate prepared by precipitation requires a much higher temperature as 560°C for C-H activation in propane. [10] In analogy to the nanostructured MnWO₄ synthesized at pH 9.9,[104] high resolution TEM and FT-IR spectroscopic analysis suggests surface termination by Co-O(H)-Co chain structures on the (010) facets. Site isolation of the very active Co atoms on a nanostructured crystalline CoWO₄ might be responsible for the improvement of the selectivity to propene in the ODP reaction, because the bulk Co₃O₄ is very active but non-selective to propene. As has been illustrated in this study, such site isolated one dimensional chains consisted of redox active transition metals on the surface termination layer might serve as a paradigm for the construction of the active sites for selective propane activation.

4.4 Experimental details:

4.4.1 Synthesis of the catalysts

The hydrothermal synthesis of CoWO₄ was performed in an analytical autoclave HPM-PT-040 (Premex Reactor GmbH). For the synthesis of CoWO₄, in the first step, a 0.2 M aqueous solution of Co(NO₃)₂ (Co(NO₃)₂·6H₂O, 99+%, Acros Organics) was added to a 0.2 M aqueous solution of Na₂WO₄ (Na₂WO₄·2H₂O, 99%, Sigma Aldrich) while stirring leading to a mixed solution of pH=7.6. Subsequently, the pH of the mixed solution was adjusted to 6.2, 7.9, 8.1 and 8.5 by adding 27.1 g of 1 M HNO₃ (HNO₃, 64-66%, Sigma Aldrich) or 6.2 and 13.1 g 1 M NaOH (NaOH, 98%, Alfa Aesar), respectively. After the first step for both metal tungstates, the mixtures were transferred to the autoclave and the temperature was raised from 20°C to 180°C at a rate of 5 °C/min. The synthesis temperature was kept at 180°C for 12 h. After cooling down the gel at a rate of 5 °C/min, the products of hydrothermal synthesis were filtered by centrifugation and washed twice with de-ionized water (MilliPore®). In the final step, the solids were dried in a muffle furnace in air at 80°C for 12 h. The solids were annealed in Argon (flow rate: 50 mL/min) at 400°C (heating rate 5 °C/min) for 2 h using a rotary tube furnace (XERION). The catalysts are called CoW_{x.x}, whereas x.x corresponds to the pH value before the hydrothermal synthesis.

The synthesis of mesoporous WO₃ is described elsewhere. Co₃O₄ (Aldrich, 99.995%) was used as obtained.

4.4.2 Catalyst characterization

High resolution TEM (HRTEM) and high resolution high angle annular dark field scanning transmission electron microscopy (HAADF-STEM) were performed on a double corrected JEOL JEM-ARM200F equipped with CEOS CESCOR, and CEOS CETCOR hexapole aberration correctors for probe and image forming lenses, respectively, and a cold field emission gun (CFEG). The acceleration voltage was set to 200 kV. TEM catalysts were prepared by drop deposition from

ethanolic suspensions onto lacey-carbon coated Cu grids. Field emission scanning electron microscopy (FESEM) was carried out with a Hitachi S4800 instrument operating at 5 kV.

The X-ray diffraction (XRD) measurement was performed in Bragg-Brentano geometry on a Bruker AXS D8 Advance theta/theta diffractometer, using Ni filtered Cu K α radiation and a position sensitive LynxEye silicon strip detector. The sample powder was filled into the recess of a cup-shaped sample holder, the surface of the powder bed being flush with the sample holder edge (front loading). The XRD data were evaluated by whole powder pattern fitting according to the Rietveld method as implemented in the TOPAS software [version 4.2, copyright 1999-2009 Bruker AXS].

X-ray photoelectron spectra were recorded at room temperature, using non-monochromatized Al K α (1486.6 eV) excitation and a hemispherical analyzer (Phoibos 150, SPECS). The binding energy scale was calibrated by the standard Au4f(7/2) and Cu2p(3/2) procedure. Theoretical cross sections from references were used to calculate the elemental composition.

The catalytic tests were carried out using a setup for partial oxidation (Integrated Lab Solutions) with 8 fixed bed quartz reactors (6 mm inner diameter) in parallel. Each reactor was equipped with a thermocouple for measuring the temperature inside the catalyst bed containing 20-300 mg of catalyst previously sieved to a particle size of 250-355 μ m and the catalytic performances were determined at atmospheric pressure. The reactant feed, which comprised C₃H₈, O₂, and N₂ as diluent, was passed through the reactors at a flow rate of 7.5-20 mL/min. The gas composition was 10 % C₃H₈, 5 % O₂ and 85% N₂. The product (and bypass) gas mixtures were analyzed by an online gas chromatograph (Agilent 7890). A system of Plot-Q and Plot-molsieve columns connected to a thermal conductivity detector (TCD) separated the permanent gases CO, CO₂, N₂, O₂, and CH₄. A system of a FFAP and a Plot-Q columns connected to a flame ionization detector (FID) allowed the separation of C₂-C₃ hydrocarbons and oxygenates.

4.5 Supporting information

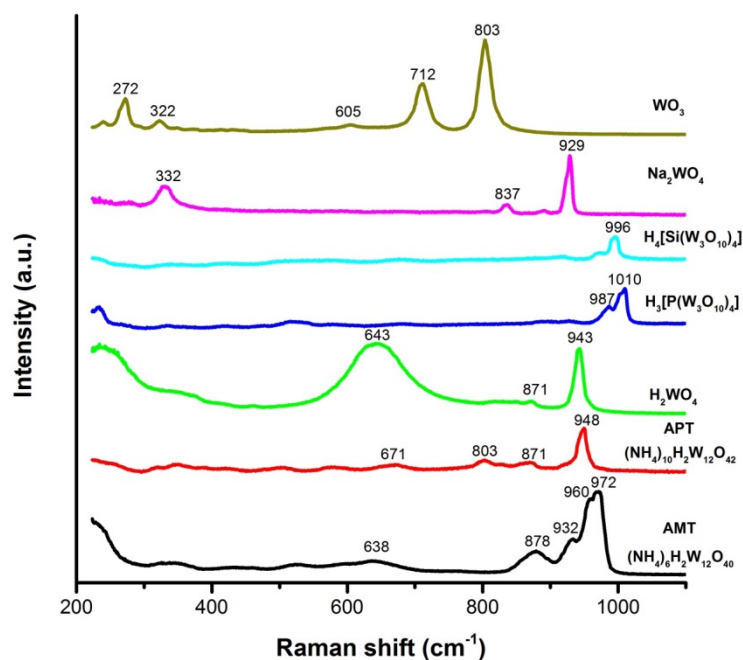


Figure S 4.1 Raman spectra of tungsten containing compounds measured as solids using 633 cm⁻¹ excitation wavelength.

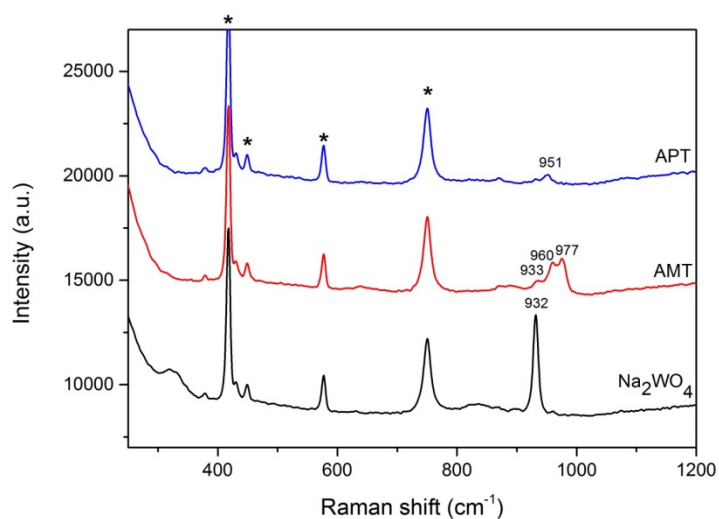


Figure S 4.2 Raman spectra of ammonium paratungstate (APT), ammonium metatungstate (AMT) and sodium tungstate in aqueous solution at room temperature. Bands denoted with asterisks belong to the sapphire window of the Raman probe.

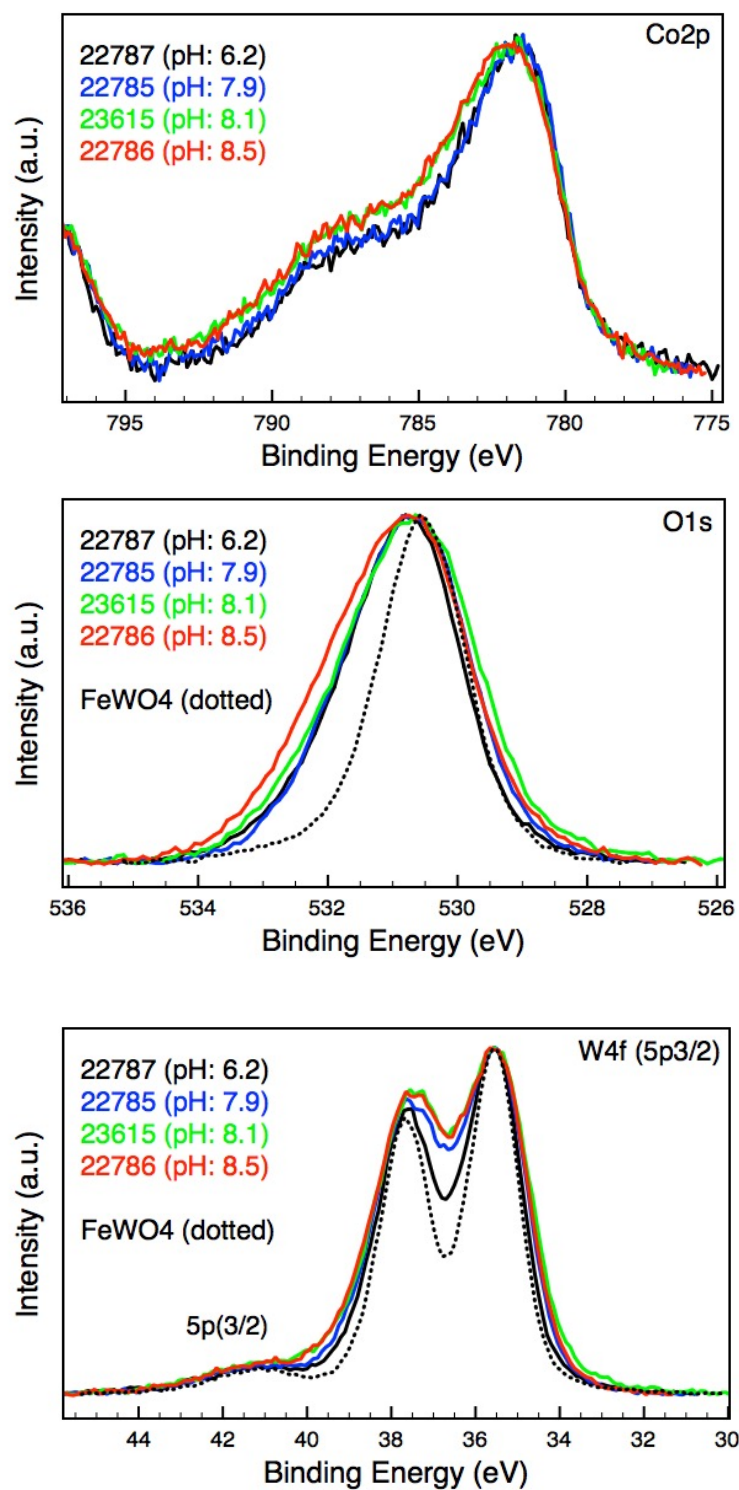


Figure S 4.3 Co2p(3/2), O1s and W4f (and 5p3/2) core level XPS spectra of the CoWO₄ samples after Shirley background subtraction and charging correction.

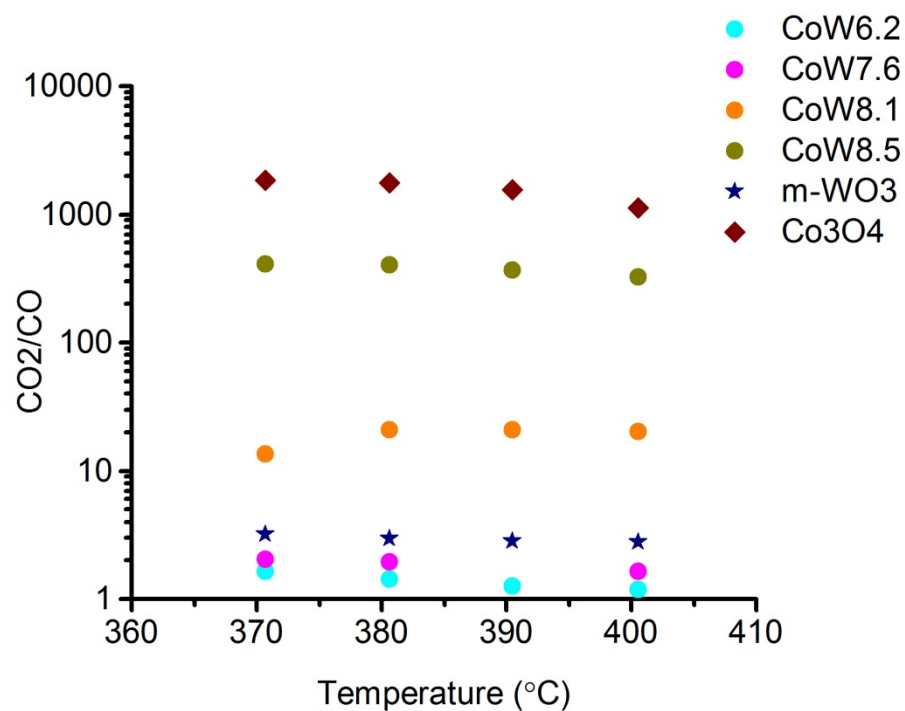


Figure S 4.4 CO₂/CO ratio in the ODP reaction over m-WO₃, Co₃O₄ and CoWO₄ catalysts. W/F=1.8-2.4 g s mL⁻¹ in the oxidative dehydrogenation of propane in a C₃H₈/O₂/N₂ feed (10:5:85).

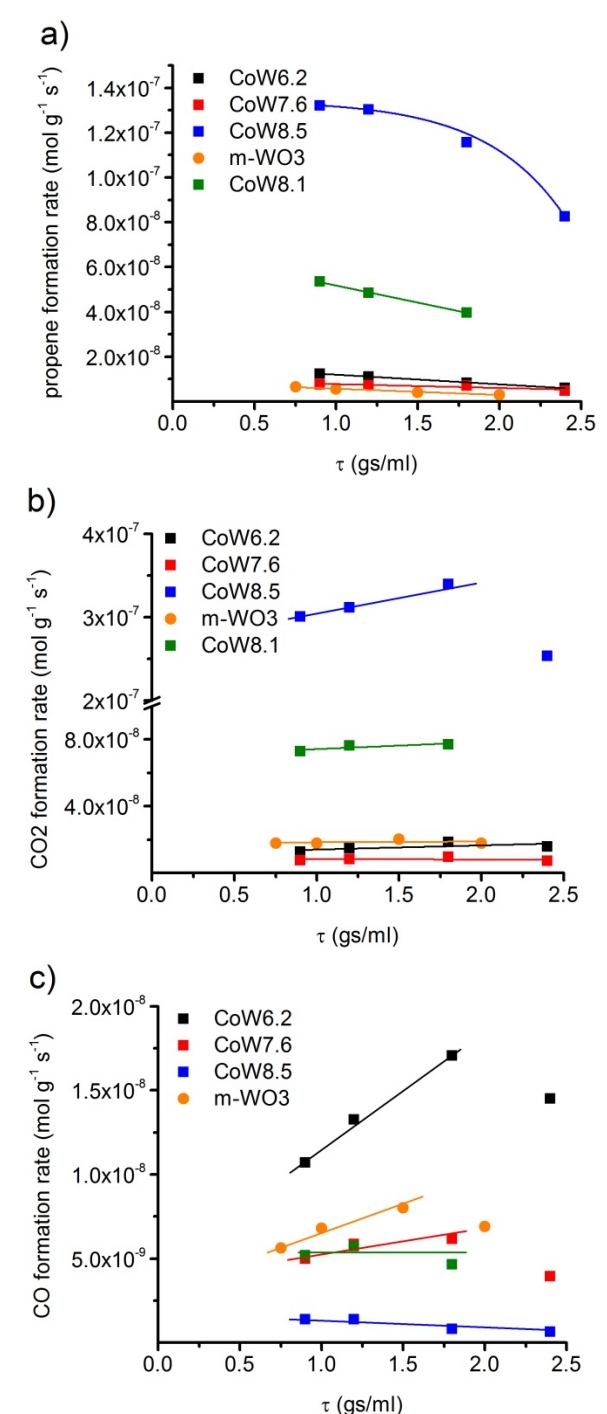


Figure S 4.5 a) Propene formation, b) CO₂ formation and c) CO formation rates over m-WO₃ and CoWO₄ catalysts. W/F=0.75-2.4 g s mL⁻¹ in the oxidative dehydrogenation of propane in a C₃H₈/O₂/N₂ feed (10:5:85).

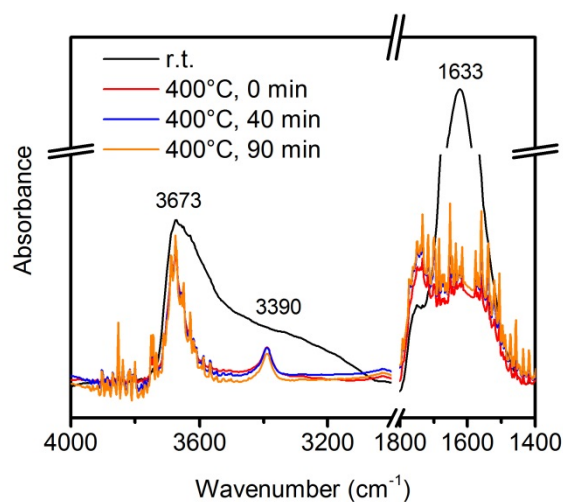


Figure S 4.6 FT-IR spectra of CoW_{6.2} catalyst in He flow.

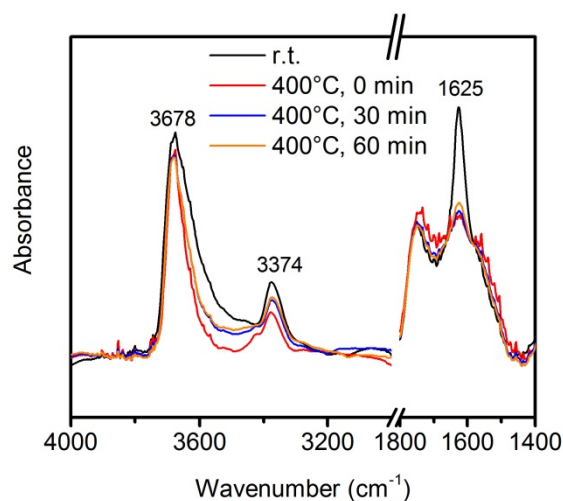


Figure S 4.7 FT-IR spectra of CoW_{7.6} catalyst in He flow.

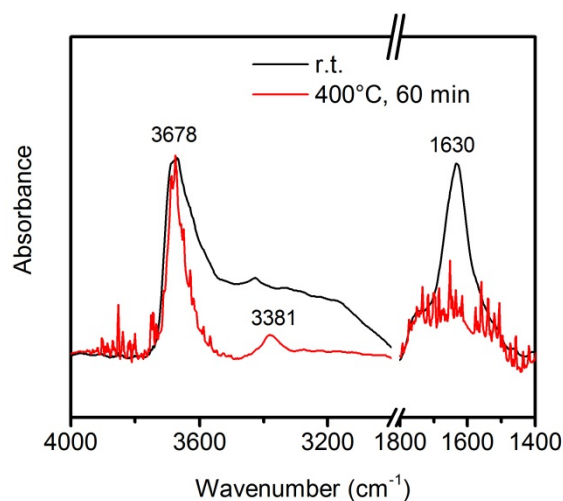


Figure S 4.8 FT-IR spectra of CoW_{8.1} catalyst in He flow.

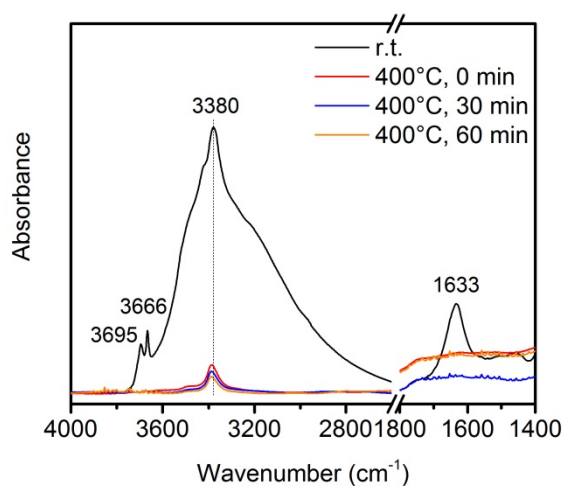


Figure S 4.9 FT-IR spectra of CoW_{8.5} catalyst in He flow.

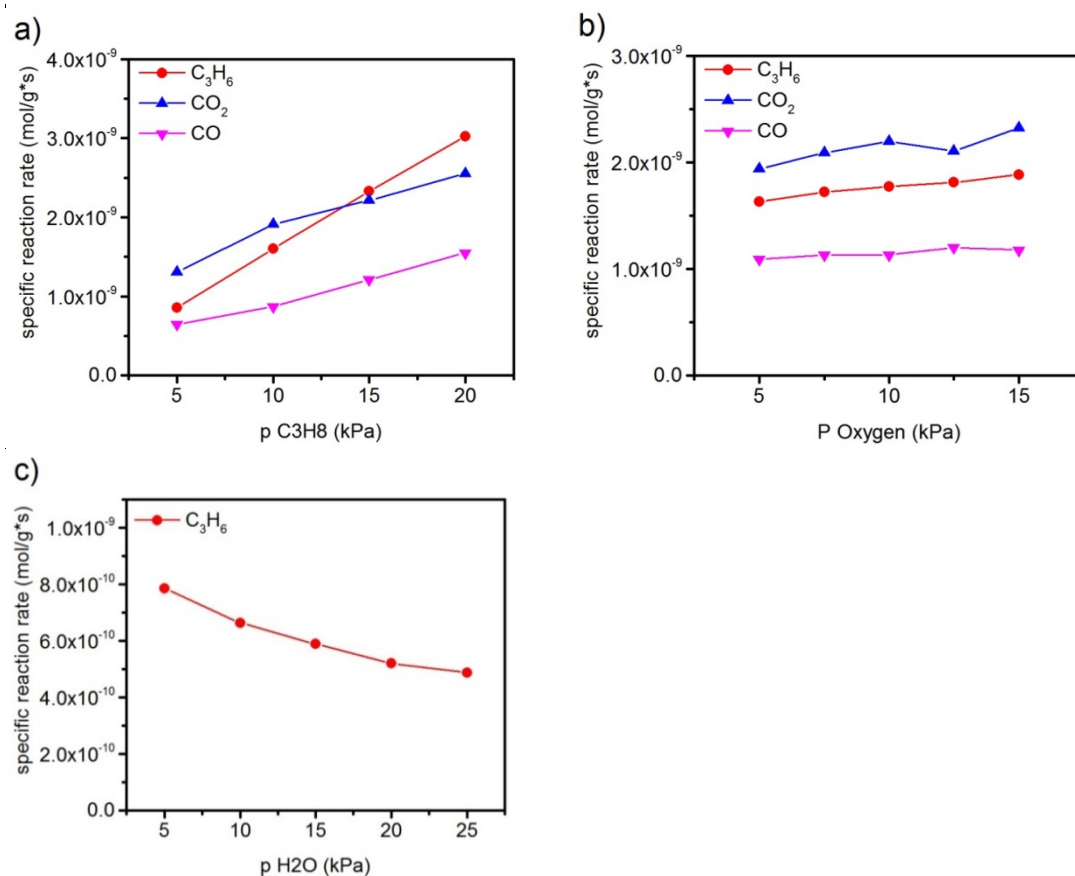


Figure S 4.10 Influence of partial pressure of a) propane, b) oxygen and c) water on the specific product formation rate on m-WO₃ catalyst.

5 Conclusions

In the present work, hydrothermally synthesized, nanostructured metal tungstates were investigated in the oxidative activation of lower alkanes. The issue of structure-reactivity relationship in oxidative dehydrogenation of propane (ODP) over metal tungstate catalysts was addressed.

Rod-shaped nanostructured MnWO₄ was found to be a new class of material, which can relatively selectively activate propane at moderate temperature. By comprehensive and complementary structural characterization, a two-dimensional manganese chain structure was observed to be the surface-terminating layer on (010) crystal planes. In situ analysis during the hydrothermal synthesis suggests the formation of this unique Mn surface structure by dissolution of WO_x in the alkaline solution during aging. The outmost chain is composed of -Mn-(OH)₂-Mn-. A redox type reaction is indicated. Mn in the aforementioned chain structure might be the electron acceptor. "Site isolation" of the active Mn chains might explain why a Mn-based oxide turns from a combustion catalyst into a relatively selective oxidation catalyst.

Hydrothermal synthesis enables to achieve a family of nanostructured CoWO₄ catalysts with varying shape and surface termination. And they were also found to be highly active in ODP reaction. CoWO₄ synthesized applying an initial pH of 8.5 shows the highest activity and selectivity, and this specific catalyst shows superior performance than the MnWO₄ catalyst. Dehydroxylation occurs at elevated temperature and formation of the Co-O-Co site is expected to happen in the oxygen containing gas feed. Kinetic investigation and structural characterizations suggest surface oxygen species in the "-Co-O-Co-" chains to be the active sites for C-H activation in propane activation.

Generally, on the CoWO₄ catalysts, higher oxygen concentration in the reaction feed leads to higher selectivity to CO_x, which suggests a crucial role of oxygen activation. The control of oxygen activation might be the major challenge in the activation of propane since it is related to the consecutive combustion of propene. An alternate feeding of propane and oxygen, which minimizes the contact of propane with the unselective oxygen species, is likely to improve the overall selectivity to propene.

In the supplementary experiments (results were not shown in the thesis) for the MnWO₄ catalysts, the influence of shape and surface structure in ODP over nanostructured MnWO₄ was investigated. Kinetic studies reveal a strong dependence of propane consumption rate on the initial pH of the hydrothermal syntheses of the phase-pure catalysts. Catalyst synthesized with highest initial pH shows very good long term stability, whereas the ones synthesized with lower initial pH endure severe deactivation. Thorough structural characterization was conducted over the series of catalysts. (010) planes were found to be partially terminated by manganese atoms in the form of chain structure by

transmission electron microscopy. Raman and IR spectroscopy resolve the manganese oxyhydroxide surface structure. In situ IR spectroscopy demonstrates reversible dehydroxylation and hydroxylation at high and low temperature, respectively. Gas phase ethanol oxidation probe reaction suggests a redox type activation of propane. The abundance of the near-surface Mn determined by X-ray photoelectron spectroscopy correlates to the initial propane consumption rate.

In another set of supplementary experiments (results not shown in the thesis), in situ UV-Vis and FT-IR spectroscopy has been applied for estimating the oxidation degree of the surface layer on a series of MnWO₄ catalysts in the ODP reaction. And time resolved analysis enables to derive the kinetic parameters of reoxidation of the surface layer. The quantitative kinetic study reveals a correlation between the initial reoxidation rate constant and the apparent propene formation rate, suggesting the important role of the reoxidation step of the catalyst. In oxygen partial pressure variation experiment on one MnWO₄ catalyst, increasing oxidation degree of the surface layer was found to accelerate the propane consumption rate. This indicates the catalytic relevancy of the surface structural oxygen species in propene activation. In situ FT-IR spectroscopy observes an increasing amount of hydroxyl groups on the catalyst when switching from inert to reaction gas atmosphere. This hints the transformation of the nucleophilic surface structural oxygen species into hydroxyl groups by hydrogen abstraction from propane.

The work elucidates the importance of segregated termination layers on the surface of bulk mixed metal oxides applied as catalysts in alkane oxidation. It is demonstrated that surface termination can be established not only under reaction conditions [1, 42-45, 67], but also during synthesis under specific hydrothermal conditions. The developed synthesis method might stimulate further synthetic work resulting in the discovery of new catalytic materials.

6 Bibliography

- [1] A.C. Sanfiz, T.W. Hansen, D. Teschner, P. Schno, F. Girgsdies, A. Trunschke, R. Schlo, M.H. Looi, S. Bee, A. Hamid, Dynamics of the MoVTenNb Oxide M1 Phase in Propane Oxidation, *J. Phys. Chem. C*, 114 (2010) 1912-1921.
- [2] F. Cavani, Catalytic selective oxidation: The forefront in the challenge for a more sustainable chemical industry, *Catal. Today*, 157 (2010) 8-15.
- [3] G. Centi, F. Trifiro, J.R. Ebner, V.M. Franchetti, Mechanistic aspects of maleic anhydride synthesis from C₄ hydrocarbons over phosphorus vanadium oxide, *Chem. Rev.*, 88 (1988) 55-80.
- [4] J.J.H.B. Sattler, A.M. Beale, B.M. Weckhuysen, Operando Raman spectroscopy study on the deactivation of Pt/Al₂O₃ and Pt-Sn/Al₂O₃ propane dehydrogenation catalysts, *Physical Chemistry Chemical Physics*, 15 (2013) 12095-12103.
- [5] W. Qi, D. Su, Metal-Free Carbon Catalysts for Oxidative Dehydrogenation Reactions, *ACS Catalysis*, 4 (2014) 3212-3218.
- [6] R. Schlögl, Active Sites for Propane Oxidation: Some Generic Considerations, *Top. Catal.*, 54 (2011) 627-638.
- [7] C.A. Carrero, R. Schloegl, I.E. Wachs, R. Schomaecker, Critical Literature Review of the Kinetics for the Oxidative Dehydrogenation of Propane over Well-Defined Supported Vanadium Oxide Catalysts, *ACS Catalysis*, 4 (2014) 3357-3380.
- [8] D.L. Stern, R.K. Grasselli, Propane Oxydehydrogenation over Molybdate-Based Catalysts, *J. Catal.*, 167 (1997) 550-559.
- [9] D.L. Stern, R.K. Grasselli, Reaction Network and Kinetics of Propane Oxydehydrogenation over Nickel Cobalt Molybdate, *J. Catal.*, 167 (1997) 560-569.
- [10] D.L. Stern, R.K. Grasselli, Propane Oxydehydrogenation over Metal Tungstates, *J. Catal.*, 167 (1997) 570-572.
- [11] K. Chen, A.T. Bell, E. Iglesia, Kinetics and Mechanism of Oxidative Dehydrogenation of Propane on Vanadium, Molybdenum, and Tungsten Oxides, *J. Phys. Chem. A*, 104 (2000) 1292-1299.
- [12] A. Khodakov, J. Yang, S. Su, E. Iglesia, A.T. Bell, Structure and properties of vanadium oxide-zirconia catalysts for propane oxidative dehydrogenation, *J. Catal.*, 177 (1998) 343-351.
- [13] K. Chen, A. Khodakov, J. Yang, A.T. Bell, E. Iglesia, Isotopic Tracer and Kinetic Studies of Oxidative Dehydrogenation Pathways on Vanadium Oxide Catalysts, *J. Catal.*, 186 (1999) 325-333.
- [14] J.N. Michaels, D.L. Stern, R.K. Grasselli, Oxydehydrogenation of propane over Mg-V-Sb-oxide catalysts. I. Reaction network, *Catal. Lett.*, 42 135-137.
- [15] J.N. Michaels, D.L. Stern, R.K. Grasselli, Oxydehydrogenation of propane over Mg-V-Sb-oxide catalysts. II. Reaction kinetics and mechanism, *Catal. Lett.*, 42 139-148.
- [16] R. Grabowski, Kinetics of Oxidative Dehydrogenation of C₂ - C₃ Alkanes on Oxide Catalysts, *Catalysis Reviews*, 48 (2006) 199-268.
- [17] A. Khodakov, B. Olthof, A.T. Bell, E. Iglesia, Structure and Catalytic Properties of Supported Vanadium Oxides: Support Effects on Oxidative Dehydrogenation Reactions, *J. Catal.*, 181 (1999) 205-216.

- [18] M.D. Argyle, K. Chen, C. Resini, C. Krebs, A.T. Bell, E. Iglesia, In situ UV-visible assessment of extent of reduction during oxidation reactions on oxide catalysts, *Chem. Commun.*, (2003) 2082-2083.
- [19] M.D. Argyle, K. Chen, C. Resini, C. Krebs, A.T. Bell, E. Iglesia, Extent of Reduction of Vanadium Oxides during Catalytic Oxidation of Alkanes Measured by in-Situ UV-Visible Spectroscopy, *J. Phys. Chem. A*, 108 (2004) 2345-2353.
- [20] M.D. Argyle, K. Chen, E. Iglesia, A.T. Bell, In situ UV-Visible Spectroscopic Measurements of Kinetic Parameters and Active Sites for Catalytic Oxidation of Alkanes on Vanadium Oxides†, *J. Phys. Chem. A*, 109 (2005) 2414-2420.
- [21] O. Ovsitser, M. Cherian, A. Brückner, E.V. Kondratenko, Dynamics of redox behavior of nano-sized VO_x species over Ti-Si-MCM-41 from time-resolved in situ UV/Vis analysis, *J. Catal.*, 265 (2009) 8-18.
- [22] R. Schlögl, Heterogeneous Catalysis, *Angew. Chem. Int. Ed.*, 54 (2015) 3465-3520.
- [23] I.E. Wachs, B.M. Weckhuysen, Structure and reactivity of surface vanadium oxide species on oxide supports, *Applied Catalysis A: General*, 157 (1997) 67-90.
- [24] B. Solsona, J.M. López Nieto, P. Concepción, A. Dejoz, F. Ivars, M.I. Vázquez, Oxidative dehydrogenation of ethane over Ni-W-O mixed metal oxide catalysts, *J. Catal.*, 280 (2011) 28-39.
- [25] R.K. Grasselli, Advances and future trends in selective oxidation and ammoxidation catalysis, *Catal. Today*, 49 (1999) 141-153.
- [26] R. Grasselli, Fundamental Principles of Selective Heterogeneous Oxidation Catalysis, *Top. Catal.*, 21 (2002) 79-88.
- [27] Y. Xia, Y. Xiong, B. Lim, S.E. Skrabalak, Shape-Controlled Synthesis of Metal Nanocrystals: Simple Chemistry Meets Complex Physics?, *Angew. Chem. Int. Ed.*, 48 (2009) 60-103.
- [28] K. Zhou, Y. Li, Catalysis Based on Nanocrystals with Well-Defined Facets, *Angew. Chem. Int. Ed.*, 51 (2012) 602-613.
- [29] Y. Li, W. Shen, Morphology-dependent nanocatalysts: Rod-shaped oxides, *Chem. Soc. Rev.*, 43 (2014) 1543-1574.
- [30] L. Hu, Q. Peng, Y. Li, Selective Synthesis of Co₃O₄ Nanocrystal with Different Shape and Crystal Plane Effect on Catalytic Property for Methane Combustion, *JACS*, 130 (2008) 16136-16137.
- [31] X. Xie, Y. Li, Z.-Q. Liu, M. Haruta, W. Shen, Low-temperature oxidation of CO catalysed by Co₃O₄ nanorods, *Nature*, 458 (2009) 746-749.
- [32] H.-X. Mai, L.-D. Sun, Y.-W. Zhang, R. Si, W. Feng, H.-P. Zhang, H.-C. Liu, C.-H. Yan, Shape-Selective Synthesis and Oxygen Storage Behavior of Ceria Nanopolyhedra, Nanorods, and Nanocubes, *J. Phys. Chem. A*, 109 (2005) 24380-24385.
- [33] K. Zhou, X. Wang, X. Sun, Q. Peng, Y. Li, Enhanced catalytic activity of ceria nanorods from well-defined reactive crystal planes, *J. Catal.*, 229 (2005) 206-212.
- [34] Z. Wu, M. Li, S.H. Overbury, On the structure dependence of CO oxidation over CeO₂ nanocrystals with well-defined surface planes, *J. Catal.*, 285 (2012) 61-73.
- [35] Q. Hua, T. Cao, X.-K. Gu, J. Lu, Z. Jiang, X. Pan, L. Luo, W.-X. Li, W. Huang, Crystal-Plane-Controlled Selectivity of Cu₂O Catalysts in Propylene Oxidation with Molecular Oxygen, *Angew. Chem. Int. Ed.*, 53 (2014) 4856-4861.

- [36] P. Schwach, W. Frandsen, M.-G. Willinger, R. Schlögl, A. Trunschke, Structure sensitivity of the oxidative activation of methane over MgO model catalysts: I. Kinetic study, *J. Catal.*, 329 (2015) 560-573.
- [37] P. Schwach, N. Hamilton, M. Eichelbaum, L. Thum, T. Lunkenbein, R. Schlögl, A. Trunschke, Structure sensitivity of the oxidative activation of methane over MgO model catalysts: II. Nature of active sites and reaction mechanism, *J. Catal.*, 329 (2015) 574-587.
- [38] Y. Lin, Z. Wu, J. Wen, K.R. Poeppelmeier, L.D. Marks, Imaging the Atomic Surface Structures of CeO₂ Nanoparticles, *Nano Lett.*, 14 (2013) 191-196.
- [39] X. Liu, K. Zhou, L. Wang, B. Wang, Y. Li, Oxygen Vacancy Clusters Promoting Reducibility and Activity of Ceria Nanorods, *JACS*, 131 (2009) 3140-3141.
- [40] Z. Wu, M. Li, J. Howe, H.M. Meyer, S.H. Overbury, Probing Defect Sites on CeO₂ Nanocrystals with Well-Defined Surface Planes by Raman Spectroscopy and O₂ Adsorption†, *Langmuir*, 26 (2010) 16595-16606.
- [41] J. Paier, C. Penshke, J. Sauer, Oxygen Defects and Surface Chemistry of Ceria: Quantum Chemical Studies Compared to Experiment, *Chem. Rev.*, 113 (2013) 3949-3985.
- [42] M. Hävecker, S. Wrabetz, J. Kröhnert, L.-I. Csepei, R. Naumann d'Alnoncourt, Y.V. Kolen'ko, F. Girgsdies, R. Schlögl, A. Trunschke, Surface chemistry of phase-pure M1 MoVTenb oxide during operation in selective oxidation of propane to acrylic acid, *J. Catal.*, 285 (2012) 48-60.
- [43] M. Hävecker, R.W. Mayer, A. Knop-Gericke, H. Bluhm, E. Kleimenov, A. Liskowski, D. Su, R. Follath, F.G. Requejo, D.F. Ogletree, M. Salmeron, J.A. Lopez-Sanchez, J.K. Bartley, G.J. Hutchings, R. Schlögl, In Situ Investigation of the Nature of the Active Surface of a Vanadyl Pyrophosphate Catalyst during n-Butane Oxidation to Maleic Anhydride, *J. Phys. Chem. A*, 107 (2003) 4587-4596.
- [44] M. Hävecker, A. Knop-Gericke, H. Bluhm, E. Kleimenov, R.W. Mayer, M. Fait, R. Schlögl, Dynamic surface behaviour of VPO catalysts under reactive and non-reactive gas compositions: an in situ XAS study, *Appl. Surf. Sci.*, 230 (2004) 272-282.
- [45] E. Kleimenov, H. Bluhm, M. Hävecker, A. Knop-Gericke, A. Pestryakov, D. Teschner, J.A. Lopez-Sanchez, J.K. Bartley, G.J. Hutchings, R. Schlögl, XPS investigations of VPO catalysts under reaction conditions, *Surf. Sci.*, 575 (2005) 181-188.
- [46] W. Zhang, A. Trunschke, R. Schlögl, D. Su, Real-Space Observation of Surface Termination of a Complex Metal Oxide Catalyst, *Angew. Chem. Int. Ed.*, 49 (2010) 6084-6089.
- [47] X. Zhang, Y. Zhou, L. Ma, X.-J. Wang, T. Ejima, T. Banse, H. Takatsuka, Y. Kondo, M. Ishino, N. Kimura, M. Watanabe, I. Matsubara, Microscopic optical and photoelectron measurements of MWO₄ (M=Mn, Fe, and Ni), *J. Lumin.*, 119 (2006) 59-63.
- [48] J. Ruiz-Fuertes, S. López-Moreno, J. López-Solano, D. Errandonea, A. Segura, R. Lacomba-Perales, A. Muñoz, S. Radescu, P. Rodríguez-Hernández, M. Gospodinov, L.L. Nagornaya, C.Y. Tu, Pressure effects on the electronic and optical properties of AWO₄ wolframites (A = Cd, Mg, Mn, and Zn): The distinctive behavior of multiferroic MnWO₄, *Phys. Rev. B*, 86 (2012) 125202.
- [49] M.N. Iliev, M.M. Gospodinov, A.P. Litvinchuk, Raman spectroscopy of MnWO₄, *Phys. Rev. B*, 80 (2009) 212302.
- [50] L.H. Hoang, N.T.M. Hien, W.S. Choi, Y.S. Lee, K. Taniguchi, T. Arima, S. Yoon, X.B. Chen, I.-S. Yang, Temperature-dependent Raman scattering study of multiferroic MnWO₄, *Journal of Raman Spectroscopy*, 41 (2010) 1005-1010.

- [51] W.S. Choi, K. Taniguchi, S.J. Moon, S.S.A. Seo, T. Arima, H. Hoang, I.-S. Yang, T.W. Noh, Y.S. Lee, Electronic structure and anomalous band-edge absorption feature in multiferroic MnWO₄: An optical spectroscopic study, *Phys. Rev. B*, 81 (2010) 205111.
- [52] S. Dey, R.A. Ricciardo, H.L. Cuthbert, P.M. Woodward, Metal-to-Metal Charge Transfer in AWO₄ (A = Mg, Mn, Co, Ni, Cu, or Zn) Compounds with the Wolframite Structure, *Inorg. Chem.*, 53 (2014) 4394-4399.
- [53] L.-G. Cai, F.-M. Liu, D. Zhang, W.-W. Zhong, Dependence of optical properties of monoclinic MnWO₄ on the electric field of incident light, *Physica B: Condensed Matter*, 407 (2012) 3654-3659.
- [54] R. Bharati, R.A. Singh, B.M. Wanklyn, Electrical conduction in manganese tungstate, *J. Phys. Chem. Solids*, 43 (1982) 641-644.
- [55] W. Qu, W. Wlodarski, J.-U. Meyer, Comparative study on micromorphology and humidity sensitive properties of thin-film and thick-film humidity sensors based on semiconducting MnWO₄, *Sensors and Actuators B: Chemical*, 64 (2000) 76-82.
- [56] C. Tian, C. Lee, H. Xiang, Y. Zhang, C. Payen, S. Jobic, M.-H. Whangbo, Magnetic structure and ferroelectric polarization of MnWO₄ investigated by density functional calculations and classical spin analysis, *Phys. Rev. B*, 80 (2009) 104426.
- [57] N. Hollmann, Z. Hu, T. Willers, L. Bohatý, P. Becker, A. Tanaka, H.H. Hsieh, H.J. Lin, C.T. Chen, L.H. Tjeng, Local symmetry and magnetic anisotropy in multiferroic MnWO₄ and antiferromagnetic CoWO₄ studied by soft x-ray absorption spectroscopy, *Phys. Rev. B*, 82 (2010) 184429.
- [58] R. Schlögl, Active Sites for Propane Oxidation: Some Generic Considerations, *Topics in Catalysis*, 54 (2011) 627-638.
- [59] F. Cavani, N. Ballarini, A. Cericola, Oxidative dehydrogenation of ethane and propane: How far from commercial implementation?, *Catal. Today*, 127 (2007) 113-131.
- [60] K. Chen, E. Iglesia, A.T. Bell, Kinetic Isotopic Effects in Oxidative Dehydrogenation of Propane on Vanadium Oxide Catalysts, *J. Catal.*, 192 (2000) 197-203.
- [61] T. Blasco, J.M.L. Nieto, Oxidative dehydrogenation of short chain alkanes on supported vanadium oxide catalysts, *Applied Catalysis A: General*, 157 (1997) 117-142.
- [62] C. Hess, Nanostructured Vanadium Oxide Model Catalysts for Selective Oxidation Reactions, *ChemPhysChem*, 10 (2009) 319-326.
- [63] I.E. Wachs, Catalysis science of supported vanadium oxide catalysts, *Dalton Transactions*, 42 (2013) 11762-11769.
- [64] B.M. Weckhuysen, D.E. Keller, Chemistry, spectroscopy and the role of supported vanadium oxides in heterogeneous catalysis, *Catal. Today*, 78 (2003) 25-46.
- [65] M. Eichelbaum, R. Glaum, M. Hävecker, K. Wittich, C. Heine, H. Schwarz, C.-K. Dobner, C. Welker-Nieuwoudt, A. Trunschke, R. Schlögl, Towards Physical Descriptors of Active and Selective Catalysts for the Oxidation of n-Butane to Maleic Anhydride, *ChemCatChem*, 5 (2013) 2318-2329.
- [66] C. Heine, M. Hävecker, M. Sanchez-Sanchez, A. Trunschke, R. Schlögl, M. Eichelbaum, Work Function, Band Bending, and Microwave Conductivity Studies on the Selective Alkane Oxidation Catalyst MoVTaNb Oxide (Orthorhombic M1 Phase) under Operation Conditions, *J. Phys. Chem. C*, 117 (2013) 26988-26997.

- [67] C. Heine, M. Hävecker, E. Stotz, F. Rosowski, A. Knop-Gericke, A. Trunschke, M. Eichelbaum, R. Schlögl, Ambient-Pressure Soft X-ray Absorption Spectroscopy of a Catalyst Surface in Action: Closing the Pressure Gap in the Selective n-Butane Oxidation over Vanadyl Pyrophosphate, *J. Phys. Chem. C*, 118 (2014) 20405-20412.
- [68] M. Eichelbaum, M. Hävecker, C. Heine, A.M. Wernbacher, F. Rosowski, A. Trunschke, R. Schlögl, The Electronic Factor in Alkane Oxidation Catalysis, *Angew. Chem. Int. Ed.*, 54 (2015) 2922-2926.
- [69] C. Heine, M. Havecker, A. Trunschke, R. Schlogl, M. Eichelbaum, The impact of steam on the electronic structure of the selective propane oxidation catalyst MoVTenb oxide (orthorhombic M1 phase), *Phys. Chem. Chem. Phys.*, 17 (2015) 8983-8993.
- [70] S.-H. Yu, B. Liu, M.-S. Mo, J.-H. Huang, X.-M. Liu, Y.-T. Qian, General Synthesis of Single-Crystal Tungstate Nanorods/Nanowires: A Facile, Low-Temperature Solution Approach, *Adv. Funct. Mater.*, 13 (2003) 639-647.
- [71] F. Kapteijn, A.D. Vanlangeveld, J.A. Moulijn, A. Andreini, M.A. Vuurman, A.M. Turek, J.M. Jehng, I.E. Wachs, Alumina-Supported Manganese Oxide Catalysts: I. Characterization: Effect of Precursor and Loading, *J. Catal.*, 150 (1994) 94-104.
- [72] F. Buciuman, F. Patcas, R. Craciun, D. R. T. Zahn, Vibrational spectroscopy of bulk and supported manganese oxides, *Phys. Chem. Chem. Phys.*, 1 (1999) 185-190.
- [73] A.J. Nelson, J.G. Reynolds, J.W. Roos, Core-level satellites and outer core-level multiplet splitting in Mn model compounds, *Journal of Vacuum Science & Technology A*, 18 (2000) 1072-1076.
- [74] M.C. Biesinger, B.P. Payne, A.P. Grosvenor, L.W.M. Lau, A.R. Gerson, R.S.C. Smart, Resolving surface chemical states in XPS analysis of first row transition metals, oxides and hydroxides: Cr, Mn, Fe, Co and Ni, *Appl. Surf. Sci.*, 257 (2011) 2717-2730.
- [75] B. Gilbert, B.H. Frazer, A. Belz, P.G. Conrad, K.H. Nealson, D. Haskel, J.C. Lang, G. Srajer, G. De Stasio, Multiple Scattering Calculations of Bonding and X-ray Absorption Spectroscopy of Manganese Oxides, *J. Phys. Chem. A*, 107 (2003) 2839-2847.
- [76] R. Qiao, T. Chin, S.J. Harris, S. Yan, W. Yang, Spectroscopic fingerprints of valence and spin states in manganese oxides and fluorides, *Current Applied Physics*, 13 (2013) 544-548.
- [77] S.P. Cramer, F.M.F. DeGroot, Y. Ma, C.T. Chen, F. Sette, C.A. Kipke, D.M. Eichhorn, M.K. Chan, W.H. Armstrong, Ligand field strengths and oxidation states from manganese L-edge spectroscopy, *JACS*, 113 (1991) 7937-7940.
- [78] K.V. Shanavas, D. Choudhury, I. Dasgupta, S.M. Sharma, D.D. Sarma, Origin of ferroelectric polarization in spiral magnetic structure of MnWO₄, *Phys. Rev. B*, 81 (2010) 212406.
- [79] K. Amakawa, L. Sun, C. Guo, M. Hävecker, P. Kube, I.E. Wachs, S. Lwin, A.I. Frenkel, A. Patlolla, K. Hermann, R. Schlögl, A. Trunschke, How Strain Affects the Reactivity of Surface Metal Oxide Catalysts, *Angew. Chem. Int. Ed.*, 52 (2013) 13553-13557.
- [80] M. Sanchez Sanchez, F. Girgsdies, M. Jastak, P. Kube, R. Schlögl, A. Trunschke, Aiding the Self-Assembly of Supramolecular Polyoxometalates under Hydrothermal Conditions To Give Precursors of Complex Functional Oxides, *Angew. Chem. Int. Ed.*, 51 (2012) 7194-7197.
- [81] R. Schlögl, S.B. Abd Hamid, Nanocatalysis: Mature Science Revisited or Something Really New?, *Angewandte Chemie International Edition*, 43 (2004) 1628-1637.

- [82] A. Trunschke, Chapter 4 Propane-Selective Oxidation to Acrylic Acid, in: *Nanostructured Catalysts: Selective Oxidations*, The Royal Society of Chemistry, 2011, pp. 56-95.
- [83] P. Gruene, T. Wolfram, K. Pelzer, R. Schlögl, A. Trunschke, Role of dispersion of vanadia on SBA-15 in the oxidative dehydrogenation of propane, *Catal. Today*, 157 (2010) 137-142.
- [84] P. Stephens, Phenomenological model of anisotropic peak broadening in powder diffraction, *Journal of Applied Crystallography*, 32 (1999) 281-289.
- [85] A. Knop - Gericke, E. Kleimenov, M. Hävecker, R. Blume, D. Teschner, S. Zafeiratos, R. Schlögl, V.I. Bukhtiyarov, V.V. Kaichev, I.P. Prosvirin, A.I. Nizovskii, H. Bluhm, A. Barinov, P. Dudin, M. Kiskinova, Chapter 4 X - Ray Photoelectron Spectroscopy for Investigation of Heterogeneous Catalytic Processes, in: C.G. Bruce, K. Helmut (Eds.) *Advances in Catalysis*, Academic Press, 2009, pp. 213-272.
- [86] M. Salmeron, R. Schlögl, Ambient pressure photoelectron spectroscopy: A new tool for surface science and nanotechnology, *Surf. Sci. Rep.*, 63 (2008) 169-199.
- [87] I.E. Wachs, K. Routray, *Catalysis Science of Bulk Mixed Oxides*, ACS Catalysis, 2 (2012) 1235-1246.
- [88] E.W. McFarland, H. Metiu, *Catalysis by Doped Oxides*, Chemical Reviews, 113 (2013) 4391-4427.
- [89] W. Ueda, Establishment of Crystalline Complex Mo-V-Oxides as Selective Oxidation Catalysts, *Journal of the Japan Petroleum Institute*, 56 (2013) 122-132.
- [90] A. Trunschke, Synthesis of Solid Catalysts, in: R. Schlögl (Ed.) *Chemical Energy Storage*, Walter de Gruyter GmbH, Berlin/Boston, 2013, pp. 277-301.
- [91] K. Amakawa, Y.V. Kolen'ko, A. Villa, M.E. Schuster, L.-I. Csepei, G. Weinberg, S. Wrabetz, R. Naumann d'Alnoncourt, F. Girgsdies, L. Prati, R. Schlögl, A. Trunschke, Multifunctionality of Crystalline MoV(TeNb) M1 Oxide Catalysts in Selective Oxidation of Propane and Benzyl Alcohol, *ACS Catalysis*, 3 (2013) 1103-1113.
- [92] M. Rajamathi, R. Seshadri, Oxide and chalcogenide nanoparticles from hydrothermal/solvothermal reactions, *Current Opinion in Solid State and Materials Science*, 6 (2002) 337-345.
- [93] C.S. Cundy, P.A. Cox, The hydrothermal synthesis of zeolites: Precursors, intermediates and reaction mechanism, *Microporous and Mesoporous Materials*, 82 (2005) 1-78.
- [94] M.K. Devaraju, I. Honma, Hydrothermal and Solvothermal Process Towards Development of LiMPO₄ (M = Fe, Mn) Nanomaterials for Lithium-Ion Batteries, *Advanced Energy Materials*, 2 (2012) 284-297.
- [95] C. Perego, R. Millini, Porous materials in catalysis: challenges for mesoporous materials, *Chemical Society Reviews*, 42 (2013) 3956-3976.
- [96] G.R. Patzke, Y. Zhou, R. Kontic, F. Conrad, *Oxide Nanomaterials: Synthetic Developments, Mechanistic Studies, and Technological Innovations*, Angewandte Chemie International Edition, 50 (2011) 826-859.
- [97] W. Shi, S. Song, H. Zhang, Hydrothermal synthetic strategies of inorganic semiconducting nanostructures, *Chemical Society Reviews*, 42 (2013) 5714-5743.

- [98] M. Sanchez Sanchez, F. Girgsdies, M. Jastak, P. Kube, R. Schlögl, A. Trunschke, Aiding the Self-Assembly of Supramolecular Polyoxometalates under Hydrothermal Conditions To Give Precursors of Complex Functional Oxides, *Angewandte Chemie International Edition*, 51 (2012) 7194-7197.
- [99] J. Noack, F. Rosowski, R. Schlögl, A. Trunschke, Speciation of Molybdates under Hydrothermal Conditions, *Zeitschrift für anorganische und allgemeine Chemie*, 640 (2014) 2730-2736.
- [100] S.H. Yu, B. Liu, M.S. Mo, J.H. Huang, X.M. Liu, Y.T. Qian, General Synthesis of Single-Crystal Tungstate Nanorods/Nanowires: A Facile, Low-Temperature Solution Approach, *Advanced Functional Materials*, 13 (2003) 639-647.
- [101] F. Gonzalez-Vilchez, W.P. Griffith, Transition-metal tetra-oxo-complexes and their vibrational spectra, *Journal of the Chemical Society, Dalton Transactions*, (1972) 1416-1421.
- [102] L.H. Hoang, N.T.M. Hien, W.S. Choi, Y.S. Lee, K. Taniguchi, T. Arima, S. Yoon, X.B. Chen, I.-S. Yang, Temperature-dependent Raman scattering study of multiferroic MnWO₄, *J Raman Spectrosc*, 41 (2010) 1005-1010.
- [103] M.N. Iliev, M.M. Gospodinov, A.P. Litvinchuk, Raman spectroscopy of MnWO₄, *Physical Review B*, 80 (2009) 212302.
- [104] X. Li, T. Lunkenbein, V. Pfeifer, M. Jastak, P.K. Nielsen, F. Girgsdies, A. Knop-Gericke, F. Rosowski, R. Schlögl, A. Trunschke, Selective Alkane Oxidation by Manganese Oxide: Site Isolation of MnO_x Chains at the Surface of MnWO₄ Nanorods, *Angew. Chem. Int. Ed.*, 55 (2016) 4092-4096.
- [105] Mohsen B. Salah, S. Vilminot, T. Mhiri, M. Kurmoo, Synthesis, Crystal Structure, and Magnetic Properties of Mn₂(OH)₂SO₄: A Novel Layered Hydroxide, *European Journal of Inorganic Chemistry*, 2004 (2004) 2272-2276.
- [106] M. Li, Z. Wu, S.H. Overbury, Surface structure dependence of selective oxidation of ethanol on faceted CeO₂ nanocrystals, *Journal of Catalysis*, 306 (2013) 164-176.
- [107] S. Muthamizh, R. Suresh, K. Giribabu, R. Manigandan, S. Praveen Kumar, S. Munusamy, V. Narayanan, MnWO₄ nanocapsules: Synthesis, characterization and its electrochemical sensing property, *Journal of Alloys and Compounds*, 619 (2015) 601-609.
- [108] T.-D. Nguyen, D. Mrabet, T.-T.-D. Vu, C.-T. Dinh, T.-O. Do, Biomolecule-assisted route for shape-controlled synthesis of single-crystalline MnWO₄ nanoparticles and spontaneous assembly of polypeptide-stabilized mesocrystal microspheres, *CrystEngComm*, 13 (2011) 1450-1460.
- [109] J.-M.M. Millet, Mechanism of first hydrogen abstraction from light alkanes on oxide catalysts, *Topics in Catalysis*, 38 (2006) 83-92.
- [110] C. Coperet, C-H Bond Activation and Organometallic Intermediates on Isolated Metal Centers on Oxide Surfaces, *Chemical Reviews*, 110 (2009) 656-680.
- [111] R.A. van Santen, I. Tranca, E.J.M. Hensen, Theory of surface chemistry and reactivity of reducible oxides, *Catalysis Today*, 244 (2015) 63-84.
- [112] X. Rozanska, R. Fortrie, J. Sauer, Size-Dependent Catalytic Activity of Supported Vanadium Oxide Species: Oxidative Dehydrogenation of Propane, *Journal of the American Chemical Society*, 136 (2014) 7751-7761.
- [113] Y. Chabre, J. Pannetier, Structural and electrochemical properties of the proton / γ -MnO₂ system, *Progress in Solid State Chemistry*, 23 (1995) 1-130.

- [114] A.A. Budneva, E.A. Paukshtis, A.A. Davydov, IR-spectroscopic studies of strength and concentration of acid centers on V₂O₅/Al₂O₃ catalysts, *React. Kinet. Catal. Lett.*, 34 (1987) 63-67.
- [115] A. Knop-Gericke, E. Kleimenov, M. Hävecker, R. Blume, D. Teschner, S. Zafeirotas, R. Schlögl, V.I. Bukhtiyarov, V.V. Kaichev, I.P. Prosvirin, A.I. Nizovskii, H. Bluhm, A. Barinov, P. Dudin, M. Kiskinova, Chapter 4: X-Ray Photoelectron Spectroscopy for Investigation of Heterogeneous Catalytic Processes, in: C.G. Bruce, K.Z. Helmut (Eds.) *Advances in Catalysis*, Academic Press, 2009, pp. 213-272.
- [116] X. Li, T. Lunkenbein, J. Krohnert, V. Pfeifer, F. Girgsdies, F. Rosowski, R. Schlögl, A. Trunschke, Hydrothermal synthesis of bi-functional nanostructured manganese tungstate catalysts for selective oxidation, *Faraday Discuss.*, 188 (2016) 99-113.

Appendix

Curriculum vitae

Name: Xuan Li

M/F: Male

Date of birth: 06.06.1988

Nationality: Chinese

Education

- PhD (2013-Present) on Heterogeneous Catalysis
 - Institutes: Fritz-Haber-Institute of the Max-Planck-Society and BasCat Unicat BASF JointLab
- Master of Science (2010-2013) in Physical Chemistry in Nanjing University
- Bachelor of Science (2006-2010) in Chemistry in Nanjing University

Publication List

- [1] **X. Li**, T. Lunkenbein, V. Pfeifer, M. Jastak, P. K. Nielsen, F. Girgsdies, A. Knop-Gericke, F. Rosowski, R. Schlögl and A. Trunschke, Selective Alkane Oxidation by Manganese Oxide: Site Isolation of MnOx Chains at the Surface of MnWO₄ Nanorods, *Angew. Chem. Int. Ed.*, 2016, 55, 4092-4096
- [2] **X. Li**, T. Lunkenbein, J. Krohnert, V. Pfeifer, F. Girgsdies, F. Rosowski, R. Schlögl and A. Trunschke, Hydrothermal synthesis of bi-functional nanostructured manganese tungstate catalysts for selective oxidation, *Faraday Discuss.*, 2015, DOI: 10.1039/C5FD00191A
- [3] A. Y. Klyushin, M. T. Greiner, X. Huang, T. Lunkenbein, **X. Li**, O. Timpe, M. Friedrich, M. Hävecker, A. Knop-Gericke and R. Schlögl, Is nanostructuring sufficient to get catalytically active Au?, *ACS Catalysis*, 2016, DOI: 10.1021/acscatal.5b02631, 3372-3380
- [4] **X. Li**, S. Ye, J. Zhao, L. Li, L. Peng and W. Ding, Selective oxidation of toluene using surface-modified vanadium oxide nanobelts, *Chinese Journal of Catalysis*, 2013, **34**, 1297-1302
- [5] H. Liu, C. Guan, **X. Li**, L. Cheng, J. Zhao, N. Xue and W. Ding, The Key Points of Highly Stable Catalysts for Methane Reforming with Carbon Dioxide, *ChemCatChem*, 2013, **5**, 3904-3909

Oral presentation List

[1] **49th Annual German Catalysis Meeting**, Weimar, Germany, **2016**, Identification of active site of nanostructured MnWO₄ in selective activation of propane, Xuan Li, Thomas Lunkenbein, Verena Pfeifer, Jutta Kröhnert, Johannes Noack, Frank Girgsdies, Frank Rosowski, Robert Schlögl, Annette Trunschke

[1] **Designing New Heterogeneous Catalysts: Faraday Discussion**, London, United Kingdom, **2016**, Hydrothermal synthesis of bi-functional nanostructured Paper manganese tungstate catalysts for selective oxidation, Annette Trunschke, Xuan Li, Thomas Lunkenbein, Jutta Kröhnert, Verena Pfeifer, Frank Girgsdies, Frank Rosowski, Robert Schlögl,

Poster presentation List

[1] **16th International Congress on Catalysis**, Beijing, China, **2016**, Selective Alkane Oxidation by Manganese Oxide: Site Isolation of MnO_x Chains at the Surface of MnWO₄ Nanorods, Xuan Li, Thomas Lunkenbein, Detre Teschner, Jutta Kröhnert, Christian Schluz, Frank Rosowski, Robert Schlögl, Annette Trunschke

[2] **48th Annual German Catalysis Meeting**, Weimar, Germany, **2015**, Shape-dependent catalytic properties of nanostructured MnWO₄ in selective oxidation, Xuan Li, Thomas Lunkenbein, Verena Pfeifer, Jutta Kröhnert, Frank Girgsdies, Raoul Naumann d'Alnoncourt, Frank Rosowski, Robert Schlögl, Annette Trunschke